Design, Fabrication and Control of a Soft Robotic Arm

by

Batu

A thesis submitted to Auckland University of Technology in partial fulfilment of the requirements for the degree of Master of Engineering

School of Engineering, Computer and Mathematical Sciences
Auckland University of Technology
New Zealand

December 2024

Abstract

Soft robots are a class of robots made from flexible materials, allowing them to operate effectively in complex and unstructured environments, which is different from traditional rigid robots. This thesis focuses on a soft robotic arm with a folded origami structure, exploring its control system and manufacturing method.

In manufacturing, experiments were conducted to test the adhesion strength of different materials. Based on the results, the overall fabrication method was defined, and a new fabrication method for the origami soft robot arm was proposed. This method ensures the structural integrity of the soft robotic arm and improves production efficiency.

Regarding the control system, most current soft robot control systems rely on internal sensors or external vision for mechanism spatial positioning. This thesis presents a control system integrating internal sensors and external stereo vision. It can accurately regulate the robot's response, preventing damage to the pneumatic drive system and soft robot structure from excessive compression and extension.

The control system enables accurate spatial positioning and configuration identification of the soft robot using cameras, even in the absence of a mechanical or analytical model. Furthermore, the system incorporates feedback signals from the soft robot's internal air pressure sensor, enabling the real-time calculation of its spatial position and shape while simultaneously measuring the fluctuations in internal pressure. A closed-loop control system is established by integrating visual feedback and air pressure feedback, safeguarding the soft robot's components and the origami's three-dimensional structure while the user operates the robot.

Additionally, this thesis introduces a stereo vision pipeline suitable for MATLAB based on the control system's stereo vision. This pipeline simplifies the establishment of a stereo vision system and enables rapid target object identification, enhancing the soft robotic arm's operational efficiency and accuracy.

The new control system, soft robot design, and fabrication method provide a reference for the control and manufacturing of origami soft robots.

Contents

Attestation of Authorship

I hereby declare that this submission is my own work and that, to the best of my knowledge and belief, it contains no material previously published or written by another person (except where explicitly defined in the acknowledgements), nor used artificial intelligence tools or generative artificial intelligence tools (unless it is clearly stated, and referenced, along with the purpose of use), nor material which to a substantial extent has been submitted for the award of any other degree or diploma of a university or other institution of higher learning.

Signature: _____
Date: _____

Chapter 1

Introduction

Traditional, rigid robotic arms have found widespread application in industrial manufacturing, surgical medicine, aerospace engineering, and other fields. These robotic arms are composed of joints and rods and are generally driven by motors or hydraulic systems.

Traditional robotic arms have a limited number of degrees of freedom (DoF) due to their rigid structure. This restricts their range of motion and adaptability. Increasing the DoF makes robot control more complex because standard kinematic models like Denavit-Hartenberg parameterization do not apply easily [1]. However, soft robotic arms with high DoF offer several advantages [2]. They improve safety in human-robot interaction by bending upon contact instead of causing injury. They conform to rigid objects without requiring precise shape modelling. They also handle delicate workpieces gently, making them useful in medicine and food processing [3]. Despite the control challenges, soft robotic arms provide a flexible and safe solution for many applications.

However, due to their structural design, they possess only limited degree of freedom. In industrial manufacturing that uses traditional robotic arms, their usage scenarios and spatial positions are limited after the robotic arms are designed and assembled, rendering them unable to perform other tasks. The advent of soft robotic arms has introduced a solution to this predicament.

1.1 Research Background

The soft robotic arms can deform, dexterously operate, and grasp objects, conferring upon them the ability to move and adapt in various environments. For example, using a unique biological material at the end of the soft robotic arm's gripper enables it to recognise specific substances in living organisms and automatically grasp desired objects [4].

A soft robotic arm is a branch of soft robots. Given the variety of designs in soft robots, they can be defined as an autonomous system with rigid mechanisms and flexible joints that exhibit passive compliance or a system made from low modulus materials, characterised by inherent compliance from elastic/hyperelastic materials [5]. The former is also divided into semi-soft continuous robots and soft continuous robots due to its rigid structure. Its structure is similar to

traditional rigid robots [2]; therefore, the following discussion will focus on the latter.

Soft robots with low-modulus materials typically include memory metals, flexible plastics, origami, etc. The fabrication of soft robots manufactured from memory metals and flexible plastics is challenging due to the necessity of special materials and processing techniques, including the use of special alloys, complex compounds, and high-temperature injection moulding. In contrast, origami-inspired soft robots are characterised by simple preparation, cost-effectiveness, and the capacity to transform two-dimensional shapes into three-dimensional shapes with a high degree of collapse and space efficiency [6]. Consequently, origami-inspired soft robots have garnered significant attention.

Origami-inspired soft robotic arms represent a fusion of the advantages of traditional robotic arms and origami-inspired soft robots. They can perform the same actions as traditional robotic arms while exhibiting lightweight structures, material conservation, high flexibility, and deformability.

Current origami-inspired soft robot origami patterns include Kresling, Miura, Yoshimura, waterbomb and twisted tower. Folding these special patterns leads to differences in their three-dimensional structures and movement methods. The previously mentioned low-modulus materials include different materials such as paper, silicon rubber, and special alloys, which also affect soft robots' movement and manufacturing methods. The material will also affect the soft robot's driving method and control system.

The current landscape of soft robotic control methods reveals a notable difference. On one end of the spectrum, some control techniques demand an extensive foundation in mathematics and mechanical engineering, often involving complex modelling and design. Conversely, certain soft robots operate with no control methods, relying on simplistic manual operation or the unique structure of the soft robot. The former approach, grounded in mathematical modelling, requires substantial data collected from the robot, which can be arduous and resource-intensive. Furthermore, the precision and accuracy of manufacturing soft robots are pivotal factors closely intertwined with control methods, affecting their effectiveness and reliability. Using computer vision to identify soft robots and calculate their spatial position presents a possible solution to the two problems of avoiding complex mathematical models and accurate robot fabrication.

This thesis begins with a discussion of the current research status of soft robots, and by comparing different manufacturing methods. It proposes a feasible and quickly reproducible manufacturing method for origami-inspired soft robotic arms (OSRA) and its control system.

1.2 Research Questions

Based on these, this thesis will research four issues:

The first problem is the choice of origami pattern. Due to folding difficulty, three-dimensional structure after folding, and direction and method of spatial compression of the three-dimensional, these characters are all related to their particular patterns. Which origami pattern is more suitable for making an OSRA?

The second problem is divided into two points: first, which driving method is used after selecting an origami pattern? Secondly, which material is used, and what's the suitable fabrication method? The common drive methods are pneumatic or hydraulic, which require the origami material to be airtight. If we focus on the difficulty of origami, the most commonly used material is printed paper. The origami pattern can be printed on this material, facilitating the folding process. However, print paper is not airtight, which affects the locomotion of the soft robotic arm. Therefore, the choice of origami material and drive method will affect each other, and both need to be considered.

The third problem is OSRA motion detection. Some flexible robot arm motion detection uses mathematical models of robots, monocular cameras, deep learning models [7], or even motion capture systems [8]. Robot control systems using stereo vision are primarily used for rigid robots. These studies can provide guidance, such as camera calibration and position estimation using stereo vision combined with robot simulation [9]. However, to detect the movement of the OSRA without any model, some techniques or standards are needed to simplify or standardise the process. What is the best stereo image processing pipeline or recognition technique to extract the state of the robot arm?

The final research question concerns the control system of the OSRA. This study examines how stereo vision can be used to obtain spatial position information of the soft robotic arm and how this data can be integrated into the control system. The vision system provides shape measurements that lift the control system from control of air pressure to the more relevant and direct control of the physical length of the actuator. One key question is how stereo vision feedback can be combined with signals from the OSRA's pneumatic drive system to improve motion accuracy and prevent excessive deformation. Additionally, this research investigates whether pressure sensors can complement stereo vision feedback to enhance control precision. Finally, an effective way to present real-time system data to the user is explored, ensuring intuitive operation and monitoring.

1.3 Contribution of this Thesis

This thesis presents key improvements in the mechanical design, fabrication, and control of the OSRA.

1.3.1 Mechanical Design and Material Optimisation

The soft robotic arm was designed with a laminated material to improve structural integrity while maintaining flexibility. A plexiglass sealing mechanism was introduced to enhance airtightness and durability, ensuring consistent pneumatic actuation. The origami-inspired structure was adjusted to reduce unwanted rotational movement, improving stability and precision during operation.

1.3.2 Fabrication Process

A cost-effective and maintainable fabrication method was developed by evaluating different manufacturing techniques. The proposed method simplifies assembly and allows easy replacement of individual components, improving the long-term usability of the soft robotic arm. Laser-cut acrylic components were incorporated to enhance structural alignment and reduce assembly errors.

1.3.3 Pneumatic Control System

The pneumatic control system was optimised with an improved valve configuration, ensuring more precise pressure modulation and faster response times. An ESP32 microcontroller was integrated to enable real-time wireless communication and enhance system flexibility. A pressure sensor was added to monitor internal air pressure, preventing excessive compression and improving actuation consistency.

1.3.4 OSRA Spatial Tracking

A stereo vision system was implemented to track the spatial position and deformation of the soft robotic arm. This system provides real-time motion data, allowing for performance evaluation and refinement of mechanical design parameters. By integrating stereo vision with pressure sensor feedback, the system ensures stable actuation and helps prevent excessive deformation, improving the reliability of the robotic arm during operation.

These improvements contribute to the structural robustness, ease of fabrication, and operational reliability of the OSRA, making it a more practical solution for soft robotics applications requiring adaptable and precise movement control.

Chapter 2

Literature Review

The first academic journal dedicated to soft robotics, Soft Robotics, was launched in 2014. Its editorial states, 'Soft Robotics is therefore truly interdisciplinary by necessity, drawing on all areas of engineering and combining them with biomedical engineering, biomechanics, mathematical modelling, biopolymer chemistry, computer science, and tissue engineering.' [10]

Today, soft robotics has emerged in many different research directions, and various aspects, such as control systems, materials, and processing, which have all impacted soft robotics research. The study of animals has greatly inspired soft technology in robotic systems [11]. Imitating the movement of animals or human organs occupies a large part of it. Soft robots can be driven in different ways when moving, which involves various aspects such as materials, manufacturing and structure.

Another important aspect is the control system, particularly after a robot has been designed or developed. It determines the response and performance of the robot. In the control system of a soft robot, there are different types of control systems, such as open-loop control systems, closed-loop control systems, or no control system at all due to their unique design and mechanism. Of these control systems, the closed-loop control system is more widely studied due to its feedback signals. Most of these signals are sourced from sensors, which can be categorized into internal and external sensors based on their design.

This section will introduce the current development of soft robots according to the driving principles, materials used, fabrication methods, and control system. A stereo vision pipeline will also be introduced, which is used to establish a stereo vision system as a feedback signal in the control system of a soft robot.

2.1 Driving Principles of Soft Robots

Research and development of soft robots is relatively new, but many applications have already been identified. Saurabh and Mohamad developed a glove-like soft robot to provide better feedback when users grip or handle items in VR/AR scenarios; it has a variable stiffness with fibre jamming [12]. Benjamin's team designed an external cardio pump to increase the cardiac compression ability, covering the heart from the outside and providing an external compression force [13]. Ciaran's team developed a wearable device to help stroke survivors rehabilitate

their ability to move their upper limbs [14]. These applications have their unique principle of driven or locomotion. Based on the type of transportation, it could also be divided into grippers, peristalsis, soft tables, and any other possible ways.

This section provides a brief introduction to the technology of soft robotics research based on the driving principles. It covers different types of soft robots and various control systems.

2.1.1 Pneumatic-Driven Method

Pneumatics commonly refers to studying and applying pressurised gas to produce mechanical motion. [11] Compared to other methods, the energy conversion of a soft robot with a pneumatic drive is simpler. The gas is pumped into the soft robot through pipes, increasing the internal pressure and causing the robot to compress, stretch, and bend. This makes pneumatic-driven more popular than others. Air is the most efficient medium because it is easy to contain, lightweight, and does not emit any pollution. Inspired by the elephant's trunk, Leng and his team proposed a series of pneumatic artificial bending helical muscles [15]. This pneumatic artificial muscle can be traced back to the McKibben pneumatic artificial muscle proposed in the 1970s [16]. It uses a pneumatically driven method to cause the actuator to undergo axial compression and stretching, and the movement is like the muscle tissue of animals. Leng's research has enabled the pneumatic artificial muscle to undergo helical stretching and helical contraction deformation [15], opening a new direction in pneumatically actuated soft robots' movement and structural design. King and his team use a pneumatic driving system to control a soft robotic arm that can bend, compress and extend [17]. The pneumatic drive system consists of three air pumps, six solenoid valves and an Arduino Nano microcontroller.

2.1.2 Chemical-Reactions Driven Method

This soft robot commonly uses either energy exchange accompanied by a response like electricity and heat, or other products of chemical reaction, like oxygen and carbon dioxide. However, it may have to be combined with other driven methods [18]. Nicholas used a multi-material 3D printer to print the functional body of a robot. The lower section comprises a hemispheroid housing an initial volume into which oxygen and butane are introduced. Upon ignition of the chemical components, a volumetric explosion is initiated, propelling the robot into the air [19]. Chemical-driven methods are commonly used to power small soft robots and often involve combustion and explosions. Therefore, to ensure that chemical reactions can proceed as desired and do not cause other hazards, such as fire or shrapnel from the explosion of the robot, the materials used and the structural design of soft robots must be carefully considered. So, the overall design must meet high requirements.

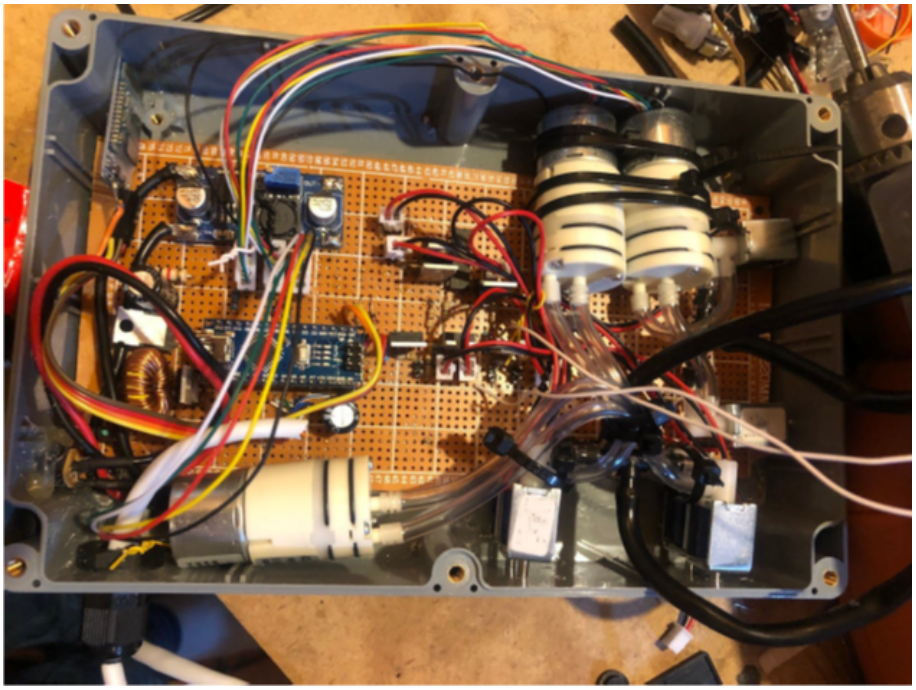

Figure 2.1: Pneumatic System [17]

2.1.3 Twisted And Coiled Polymer Actuators

These are produced via an economically efficient manufacturing procedure. It involves subjecting a straight fibre to tensile stress, inducing substantial twisting until the spontaneous formation of coils [20]. The twisted and coiled polymer actuator presents two notable benefits: its low weight and cost efficiency [21].

2.1.4 Smart Material

Some soft robots that utilise smart materials are distinguished from those that employ other actuation methodologies in that the material itself can be used as a power source. When an external stimulus is received, a soft robot that uses a smart material will deform and generate movement. Shape-memory alloys and shape-memory polymers are two commonly used materials. The production process for such actuators focuses more on the selection of materials and the material's deformation principle. The utilisation of smart material in soft robots will be discussed in the next section.

2.2 Material of Soft Robots

The materials used to make soft robots are usually related to their driving methods. Commonly used materials are shape memory materials or flexible materials. Different materials make the application environment and movement character-

istics of soft robots different. This section will introduce the materials currently used in soft robot research and development.

2.2.1 Shape Memory Materials

Shape memory material is material that can return to its original form from its present state in response to external factors.

Shape Memory Alloy (SMA)

SMAs are intermetallic compounds capable of repeatedly and reversibly returning to a predefined shape throughout heating and cooling cycles. On a microscopic scale, this process involves a phase transition from martensite, which is stable at lower temperatures, to austenite, the stable phase at higher temperatures [22]. SMAs can transform thermal energy into mechanical energy and offer benefits such as straightforward manufacturing and cost efficiency. These materials have been utilized in various applications, including soft crawling robots, micro-robots, soft robotic jellyfish, and variable stiffness exoskeletons. As shown in Figure 2.2, Liu and his team designed a self-folding bird with an electrically programmable shape-memory function [23].

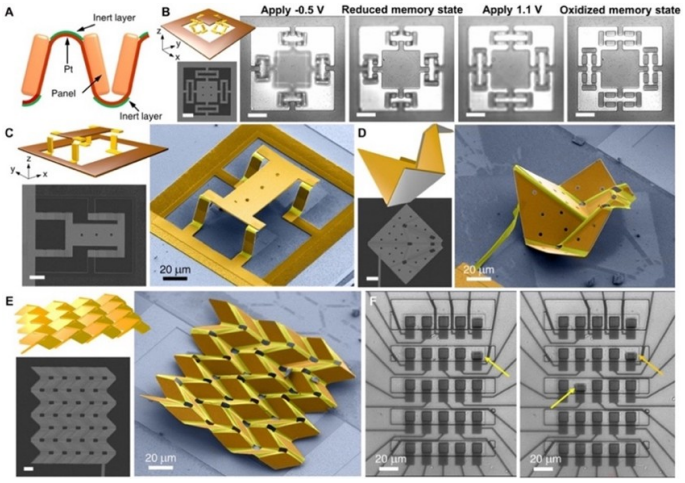

Figure 2.2: Actuator with SMA [23]

Shape Memory Polymer (SMP)

SMPs are elastic polymer networks integrated with stimuli-responsive switches. The shape-memory effect is not an inherent property of polymers; rather, it arises from the combination of polymer morphology and specific processing techniques, functioning as a tailored material adaptation. During conventional processing, the polymer is first molded into its permanent shape. In a subsequent programming step, it is deformed and stabilized into a temporary configuration [24]. Fig-

ure 2.3 illustrates an advanced electro-thermal actuator with a tri-layer structure composed of carbon nanotubes, kapton, and a thermo-responsive shape memory polymer [25]. SMPs are applicable not only in soft robotics but also in biomedical fields, including vascular grafts and cardiovascular stents [26].

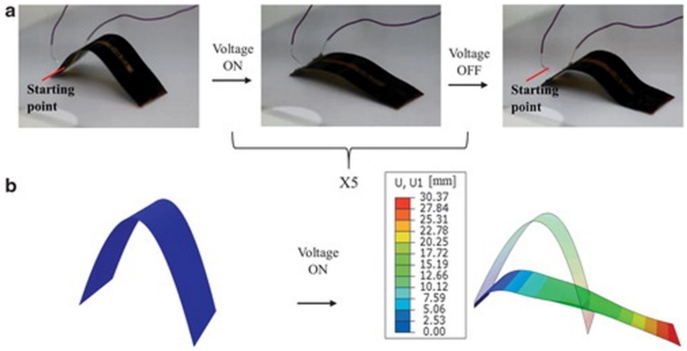

Figure 2.3: Actuator with SMP [25]

Shape Memory Hydrogels (SMH)

In medical applications of SMP materials, researchers have observed that hydrophilic polymeric hydrogels, with their higher water content, exhibit superior biocompatibility and a closer resemblance to human tissue [26]. Their soft, water-rich nature also makes them ideal for fabricating soft robots. SMH can recover either programmed or permanent structural configurations when subjected to specific stimuli, such as temperature and pH changes [27]. As shown in Figure 2.4, Li developed a double-layer soft robot using SMH, capable of performing both gripping and stretching motions in response to temperature variations [28].

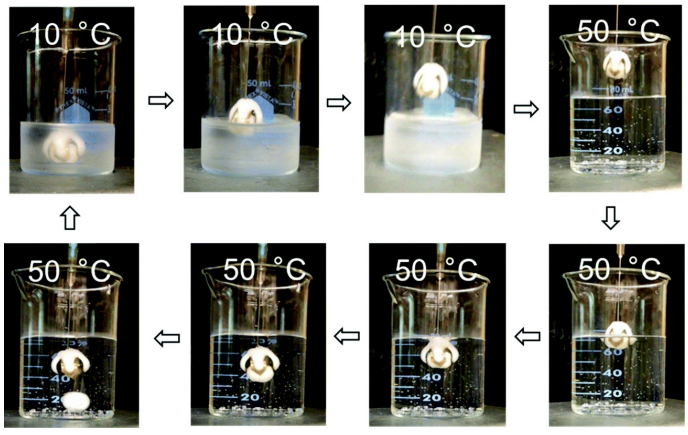

Figure 2.4: Actuator with SMH [28]

2.2.2 Flexible Material

Among the previously mentioned materials, all except SMH are still considered rigid. In these materials, deformation occurs only in limited regions, while the

majority retains a fixed shape to preserve the spatial structure of the soft robot. However, certain soft robots are designed for full-body flexibility, necessitating the use of materials that are inherently soft and highly adaptable. This section explores the materials employed in such fully flexible soft robots.

Silicone-based Material

Silicone, or polysiloxane, is a polymer consisting of repeating siloxane units and typically appears as a colorless oil or rubber-like material. It is widely used in sealants, adhesives, lubricants, medicine, cookware, thermal insulation, and electrical insulation, with common forms including silicone oil, grease, rubber, resin, and caulk [29]. Owing to its softness and airtight nature, silicone has gained significant research interest and is commonly applied in soft robotics [30–32]. Among various silicone-based materials, EcoFlex stands out for its ease of use and the diverse range of available variants, primarily distinguished by differing hardness levels after curing. Its properties have led to extensive research on its applications in soft robot fabrication [33–37].

Fibres

Twisted and coiled polymer actuators are commonly constructed using nylon fibre or fishing line. These actuators replicate human muscle movement by intertwining multiple strands and integrating conductive nylon fibre to achieve electrically induced motion via Joule heating. Another approach employs an inner silicone microtube or microtubule combined with an externally constrained micro-coil. The distal end of the microtubule is knotted and sealed to the micro-coil with adhesive silicone, while the proximal end is connected to a fluid source through a transmission tube [38], as illustrated in Figure 2.5.

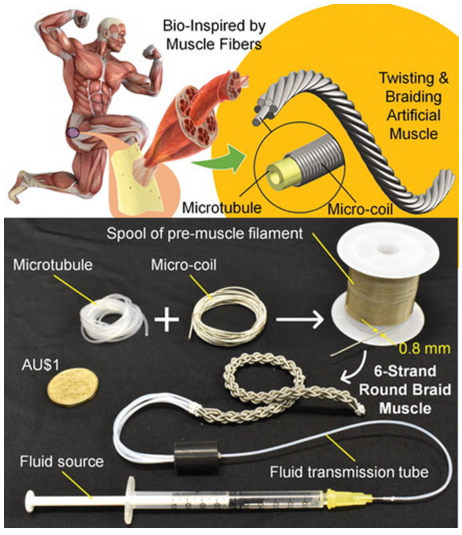

Figure 2.5: Actuator with Fibre [38]

2.3 Fabrication Methods of Soft Robots

Fabrication techniques are critical for turning soft robot designs into tangible products. While some soft robots are produced manually from a single material using methods such as casting or molding, fully realizing their potential will require advanced manufacturing processes that can integrate multiple materials into complex structures simultaneously [39]. The following section reviews several commonly employed fabrication methods for soft robots beyond manual manufacturing.

2.3.1 3D Printing

According to Standard ISO/ASTM 52900:2021, 3D printing is classified into seven distinct categories [40]: binder jetting, directed energy deposition, material extrusion, material jetting, powder bed fusion, sheet lamination, and vat photopolymerisation. This section will focus on three of these well-established technologies, which have extensive applications across various fields.

Material Extrusion

This method is currently the most widely used 3D printing technique. First, a low-melting material—either plastic or metal—is heated until molten and then delivered to the print head. By coordinating the movement of the print head and the print bed, the molten material is deposited layer by layer to form the desired shape, thereby completing the print. In soft robot manufacturing, material extrusion is frequently employed, with PLA plastic being a common material. Through specialized structural designs, even soft robots fabricated from PLA plastic can exhibit a notable degree of deformability [41]. Alternatively, flexible materials such as TPU are also used for printing and fabricating soft robots [42]. In addition, some studies have modified material extrusion printers by integrating features from stereolithography, where ultraviolet light is applied along the extrusion path while the flexible material is deposited, thus achieving simultaneous printing and curing [43].

Stereolithography

Stereolithography, which is the most prevalent method, operates by directing an ultraviolet laser onto a vat containing photopolymer resin. Using computer-aided manufacturing and design software, the ultraviolet laser traces a pre-programmed pattern onto the surface of the resin. Because the photopolymer resin is sensitive to ultraviolet light, exposure induces a photochemical reaction that solidifies the resin into a single layer of the desired three-dimensional object. Afterwards, the build platform is lowered by one layer, and a blade evenly reapplies resin

over the vat. This process is repeated layer by layer until the three-dimensional object is fully formed [44]. In soft robot research, stereolithography is typically employed to fabricate moulds, with soft robots subsequently produced through casting; however, some studies have achieved direct fabrication of soft robots by using specialized materials or modified stereolithography 3D printers [45, 46].

Powder Bed Fusion

Laser powder bed fusion is a widely adopted method in metal additive manufacturing that uses a laser to melt fine metallic powders, building complex parts layer by layer. Figure 2.6 illustrates a typical laser powder bed fusion system. This method offers a cost-effective approach to fabricating parts with intricate geometries, although achieving consistent quality remains challenging. Consequently, real-time monitoring of the process is essential to produce defect-free parts that meet predetermined quality standards [47]. While laser powder bed fusion typically yields metal components, in soft robot manufacturing it is limited to mold fabrication, since creating soft robots requires the use of flexible materials.

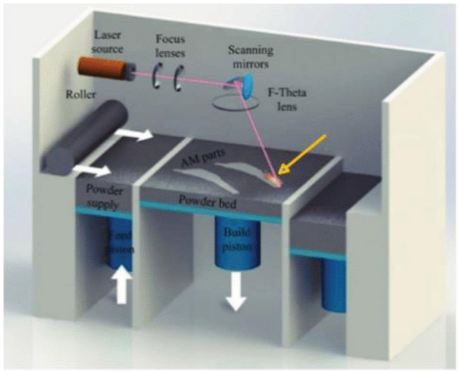

Figure 2.6: Powder Bed Fusion [47]

2.3.2 Photolithography

Photolithography is a technique for producing integrated circuits by using light to imprint a pattern onto a substrate, usually a silicon wafer. The process starts by applying a photosensitive photoresist onto the substrate, after which a photomask containing the desired design is placed on top. Light passes through the photomask, exposing selected areas of the photoresist; these exposed regions then experience chemical changes that make them either soluble or insoluble in a developer solution. Once developed, the pattern is transferred to the substrate using methods such as etching, chemical vapor deposition, or ion implantation [48]. In an innovative twist, Wu's team utilized leaves as photolithography templates, successfully replicating the leaf vein patterns onto a soft substrate with a resolution of up to $500\,\mathrm{nm}$, and the transferred patterns can endure pressures as high as

260 kPa [49]. This breakthrough paves the way for new, high-precision fabrication methods in soft robotics.

2.3.3 Laser Cutting

Laser machining, leveraging the non-contact nature of laser beams, allows for intricate and customised designs on soft materials, enabling the fabrication of precise and complex actuator structures. High-precision lasers cut or etch patterns and channels in soft materials to control their deformation behaviour. Moghadam's team used a laser to cut multi-layer TPU film to create a soft robot that can swim by connecting multiple bag-like airbags [50], as shown in Figure 2.7.

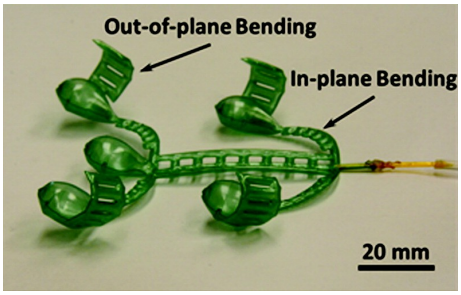

Figure 2.7: Powder Bed Fusion [50]

2.3.4 Molding and Casting

The moulding and casting process, whereby liquid or gel-like materials are poured or injected into custom moulds, produces soft robots with tailored shapes and properties. This method allows the same product to be manufactured quickly and in large quantities while maintaining consistency. In current soft robot manufacturing, 3D printing technology is more commonly used to make moulds, and other materials such as EcoFlex are then poured into the moulds and allowed to solidify, completing the fabrication of the soft robots [51–55].

2.4 Origami-inspired Soft Robots

A soft robot's driving system provides power and controls the changes in its spatial structure. Its functions include bending, rotating and other actions. However, the soft robot's special structural design also determines its actions' characteristics and methods during deformation. Origami's unique geometric design enables soft robots to achieve precise and diverse movements during deformation, greatly expanding their application scenarios. Origami special geometric structures can transform two-dimensional flat materials into complex three-dimensional forms. This feature enables origami-inspired soft robots to take ad-

vantage of the active deformation characteristics and maximise the use of space through geometric design.

Origami is known as the art of paper folding. It has inspired the design of many soft robots [56–58]. Its special geometric structure can transform two-dimensional flat materials into structures with complex three-dimensional shapes. Kresling [59], Miura [60], Yoshimura [61], waterbomb [62], and twisted tower [63] are some of the most widespread folding patterns used in the construction of soft robots.

2.4.1 Miura Pattern

The Miura pattern employs a unique zigzag design to create parallelograms and mirror reflections; each parallelogram and its reflection form mountain and valley folds.

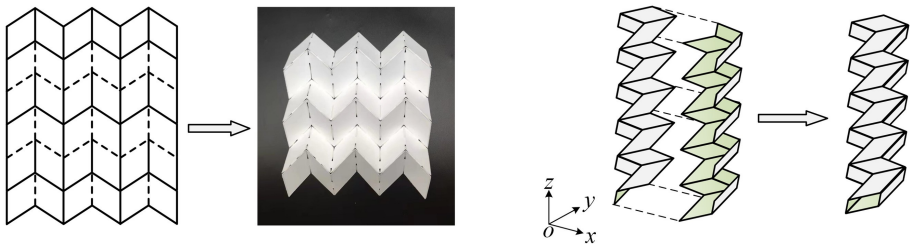

Figure 2.8: Miura Fold and Miura Tube [64]

2.4.2 Yoshimura Pattern

The Yoshimura pattern is a common type of fold that typically occurs when an elongated cylindrical structure is subjected to shearing or axial pressure, such as in a flattened can or clothing fabric [65].

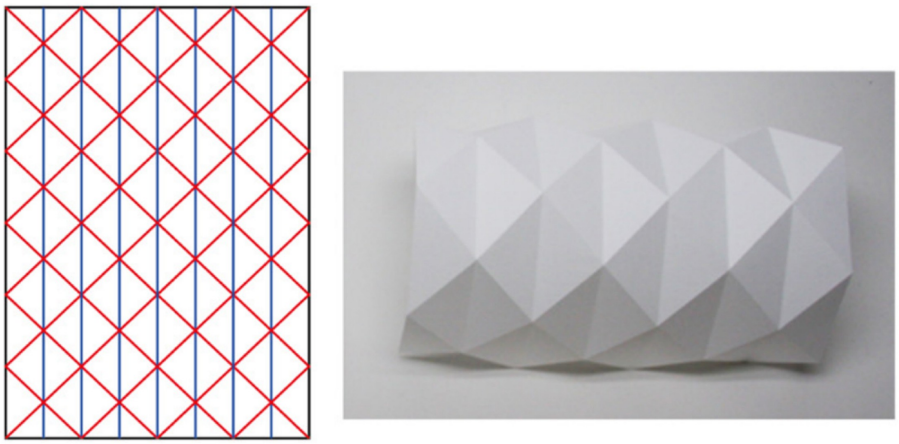

Figure 2.9: Yoshimura Fold [66]

2.4.3 Kresling Pattern

The term ”Kresling Pattern” describes the analogy between the deployable folding configuration seen in a hawkmoth’s bellows and the folding behavior of a cylindrical thin-walled shell that buckles spontaneously under torsional stress. Experiments using thin-walled cylinders fabricated from paper or polypropylene have shown that a ”natural” folding pattern—similar to that of the hawkmoth—emerges under torsional loading. In these tests, a thin-walled sheet is wrapped around two coaxial mandrels with a gap in between; when the mandrels are twisted, a highly regular and self-organized folding pattern develops across the gap. This pattern is composed of inclined, elongated parallelograms (mountain folds) that are bisected along their long diagonal by valley folds [67].

The Kresling pattern is considered superior to the Yoshimura pattern for thin-walled cylinders undergoing twist buckling, as it can accommodate large, complex yet predictable shape transformations.

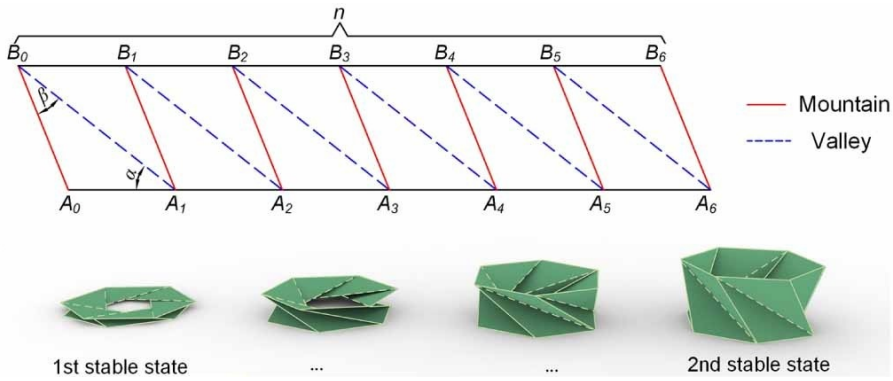

Figure 2.10: Kresling Pattern [68]

2.4.4 Waterbomb Pattern

Waterbomb origami features a pattern with multiple vertex points where six folds converge. A twist motion also exists, starting in the middle of the tube and successively spreading toward both ends [69], as shown in Figure 2.12. This movement can be thought of as the tube expanding rather than radially compressing or stretching. The nature of this expansion also makes it impossible to perform bending movements.

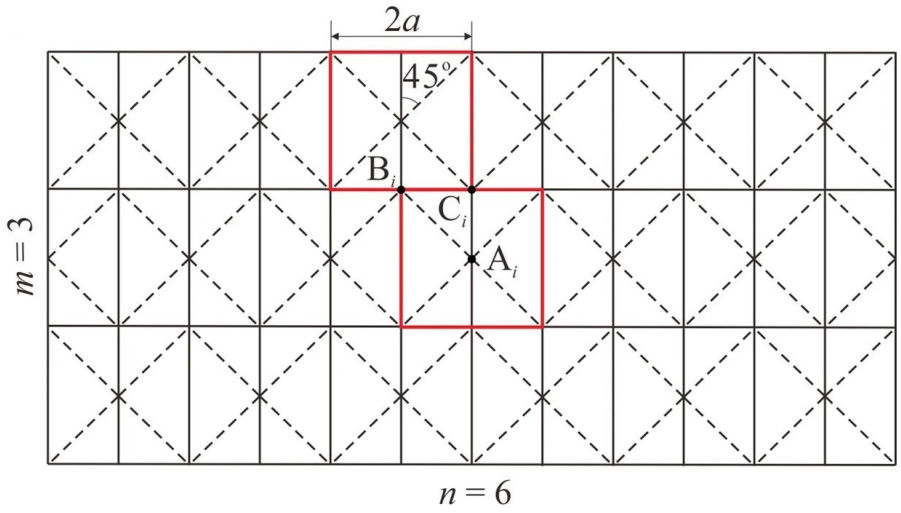

Figure 2.11: Waterbomb Pattern [69]

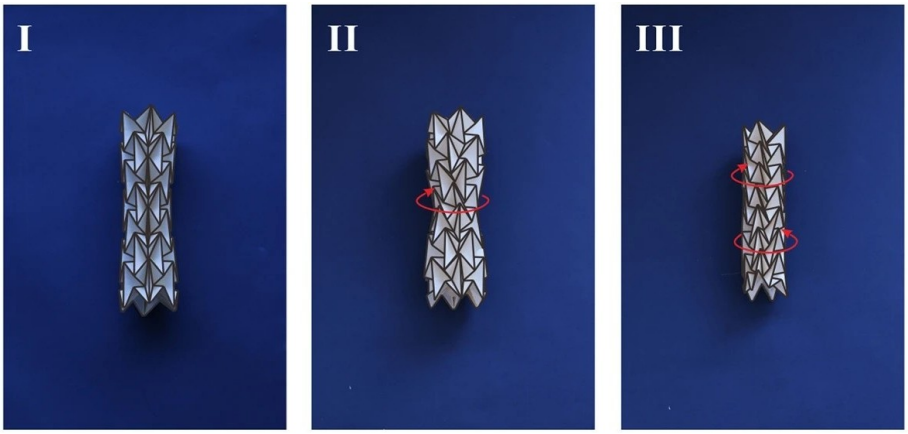

Figure 2.12: Waterbomb Tube [69]

2.4.5 Origami Twisted Tower

The Origami Twisted Tower combines multiple segments, usually containing 16 segments per layer. Its structure makes it easy to bend, twist, and stretch. As shown in Figure 2.13. Its mechanism has a unique hollow form, consisting of different segments spliced together to form a whole, and each segment also forms a hollow frame. This unique structure makes choosing the right driving method difficult, as neither a pneumatic nor a hydraulic driving system can be used. Only a tendon driving system or a special material like memory shape alloy can be considered.

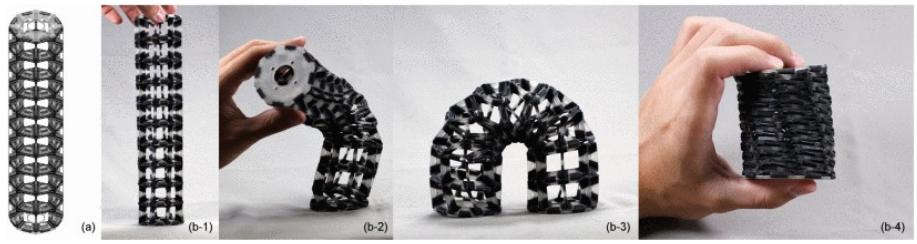

Figure 2.13: Origami Twisted Tower [70]

All of these folding patterns are used in the structural design of soft robots, but the most commonly utilised are the Yoshimura and Kresling patterns. King and his team used the Yoshimura pattern as the overall structure to create a soft robotic arm [17]. Although the Yoshimura pattern is relatively simple in design, in its folded three-dimensional structure, it is relatively soft in the horizontal direction, which means that it cannot withstand shearing forces. Any shearing force will cause the arm to bend. This result is shown in Figure 2.14.

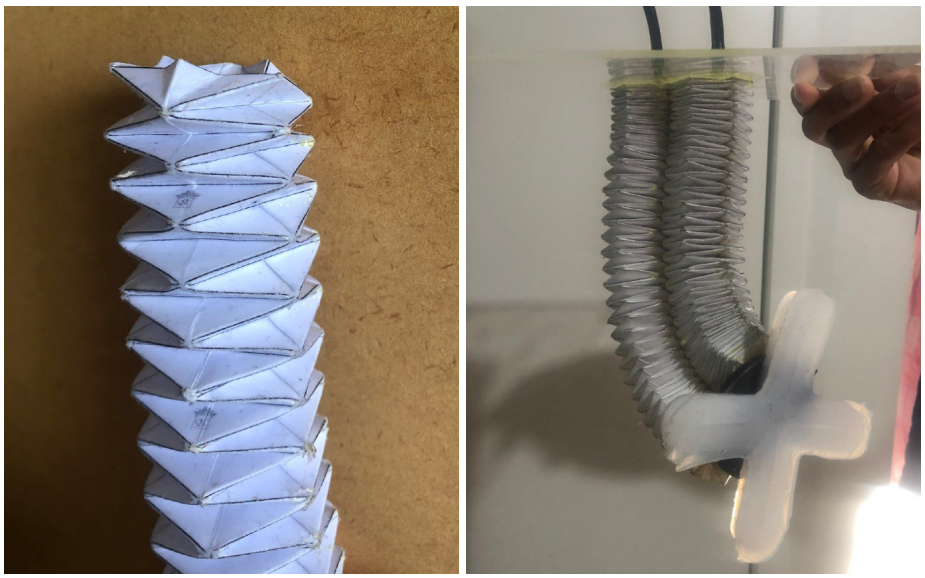

(a) Yoshimura Tube (b) Soft Robotic Arm

Figure 2.14: Soft Robotic Arm with Yoshimura Pattern [17]

Nguyen used the Kresling Pattern to create a soft table [71], as shown in Figure 2.15. It consists of multiple Kresling tubes. By controlling the compression and extension of different tubes, the upper surface of the soft table is deformed, causing objects on the table to slide and ultimately achieving the effect of moving objects. His project confirms that Kresling tubes not only have sufficient rigidity in vertical motion but also that when multiple tubes generate vertical motion with different compression ratios, they can cause nearby tubes to bend, and this bending is recoverable and will not cause structural damage.

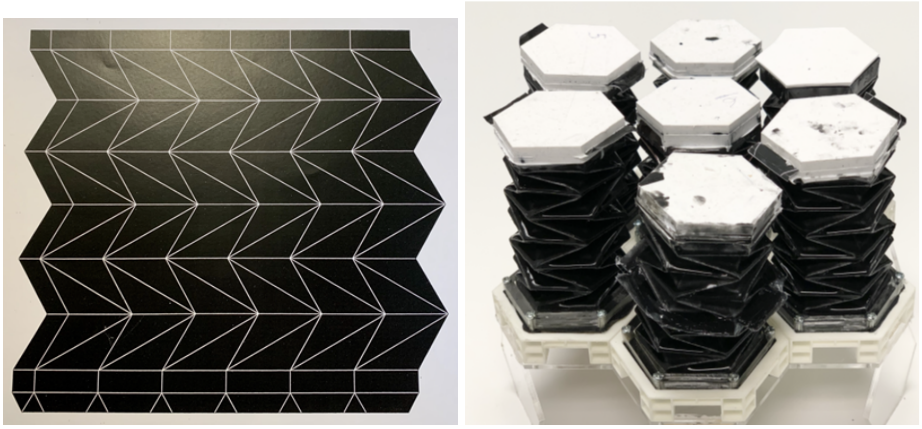

(a) Kresling Pattern (b) Soft Table

Figure 2.15: Soft Table with Kresling Pattern [71]

Origami structures are used in the design of many soft robots, and different types of origami structures have their own special three-dimensional structures and movement methods. By comparing different types of origami with their applications, the Kresling Pattern not only exhibits good compression and extension capabilities in vertical motion, but also maintains its vertical shape. It also has a certain degree of bending ability when combined with multiple Kresling tubes. Therefore, this thesis will use the Kresling Pattern as the origami structure for the OSRA.

2.5 Control System

Unlike rigid robots, the movement of soft robots is not limited by the DOFs. Using different designs could make a soft robot twist, bend, comprise, or expand. Control algorithms employed in the field of soft robotics can be classified into two categories: model-based and model-free control strategies. However, some of the researchers also certified the availability of soft robot designs with no control methods. This section will introduce the control system related to soft robotics.

2.5.1 Types of Control System

No Control Method

Currently, most of the development and research of soft robots are just proposing or verifying a design from a mechanical or physical point of view. The specific design is just compatible with a particular environment or purpose. Like the VR glove and after-stroke rehab equipment, which have been mentioned in Section 2.1, they have been running or operating under manual control, and there is no control method being designed. But for some other designs, the soft robot'

body passively adapts to the ambient environment and detailed control was not required

Model-based Control

The most common model-based control method for soft robots involves controlling the final position of the robot's end-effector. By using previously measured data, the robot's movements can be predicted and controlled. Low-level control is typically achieved by regulating pressure or volume.

Another approach employs linear PID control, which uses a cascade architecture of linear PID controllers to achieve effective tracking. For instance, in Minh's design [72], the inner loop uses pressure feedback to regulate the actuator's input pressure, while the outer loop generates a reference input for the inner loop based on the reference position and feedback. However, performance is often affected by unavoidable factors like hysteresis.

Before soft robotics became widely recognised, researchers and engineers explored applying biomimetics to robotics. Continuum robots, inspired by snakes, tree trunks, and tendrils, feature a flexible backbone capable of continuous bending. Their shape is controlled by intrinsic actuators (e.g., pneumatic or hydraulic systems) or transmission elements (e.g., tendons or flexible tubes) manipulated from one end of the backbone. These robots, with their high length-to-diameter ratio, are ideal for deploying tools or sensors along narrow, winding paths [73]. Continuum robots often emphasize piecewise constant curvature, which simplifies kinematic modelling. They can be represented as a finite series of curved segments, each described by arc parameters transformable into analytical frames [74].

To address performance issues like hysteresis, forward hysteresis modelling is used as a system identification approach to simulate and measure the system's response. The resulting model aids in designing suitable controllers for soft robots. This modelling technique is increasingly applied in soft robot control systems [75].

Model-free Control

Model-free approaches do not require defining parameters. This allows for the development of arbitrarily complex kinematic models based on sample data and sensory noise. It is better suited for highly nonlinear, nonuniform, or unstructured environments where modelling is difficult or impossible. However, the model-based approaches need to be derived from a dataset, which is not always easy to obtain.

Nevertheless, the shortage is apparent. Analysing their stability and convergence is challenging due to their black-box nature. Kinematic controllers assume limited or no dynamic interactions between segments, impeding precise

and rapid movement of soft manipulators. These controllers depend on the steady-state assumption, which may not be available for soft robots. Another relatively new solution is using Model-Free Dynamic Controllers. Combining feedback controllers like sensors and neural network components achieves close-loop control. However, applying the model-free dynamic approach is limited for two main reasons: training time and stability. Training time refers to the time required to train the controller using data from the system. This can be a significant challenge for model-free approaches as they require a large amount of data to learn the system dynamics. Stability concerns refer to the fact that model-free approaches may not guarantee system stability under all conditions. This is because they do not explicitly consider the system dynamics and may be unable to handle disturbances or uncertainties. Despite these limitations, model-free approaches are still a promising solution [76].

2.5.2 Feedback in Control Systems

In a soft robot's control system, whether a model-based control system or a model-free control system, sensors are inevitably used to obtain the soft robot's attitude, position, or control signals. For example, a reinforcement learning navigation system for neurovascular catheters uses external vision to record, analyse, and give feedback to the reinforcement learning model [77], and an optical mouse sensor is used as a user input recognition device when a finite element model is used for soft robot motion control [78]. Sensors are, therefore, an important part of the control system of a soft robot. Most soft robots are currently controlled in an open-loop manner without sensors or other feedback. However, integrating the sensors into a soft robot can provide more information about the robot and ambient conditions. Different sensors also can be combined into a single robot to provide more comprehensive details. Based on the result, this usage or implementation could be divided into two different methods.

Embedded Sensor

Embedded sensors have been widely used in traditional robots for object detection and self-monitoring. In soft robots, however, embedded sensors offer even greater potential due to their ability to conform to flexible structures. Thien developed an imaging method. It is based on an array of infrared sensors embedded in the air chambers of a pneumatically actuated soft machine table. This system can measure the table's deformation, demonstrating the feasibility of internal sensing for soft robotic structures [79]. Bächer has developed an automated sensor design for proprioceptive soft robots. It combines several different kinds of sensors to provide comprehensive information to control the movement of soft robots [80]. In Hammond III's project, they propose a design of a pneumatic artificial muscle equipped with integrated soft optical sensors to evaluate muscle contraction

length and force [81]. These reflective optical sensors are seamlessly incorporated into each muscle to capture light reflection from silicone features. Johns Hopkins University proposed a soft biometric finger with a piezoresistive tactile sensor array integrated at the fingertip. The sensor array has nine texels (sensing elements) arranged in a three-by-three grid, providing spatial information about textures [82].

External Sensor

Soft robots' most common external sensor is a vision sensor, usually a camera. With the development of computer vision, many applications have been integrated into other research fields. As mentioned before, most soft robots have non-linear characteristics and infinite DOF. Computer vision might be a handful solution. Due to the environment or the size of the soft robot, integrating the camera into the robot may not be an option. Providing vision from external surroundings would be the best way out. Li's team has developed a formation control method for the soft robotic fish swarm, which integrated computer vision for a global vision. With a camera on the top to capture the video of the entire group of soft robots, they have successfully controlled robots to form three different formations [83].

2.6 Stereo Vision

2.6.1 Vision Feedback in Control System

Section 2.5.2 has described the sensors used in soft robotics. Internal sensors tend to raise design and manufacturing costs, whereas cameras are the most commonly used external sensors. This section introduces fundamental computer vision concepts and processes, and it proposes a stereo vision pipeline. Depending on the application, computer vision systems can be structured in various ways; the most common configuration follows the image processing pipeline, which includes image acquisition, pre-processing, feature extraction, object detection, object recognition and classification, post-processing, visualization, and interpretation [84].

Image and Acquisition

Image acquisition involves capturing visual inputs and arranging the scene appropriately, including configuring the light source and positioning the camera [18]. Proper light source setup is a critical preparatory step that enhances measurement robustness and emphasizes features of interest [85]. Likewise, careful camera positioning is essential, as the object may be partially occluded by itself or fall outside the camera's limited field of view, leading to information loss [86].

Greg proposed an optimized placement strategy for the light source and camera to mitigate these issues [86].

Pre-processing

This step can simplify subsequent processing and enhance accuracy. Common pre-processing techniques include converting colour images to grayscale, which reduces computational complexity, and normalising images, as many machine learning algorithms require a uniform input scale. Additionally, data augmentation—where perturbed versions of existing images are added to the dataset—exposes neural networks to a variety of changes, thereby improving their ability to recognise objects in different forms and shapes [87].

Background Subtraction Background subtraction is an image pre-processing technique that computes the difference between the current frame and a background frame to isolate the foreground object. MATLAB offers two approaches for this method. One is the 'imsubtract' function, which simply subtracts one image from another or removes a constant value from an image [88]. The other is a more advanced approach, where a foreground detector compares a colour or grayscale video frame with a background model to decide if each pixel belongs to the background or foreground, after which the foreground mask is generated [89].

Feature Extraction

Image data feature extraction involves representing the region of interest within an image as a compact feature vector. A 'feature' is defined as a measurable visual property that provides essential information for subsequent decision-making. Various algorithms exist for feature extraction, and two representative methods are described below.

Skeletonization Skeletonization is a process that converts a binary image by reducing its foreground regions to a skeletal structure while maintaining their original extent and connectivity. This transformation can be performed either by morphological thinning or through the computation of a distance transform. Morphological thinning produces a skeleton, which can be thought of as the centers of bi-tangent circles within the foreground region. While the skeleton is a binary image that represents a simplified version of the original structure, the medial axis transform (MAT) yields a grayscale image where each point on the skeleton is assigned an intensity corresponding to its distance from the object's boundary. Although the terms "Skeletonization" and "MAT" are frequently used interchangeably, there may be subtle distinctions between them [90].

Figure 2.16: Skeletonization [90]

Reeb Graph A Reeb graph is a mathematical construct that captures the evolution of the level sets of a real-valued function defined on a manifold. It serves as a fundamental data structure for understanding and representing the topological features of shapes, with applications in fields such as computer graphics, solid modelling, and visualisation. Its utility extends to tasks including similarity measurement, defect detection in complex models, and the automation of visualisation parameter selection [91].

For the visualisation and interpretation phase in the image processing pipeline described in Section 2.6.2, the results of the skeletonization and Reeb graph processing are presented in Figure 2.16 and Figure 2.17, respectively. These two feature extraction algorithms encompass not only feature extraction but also object detection, recognition, and classification. Finally, the image visualisation step must be tailored to the requirements of different computing platforms or programming languages.

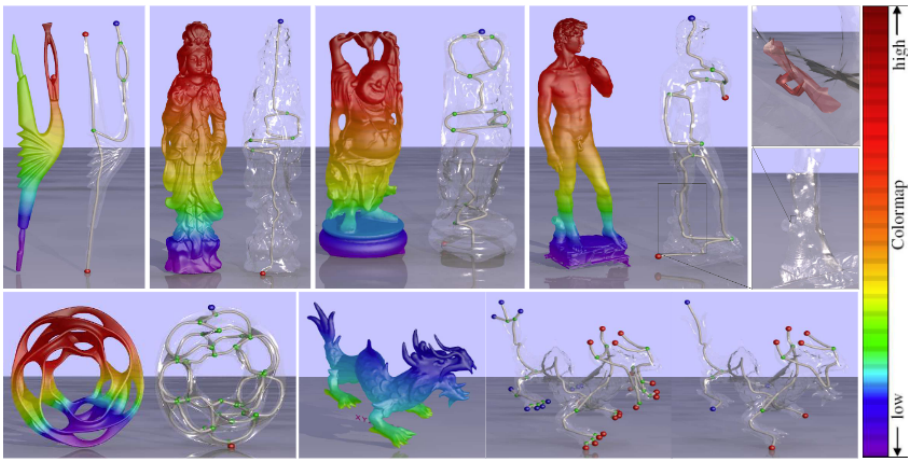

Figure 2.17: Reeb Graph [91]

Stereo Vision

Stereo vision is a computational method used to estimate the depth of objects in a scene by analyzing image pairs captured from two distinct viewpoints. As an

integral part of the image processing pipeline, it follows a systematic approach comprising image acquisition, pre-processing, feature extraction, and 3D reconstruction. However, its primary focus is on extracting depth information through disparity computation, thereby functioning not only as a conventional image processing workflow but also as a specialized technique for obtaining 3D shape features.

The Toyota Research Institute has developed a stereo vision network that has been integrated into its general-purpose robot as the principal perception sensor for household tasks. This network supports positioning, mapping, manipulation, and motion planning, and it effectively addresses challenges posed by light reflections from metal and glass surfaces that can compromise stereo vision accuracy [92].

Currently, stereo vision applications in soft robotics fall into two categories: one involves verifying the accuracy of the soft robot's mathematical model [93, 94], and the other focuses on detecting or analyzing the texture of objects to be grasped by the soft robot [95, 96].

2.6.2 Stereo Vision Pipeline

Stereo Vision Pipeline is a computer vision workflow used to reconstruct 3D depth information of a scene or object from two camera views. It imitates the visual principle of human eye, estimating the distance of each pixel to the camera by analysing parallax. The basic process is as follows.

Cameras Setup The positioning of the cameras is critical for effective stereo vision. The distance and angle between the cameras dictate the pixel displacement in the captured images. As shown in Figure 2.18, O and O' denote the two cameras, X represents the target object, B is the baseline distance between the cameras, and z is the distance from the target object to the cameras. Notably, the disparity of the target object in the images is inversely proportional to z.

When calculating the target object's position, it is necessary to adjust for the angle between the cameras. In Figure 2.18, if the point X is assumed to be at the intersection of the optical axes of the two cameras, then the actual distance from the cameras to the target must exceed z. Otherwise, the 'disparity range' parameter may exceed MATLAB's maximum allowed value when computing the disparity map.

Any changes in the distance or angle between the cameras require a complete restart of the entire processing pipeline.

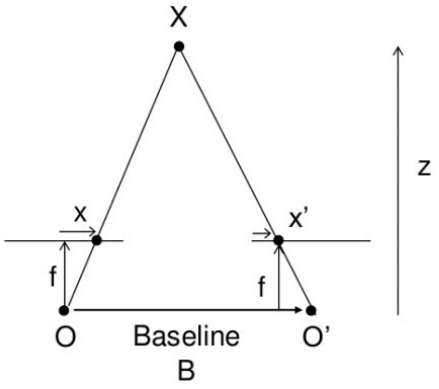

Figure 2.18: Stereo Vision [97]

Stereo Camera Calibration The camera's parameters are essential for computing the differences between images, which requires that the camera be calibrated using a dedicated tool. First, prepare a checkerboard and capture at least ten sets of simultaneous images with two cameras. The checkerboard should cover all four corners of each camera's field of view, and the entire checkerboard must be visible in the captured images. By rotating and tilting the checkerboard, the calibration process can capture three-dimensional information instead of data confined to several planes at different depths. Capture as many sets of images as possible to encompass the full visible range of the cameras and the complete depth range of the target. Finally, use the stereo camera calibration tool to perform calibration—this includes adding images, calibrating, evaluating, refining, and exporting the camera parameters [98].

Disparity Map A disparity map calculates the horizontal shift of each pixel between two images [99]. This technique can be described using a simple equation.

$$\text{disparity} = x - x' = \frac{Bf}{Z} \tag{2.1}$$

x and x' represent the distances between the projections of a 3D scene point onto the image plane and the respective camera centers. B denotes the distance between the two cameras, and f is the camera's focal length. Using this equation, the depth for every pixel can be computed [97].

3D Reconstruction 3D reconstruction involves capturing both the shape and appearance of real-world objects. This process can be achieved through either active or passive techniques. In practice, 3D reconstruction employs one or more images to compute and recreate the object or scene across the XY plane (representing two dimensions) and along the Z axis (representing depth). According to

current algorithms, these methods can be implemented by either active or passive approaches [100]. The active approach is the most prevalent, typically involving techniques such as using a disparity map, structured light, or a LiDAR sensor.

Point Cloud Processing A point cloud is a dataset containing the X, Y, and Z axis information for each point. Since MATLAB is the chosen platform for this project, it offers various point cloud processing capabilities, including pre-processing steps such as denoising and downsampling, as well as post-processing operations like identifying points within a region of interest and locating the nearest neighbours of a given point [101].

2.7 Summary

In current research, soft robots' designs, structures, functions and control systems are diverse. According to the conclusions in Section 2.4, the Kresling pattern is superior to the Yoshimura pattern used in previous student projects, and this thesis will use the Kresling pattern to design and manufacture the OSRA. For its control system, external visual feedback is currently most suitable for soft robots. Monocular vision cannot provide complete spatial information without relying on machine learning or mathematical models for soft robots. It can only identify the horizontal and vertical movements of the robot in the plane. However, stereo vision can provide 3D spatial information for soft robots through the collaborative work of multiple cameras. In the current research on vision-based soft robotic arms, there is a gap in how to use stereo vision to detect 3D spatial information in soft robotic arms. The solution proposed in this thesis is to fill this research gap by using the Kresling Pattern to fabricate a soft robotic arm and constructing a control system based on stereo vision to compute the 3D spatial information of the robotic arm in real-time. Specifically, Chapter 3 proposes the scene setup of the stereo vision camera and the specific manufacturing method of the soft robotic arm. Chapter 4 describes the selection of manufacturing materials, the response and state of the robotic arm, and the structure of the control system.

Chapter 3

Design

In the design of this thesis, the OSRA uses the Kresling Pattern as the geometric structure. The entire OSRA is like an octopus arm with a claw, with one end fixed and attachable to the top of a frame or box and the other end free yet equipped with a gripper. By using the origami structure, it should have infinite DOF. At least three origami actuators are used to form an integral arm to ensure that the arm can be bent in different directions. A pneumatic driving system will be used to drive the arm, and tubes will be used to connect to the origami actuators and the driving system. The whole arm should be airtight to allow the pneumatic drive to move the actuator. A pressure sensor or origami actuator will be integrated into the drive system to monitor airtightness and ensure proper operation. The stereo vision system is used as an external sensor to identify the OSRA's spatial position and shape changes (compression, extension, bending). The control system takes the user operations (buttons) as input, the pressure sensor and the stereo vision calculation results as feedback signals, and the final outputs a signal to activate the drive system to drive the soft robotic arm. Detailed design will be covered in this chapter.

3.1 Soft Arm

This thesis proposes an OSRA and its control system. The first step is to design a soft robotic arm. The OSRA design incorporates the findings of the literature review. Specifically, the Kresling pattern is superior to the Yoshimura pattern in terms of thin-walled cylinders subjected to twist buckling due to its ability to tolerate large and complex, yet still predictable, shape transformations [102]. The whole arm should be able to perform telescopic and bending movements while also being repairable, with parts that can be quickly replaced. This section will only discuss the design of the soft arm and the selection of materials and analysis will be discussed in Chapter 4. This soft robotic arm design has four primary components: origami actuators, a gripper, connecting and sealing pads, and a frame.

The original Kresling pattern has a defect: it will rotate during the compression and extension process because the valley folds are not horizontal or vertical. The whole origami actuator is composed of several units using the Kresling pattern, which are vertically combined. As shown in Figure 3.1, it is composed of 5

units. The original Kresling Pattern is a surface composed of two triangles with

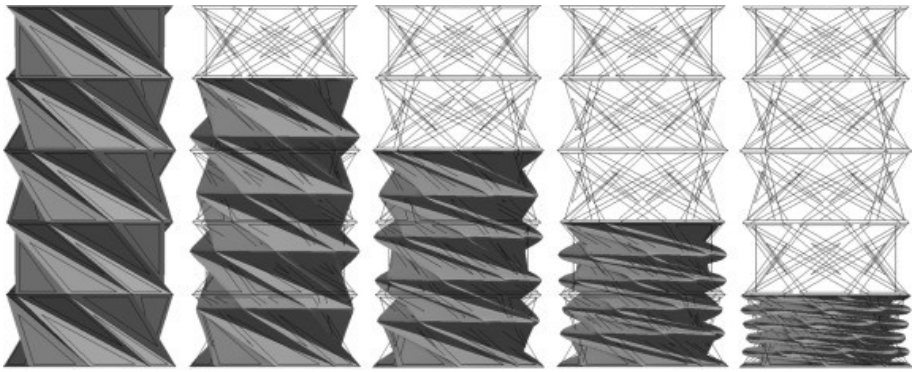

Figure 3.1: Original Kresling Pattern Actuator with Different Compression Ratio [103]

long diagonal edges mirrored. Six identical faces surround the centre of a regular hexagon with a side length to form a single unit. The base of the triangle is denoted by a, the short diagonal by b, the long diagonal by c and the angle between the long diagonal and the base by δ. Each unit's rotation angle during compression is denoted by θ. The maximum rotation angle of each unit can be calculated using the following formula [104].

$$\theta = 2\arcsin\frac{b}{2a} - 2\arcsin\frac{b\cos\delta}{2a} \tag{3.1}$$

This rotation problem increases with the length of the origami actuator increase. To avoid this problem, horizontally mirror two adjacent units so that the rotation directions of the two units are opposite, thus avoiding this problem. As shown in Figure 3.2. The adjusted design of the origami actuator is shown in Figure 3.15.

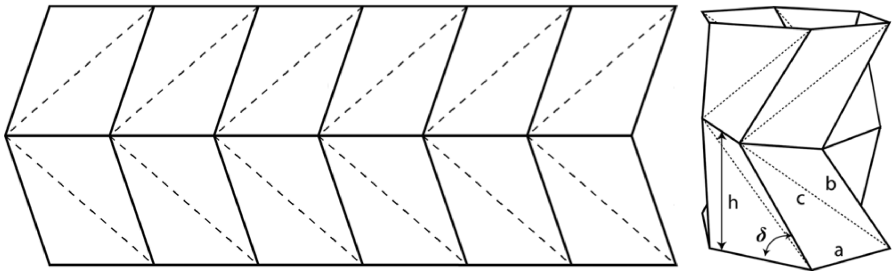

(a) (b)

Figure 3.2: Mirrored Kresling Pattern

In OSRA's design, it will use three identical origami actuators. The three origami actuators are made with paper, Sellotape, acrylic glass, and EcoFlex Rebound 25. These materials are easy to access, and the 120gsm paper and Sellotape can provide good cohesion and air sealing. The comparison of different material

combinations will be covered in Chapter 4. However, the three origami actuators' top and bottom surfaces must be well sealed to ensure the airtightness of the actuator. Therefore, several parts are designed to seal the ends and can be screwed into a designed frame. Figure 3.3 shows the six parts used to seal the ends. Figure 3.4 shows the frame.

In Figure 3.3, two more significant parts are called connector pads and are used to fix the three origami actuators together as one object. The left pad is used to attach the bottom surface, and the centre round hole is used to attach the soft gripper. The two connection pads are cut from acrylic glass. The four smaller parts are called sealing pads. The two 34 mm side-length gaskets are 3D printed, and their size can fit into the top and bottom openings of the unsealed origami actuator. The two 35 mm gaskets are cut from acrylic glass and provide a good air seal by covering the 34 mm gaskets with a layer of Rebound 25 silicone and attaching the 35 mm gaskets to the silicone with screws and nuts to form a sandwich structure. The detailed steps are described in Chapter 3.5. It should be noted that the 35 mm gasket is not a necessary part, and its importance lies in the individual air tightness testing of individual origami actuators. These two gaskets can be omitted, and the two connector pads can be used directly.

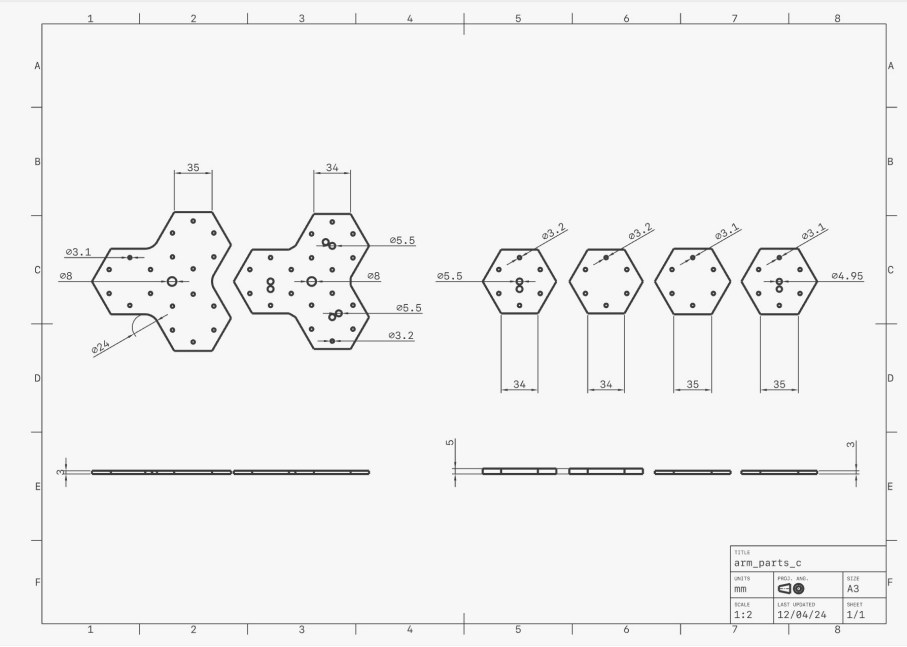

Figure 3.3: Connector Pads and Sealing Pads

In Figure 3.4, a frame is made with wood board and cut by a laser cutting machine. This design gives the OSRA a fixed top end and a free bottom end (gripper). The frame can be seen as a reference object in stereo vision to locate the soft arm.

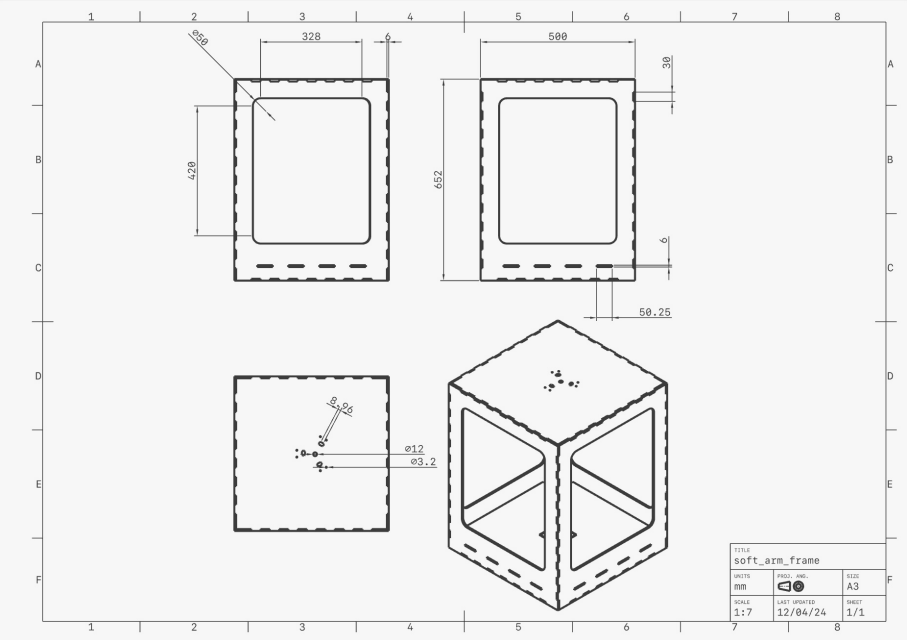

Figure 3.4: Frame

Rubber gripper uses an open-source CAD design [105]. The open-source file provides several parameters to adjust the shape and size of the gripper, including the number of branches, wall thickness, air chamber grid height, etc. This open-source design allows altering the original design to adapt to different applications or scenarios. EcoFlex 30 has been chosen as the material for fabrication. This material is easy to store and use, can tolerate 200 psi pressure, and has no special requirement for fabrication; all procedures can happen at regular room temperature and environment. These characteristics make it strongly suitable for gripper fabrication. Figure 3.5 shows the gripper bending.

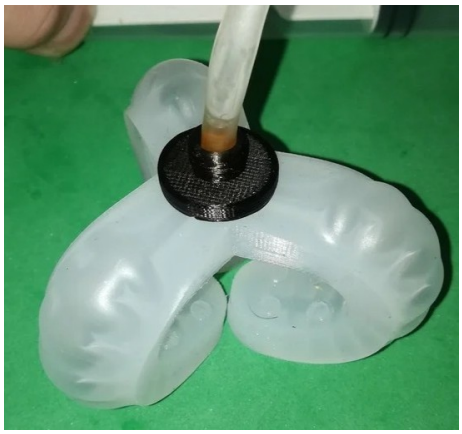

Figure 3.5: Soft Gripper

In the open-source CAD design, a connector (the black part on the gripper in Figure 3.5) connects the tube to the gripper. However, this part is glued to the

gripper with EcoFlex30, but the binding ability of PLA plastic (3D printing material) and EcoFlex30 is not strong, so the parts in Figure 3.6 are designed both for 3D printing. The left part's bottom disc needs to be inserted into the gripper through an open cut on top of the gripper, and then the top part is inserted into the hose to connect the gripper to the pneumatic drive system. Finally, the right-hand part is placed over the left-hand part, and the two parts are firmly pressed together from above and below with a clicking sound. This nesting structure ensures a tight hose connection and allows the gripper to be clamped by the disc-shaped undersides of the two parts. Install the gripper to the arm requires inserting the top of the left side part into the centre round hole of the connecting pad, which was mentioned before. To further improve the airtightness, the outsides of the two parts can be re-sealed with EcoFlex30.

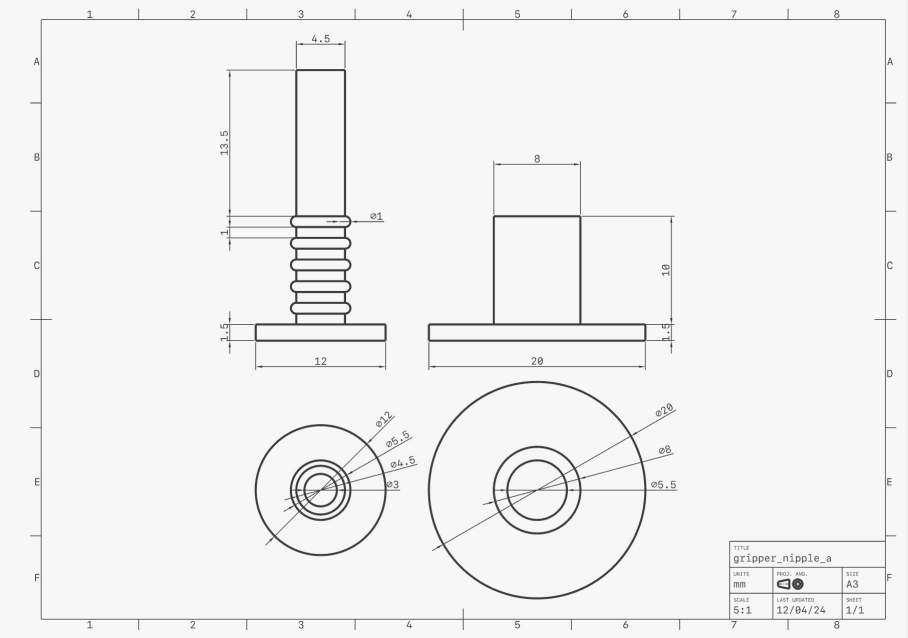

Figure 3.6: Gripper Connectors

3.2 Pneumatic-driven System

The next question is how to make a soft robotic arm move. In this thesis, a pneumatic drive system is used, which is the basic system of the soft robotic arm. Its proper functioning affects all movements of the soft robotic arm. This pneumatic drive system includes a user input, an output, and a control unit. The components of these three parts are buttons, relays, electromagnetic valves, and an ESP32 microcontroller.

The six buttons on the user input side represent the air deflate, inflate, gripper and origami actuators 1 to 3. A combination of two buttons performs each operation. For example, pressing the Inflate + Actuator 1 button simultaneously will

cause Actuator 1 to extend; conversely, pressing the Deflate + Actuator 1 button simultaneously will cause Actuator 1 to compress. It is also possible to press several buttons simultaneously, but the pneumatic drive can only be activated in one state, either deflate or inflate; i.e. pressing the Deflate and Inflate buttons simultaneously will not cause the pneumatic drive system to perform any actions.

A two-channel solenoid relay module used as an output is connected to two three-way valves (the main valves that connect with the air pump), and an eight-channel solenoid relay module is connected to eight secondary two-way valves. The three-way valves ensure that the air pump does not stop due to a blocked air path when all two-way valves are closed. Two secondary two-way valves control the inflation and deflation of one origami actuator. Two short tubes are embedded at the end of the origami actuator, and their connecting point can be seen in the connection pads in Figure 3.3, that is, the three sets of two connected circular openings on the right connection pad.

Taking an origami actuator as an example, the connection path of the inflated state of the pneumatic drive system is a three-way valve, a two-way valve, and an origami actuator. This path is activated when the user simultaneously presses the Inflate button and the Origami Actuator 1 button. Assuming that the three-way valve switches from outlet 1 to outlet 2 (outlet 1 is not connected to anything and outlet 2 is connected to the two-way valve), the two-way valve opens, and air is fed to origami actuator 1, causing origami actuator 1 to expand. Still, since the other two origami actuators do not expand, the arm bends opposite to origami actuator 1. If the user simultaneously presses the air Inflate button and the Origami Actuator 1 and Origami Actuator 2 buttons, the two identical air inflate paths open, but Origami Actuator 3 is not inflated, which causes the arm to bend in the direction of Origami Actuator 3. If the Inflate button and the Origami Actuator 1, Origami Actuator 2 and Origami Actuator 3 buttons are pressed simultaneously, the three inflate paths open, causing all three origami actuators to expand simultaneously and the arm to elongate.

As seen from the above user input and output, the control unit needs sufficient interfaces or ports to connect all components. It also needs to have the ability to communicate with a computer using the I2C communication protocol to connect to the air pressure sensor and be able to communicate with the computer to send the status information or readings of all components in the pneumatic drive system to the computer or receive information from the computer for further processing. Considering the above requirements, ESP32 is a good choice. It integrates 36 general-purpose GPIO interfaces, a Bluetooth module, a WiFi module, and two I2C communication controllers. It also supports UART protocol and communication with the computer using a serial port. It also supports using FreeRTOS technology to achieve approximate multi-threading capabilities using time-slice task rotation.

Figure 3.7 shows a block diagram of the pneumatic drive system. The circuit

diagram showing the connection between each electronic component is on the left-hand side of the figure. Black lines indicate the connections between components. The right side of the figure shows the piping diagram, which shows the gas path between the primary three-way valve, the secondary two-way valve, the three origami actuators and the gripper. The blue lines represent the gas pipes.

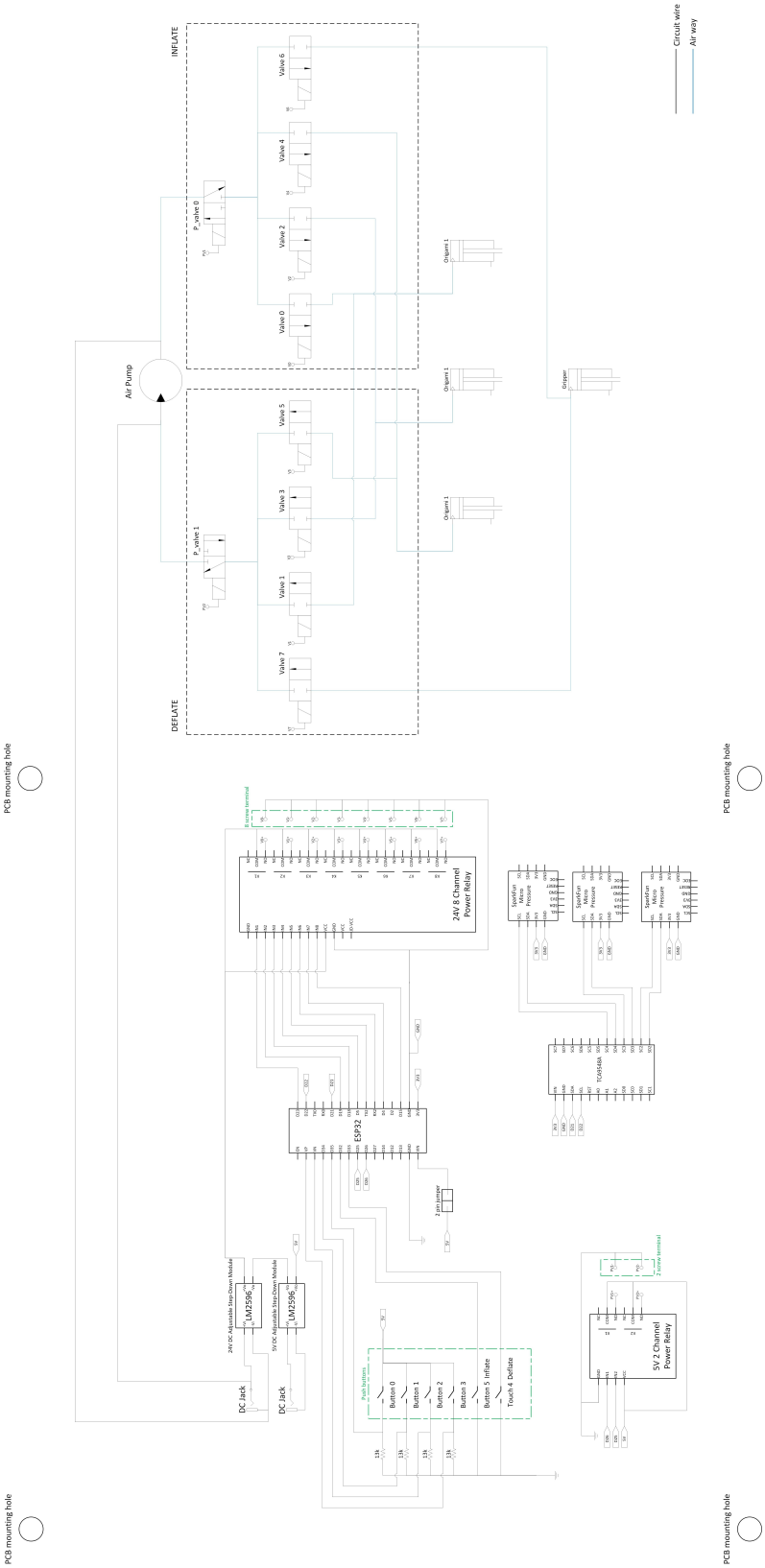

Figure 3.7: Pneumatic-driven System Diagram

3.3 Control System

Like other soft robots, the OSRA has an infinite number of degrees of freedom. It is expected to be able to bend, compress and stretch with great flexibility.

3.3.1 Sensors in Control System

A pneumatic drive system controls the three origami actuators. The compression or extension of one actuator causes the other two to bend. The airtightness of the three actuators will allow the air pressure sensor to read the pressure inside the three actuators. The air pressure sensor selected is the Sparkfun MicroPressure Sensor [106], which is equipped with Honeywell's $25\,\mathrm{psi}$ piezoresistive silicon pressure sensor as a core, with I2C communication protocol and a protective cover. This gives the air pressure sensor a calibrated pressure measurement range of $1\,\mathrm{psi}$ to $25\,\mathrm{psi}$, a measurement frequency of $1\,\mathrm{Hz}$ and provides an Arduino library to read the pressure reading in multiple units. Its protective cover can also be connected directly to the pneumatic drive system hose.

Figure 3.8: SparkFun MicroPressure Sensor

Therefore, whether it is the pneumatic drive system inflating or exhausting or the three origami actuators being deformed by external forces, the resulting pressure changes will cause the output of the air pressure sensor to change.

Stereo vision can detect the overall length of the arm and changes in position in space, such as horizontal displacement and bending in different directions.

In the above two components, the air pressure sensor readings and the stereo vision output results are used as feedback signals. The control system must receive these two signals in real-time and ensure that the user's control input is appropriate while avoiding structural damage to the origami robot arm caused by excessive stretching and bending and avoiding damage to the air pump in the pneumatic drive system caused by excessive compression.

3.3.2 Control System Diagram

Figure 3.9 shows a block diagram of the control system. The input signal generated when the user presses a button in the pneumatic drive system is sent to ESP32. ESP32 controls the valve to move the origami actuator. The final output is the movement of the origami arm.

Two feedback signals are involved in this process: the readings from the air pressure sensor and the output signal from the vision system.

The air pressure sensor is integrated into the pneumatic control system, so its readings can be obtained directly by ESP32. It is to obtain the air pressure changes in the three origami actuators in real-time. As the pneumatic drive system causes the air pressure in the origami actuator to increase (more gas) when it is in the inflation state and decrease (less gas) when it is in the deflation state, this characteristic can be used to determine the current action of the origami actuator based on the change in air pressure. A threshold is set based on the air pressure readings at maximum compression and maximum extension of the origami actuator. The pneumatic drive system will stop before the threshold is reached, i.e. before it inflates or deflates, thereby protecting the geometric structure of the origami actuator from damage.

The vision system acts as an external sensor, with the stereo shell capturing the spatial position of the origami actuator in real-time to calculate the length, orientation and degree of bending of the origami actuator. Since the internal air pressure of the origami actuator can be affected by external forces such as load weight and external pressure, the feedback from the vision system can provide a second feedback signal to achieve the same purpose of protecting the geometry of the origami actuator. As it is not in the actuator system but in an external computer, the length is converted into a pneumatic pressure value and sent to the ESP32 to control the pneumatic drive system. The working principle of the vision system is described in Section 3.4.

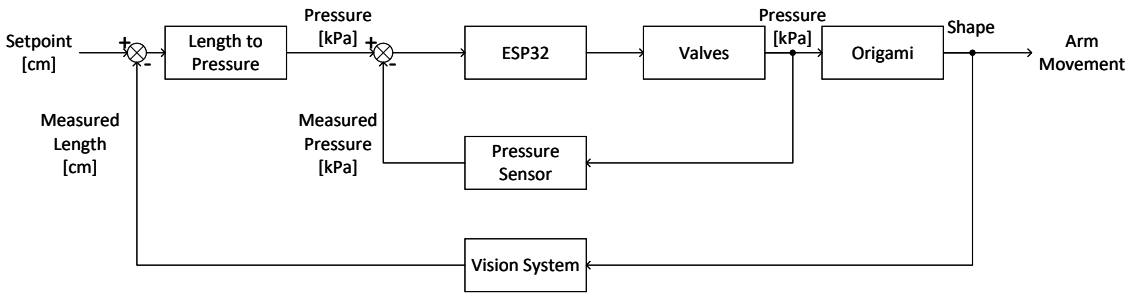

Figure 3.9: Control System Diagram

3.3.3 Dashboard of Control System

Figure 3.10a shows the user dashboard on the computer, which displays the spatial position of the origami robot arm, the status of some components (buttons, three-way valves and two-way valves) in the pneumatic drive system, and the three pneumatic actuators' real-time internal air pressure readings, corresponding to the three air pressure sensors. It can be seen that the user dashboard is divided into three parts from left to right. The first and second parts represent the movement of the soft robotic arm in the XY and ZY planes, respectively.

OSRA Spatial Information

To make the movement of the robot arm clearer to see, the robot arm identified by stereo vision is divided into 10 vertical parts. In each part, calculate the median of its x-coordinates and y-coordinates and use the result as the centre point of this part. The plotting function then connects the 10 points to draw the line diagram.

The ZY plane polyline graph also divides the soft robotic arm into 10 vertical parts, and the centre point of each part is obtained by taking the median of the Z and Y coordinates of each part in the ZY plane. The remaining steps are the same as the XY plane line graph.

The two line graphs both have a unit of cm. In the ZY plane, the Z axis does not start from 0 because the calculation result of stereo vision takes the camera as the starting point. Therefore, the distance from the camera to the soft mechanical arm is about 140 cm (considering the two line graphs combined as the vertical line of the stereo geometric centre of the soft robotic arm, this distance needs to consider the distance from the vertical line to the surface).

Pneumatic System Information

This area contains two parts:

The first part shows a bar chart of the push button, primary three-way valve and secondary two-way valve in the pneumatic drive system. The X-axis of the bar chart is labelled with the names of the different components, i.e. the corresponding readings represent the status of the component. The push button and all the valves work in the same way; they only have two states: 0 and 1, with 0 meaning not pressed/closed, and 1 meaning pressed/opened. Therefore, the maximum value of the Y-axis is 1, and the minimum value is 0. The minimum value of -1 is seen on the Y-axis in the chart because MATLAB sets the Y-axis to the vertical centre of the chart by default when no data is passed in. After data is entered, the minimum value of the Y-axis will change to 0.

The second part is a line graph that records the real-time data from the three air pressure sensors. There are three lines in the graph, cyan, blue and orange, representing the real time readings of the air pressure sensors 1-3, and the internal air pressure of the origami actuator 1-3. The unit of measurement is kPa. As

MATLAB continuously imports data into the line graph, the line graph is continuously compressed to the left, making it difficult to distinguish the data. Therefore, the number of data displayed in the line graph is limited to the last 40 data points, and the data number is marked on the x-axis. These 40 data points correspond to readings taken over a period of approximately 28-30 seconds. This timing inaccuracy is due to the use of FreeRTOS by ESP32 and cannot be resolved at this time. This problem is described in detail in Chapter 4.

This user dashboard provides a more intuitive view of the spatial movement of the OSRA and allows users to monitor the status of the pneumatic system and soft robotic arm in real-time.

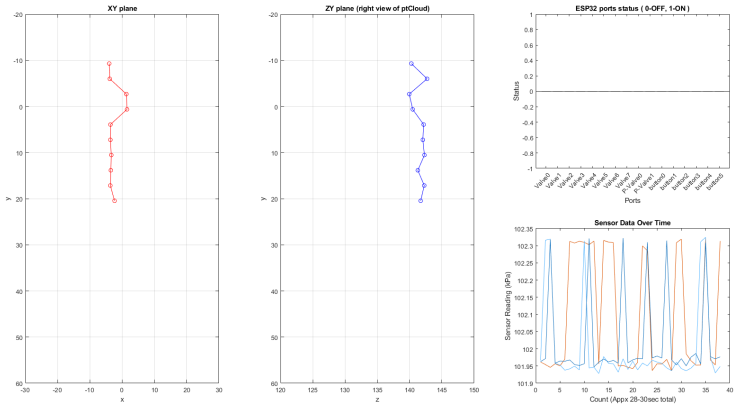

(a)

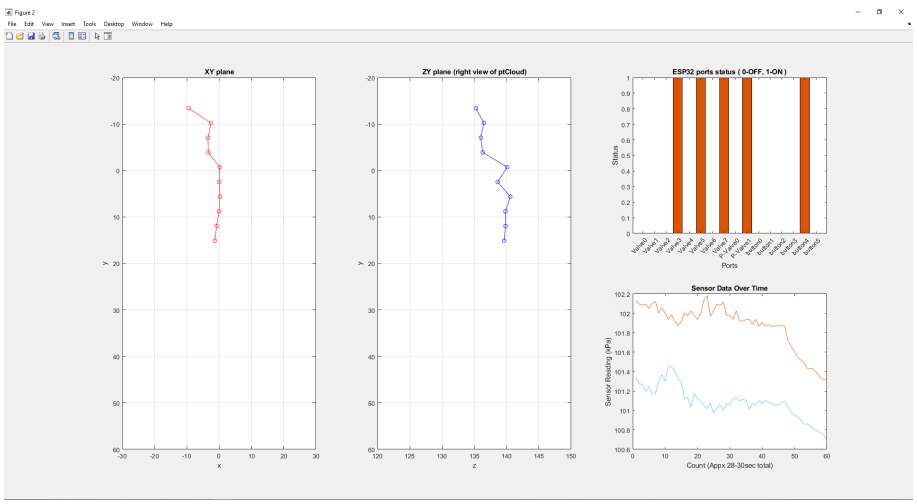

(b)

Figure 3.10: User Dashboard

3.4 Stereo Vision Scene

The stereo vision scene is set up to perform 3D measurements of the soft robotic arm. The accuracy of the measurement results will affect the accuracy of the 3D scene reconstruction of the identified soft robotic arm and will affect the accuracy of the feedback signal in the control system.

3.4.1 Stereo Shell

The first step in establishing stereo vision is to set up two or more cameras to form a stereo camera. In this thesis, two cameras are used to form a stereo camera. Assume that after the stereo camera is calibrated, any slight movement of either camera causes the baseline and intersection angle of the cameras to change. To avoid this problem, the stereo shell shown in Figure 3.11 has been designed. It is intended to provide an easy-to-use stereo camera scene. It gives a fixed baseline and intersection angle between the two cameras. This combines the two cameras into a single object that can be placed anywhere. Because the baseline and intersection angle of the two cameras are fixed, stereo camera calibration is only required once.

The two cameras are placed in two blocks, with an opening at the back of the block for the camera's cable. The housing is modular, and the angle of intersection of the two cameras can be adjusted to accommodate target objects of different sizes and different distances between the camera and the target object.

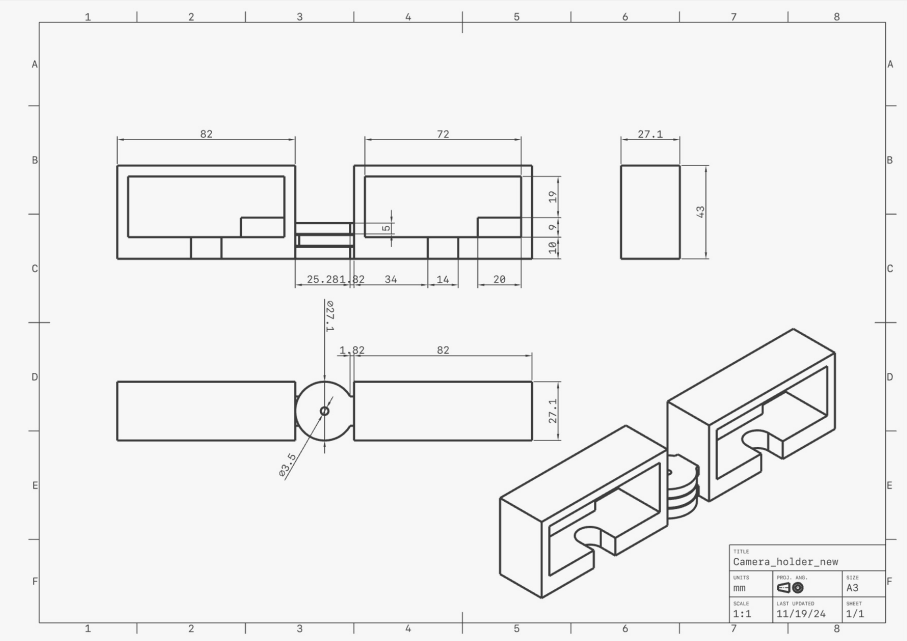

Figure 3.11: Stereo Shell

3.4.2 Stereo Vision

By following the pipeline in Section 2.6.2, a basic binocular vision system can be established, which can output stereo vision information and extract the desired target's spatial information. The pipeline revolves around stereo vision using MATLAB as a platform, and all the functions, algorithms, and features involved are available in MATLAB.

The stereo vision system uses a stereo shell to acquire real-time input video and return a point cloud object. In addition, the system provides an interface for displaying the calculated disparity map and point cloud map. As shown in Figure 3.12, the disparity map is on the left, where different colours indicate the object's disparity value, with blue being the smallest and red being the largest. The larger the disparity, the closer the object is to the stereo vision shell; the point cloud is on the right, where the person in the centre can be observed. Other items in the environment are not fully displayed due to the camera issue, and this problem will be analysed in Chapter 4.

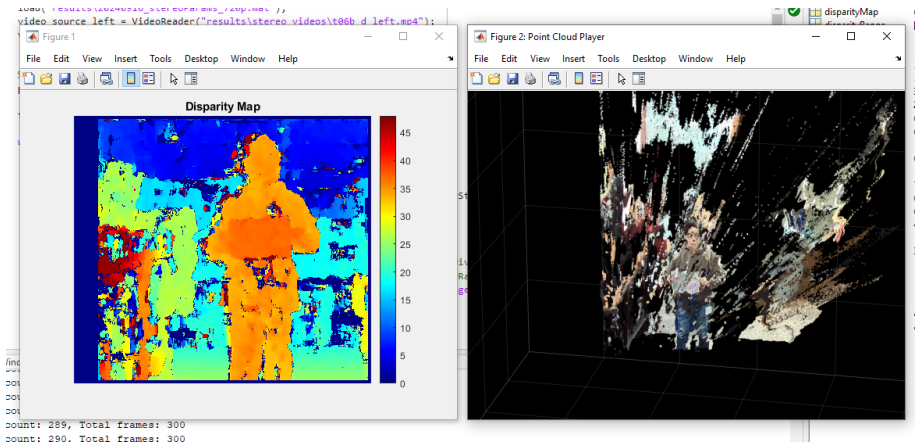

Figure 3.12: Stereo Vision Output

3.5 Fabrication

This fabrication method pertains to the fabrication of any origami-inspired soft arms. The materials applied throughout the production include A3-size 120 gsm paper, Sellotape, Rebound25, and the connecting and sealing components referred to in the preceding sections.

The Kresling Pattern is a modification of Matthew's design [59], which maintains the angles of the basic triangles, adjusts the lengths of the three sides, enlarges the basic triangles, mirrors the triangles to form a rhombus, and then arranges and combines these triangles to obtain the desired pattern size. An overlap area was designed on both the left and right sides to facilitate the bonding process as a cylinder. Concurrently, the bonding areas have been kept as small as

possible to prevent any adverse effects on the behaviour of the actuators due to the varying thicknesses. Additional supplementary mesh areas were created at the top and bottom to bond to the connecting components.

Figure 3.13 shows the Kresling Pattern design. The dotted lines represent a valley, which means to fold inside, and the solid lines represent a mountain, which means to fold outside.

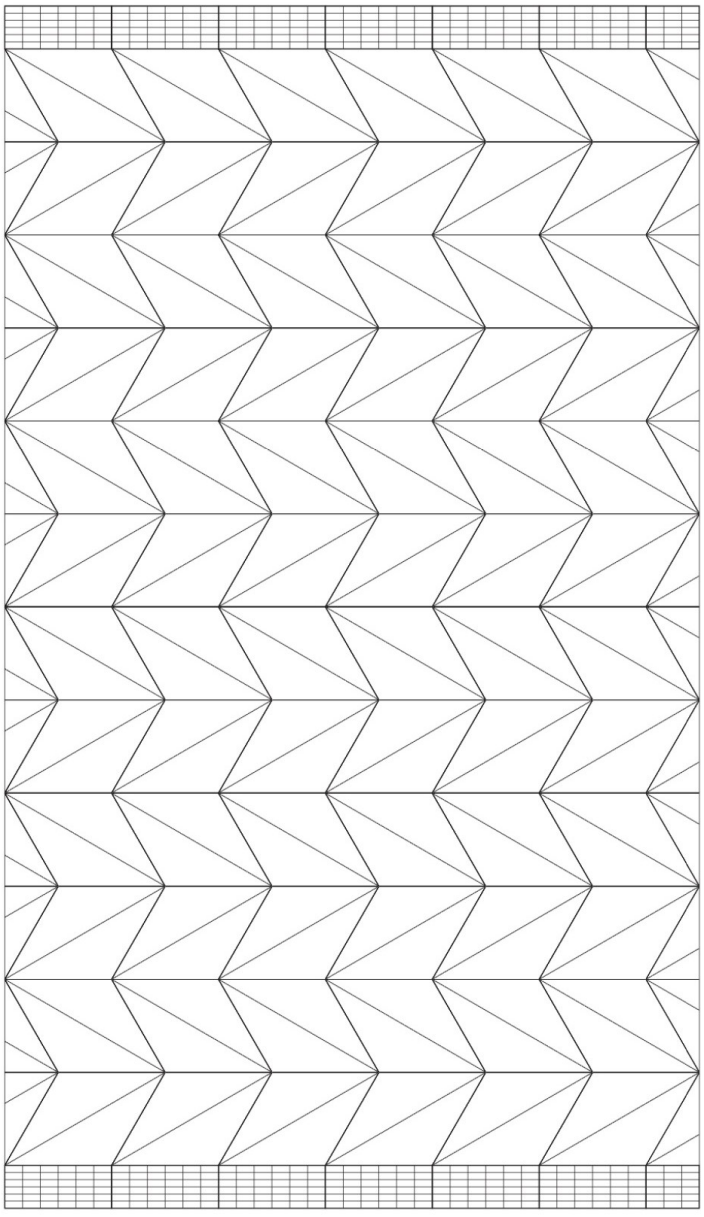

Figure 3.13: Origami Design

Figure 3.14 illustrates the fabrication process of the Kresling Pattern origami actuator. The pattern was printed on A3-sized 120 gsm paper, as shown in Figure 3.13. All horizontal solid lines were folded to form a continuous zigzag pattern across the sheet. The first section on either the left or right side was kept

folded while the remainder was unfolded. Within the folded section, dotted lines were creased in one direction and solid lines in the opposite direction, systematically alternating between mountain and valley folds.

After completing the folds within a section, that portion was unfolded, and the adjacent section was folded in half to repeat the process. Once all sections had been folded, the paper was fully unfolded, revealing a uniform pattern of alternating peaks and valleys. The patterned paper was then wrapped around a wooden mandrel and secured into a cylindrical shape using double-sided tape, with the seam reinforced by clear adhesive tape. The resulting Kresling Pattern structure is shown in its final form in Figure 3.15.

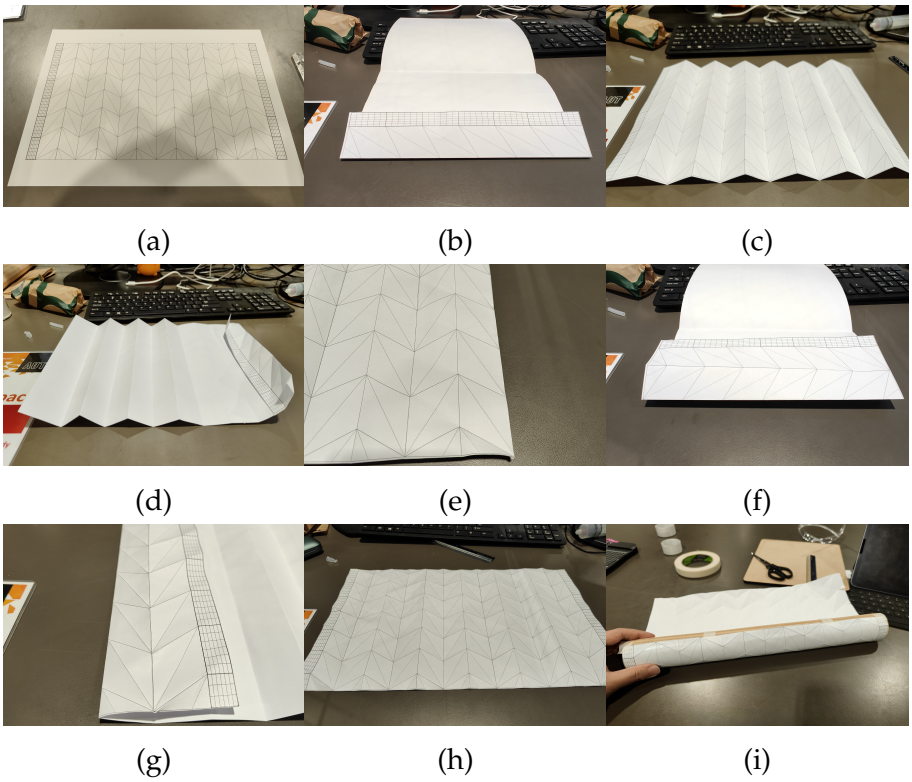

Figure 3.14: Origami Actuator Folding Procedure

To ensure airtightness, both ends of the origami structure were sealed using the components depicted in Figure 3.3, which include two 3D-printed hexagonal parts and four laser-cut acrylic glass components.

BM3 nuts were inserted into the designated slots of the 3D-printed parts (Figure 3.16a). Notches were made at both ends of the origami cylinder to facilitate fastening, and the hexagonal components were adhered using double-sided tape. A containment barrier was formed using masking tape with a height exceeding 6 mm, into which 14 ml of mixed Rebound 25 silicone was poured and allowed to cure. After curing, the acrylic glass components were affixed using M3 screws. Figure 3.16d illustrates the difference between screwed and unscrewed conditions, where air bubbles were visible at the unscrewed interface (highlighted with

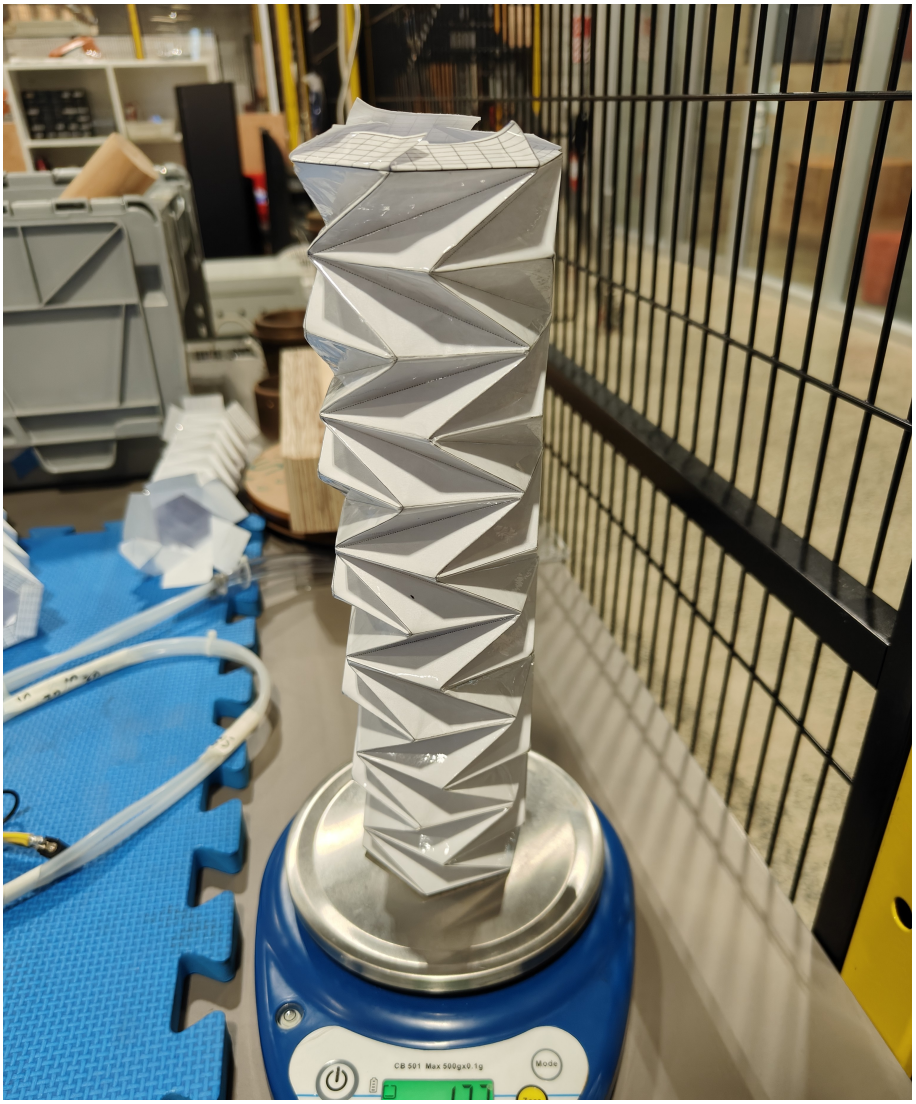

Figure 3.15: Finished Origami Folding

red circles).

Note that the 3D-printed component featuring two central holes was pre-fitted with a tubing insert prior to attachment. The insertion depth of the tube was set to match the fully folded length of the origami actuator; for example, in the configuration shown in Figure 3.16f, the tube was inserted to a depth of 20 mm. This sealing process was repeated to produce three origami actuators. The three completed units are shown in Figure 3.17.

The fixed frame of the soft robotic arm is shown in Figure 3.4. The three origami actuators were assembled into a integrated structure using the two largest components from Figure 3.3, and mounted onto the frame. The fully assembled soft robotic arm is presented in Figure 4.16.

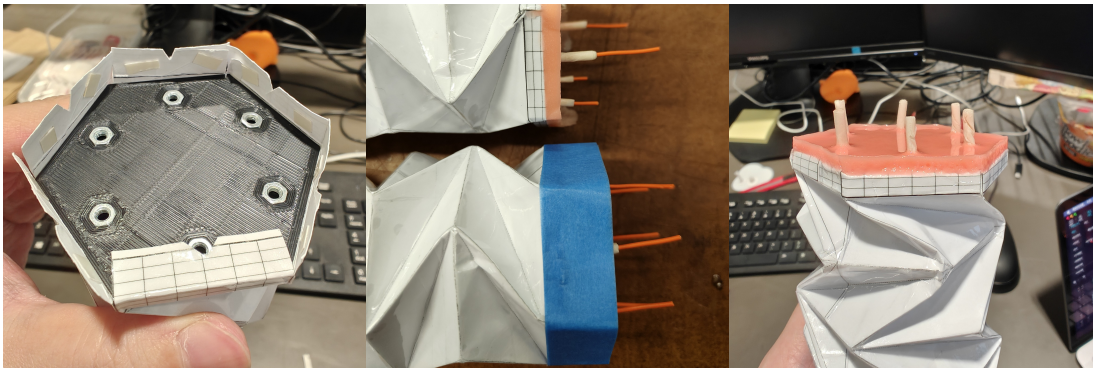

(a) (b) (c)

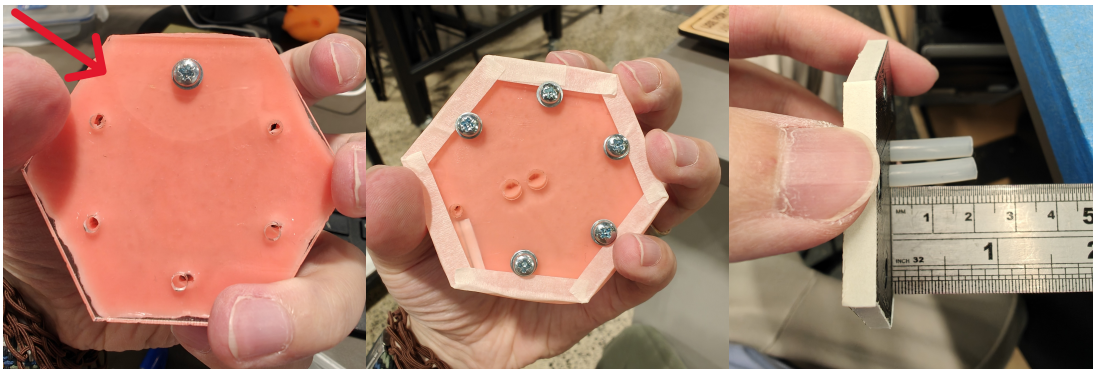

(d) (e) (f)

Figure 3.16: Origami Actuator Sealing Procedure

Figure 3.17: Temporary Assembled Origami Actuator

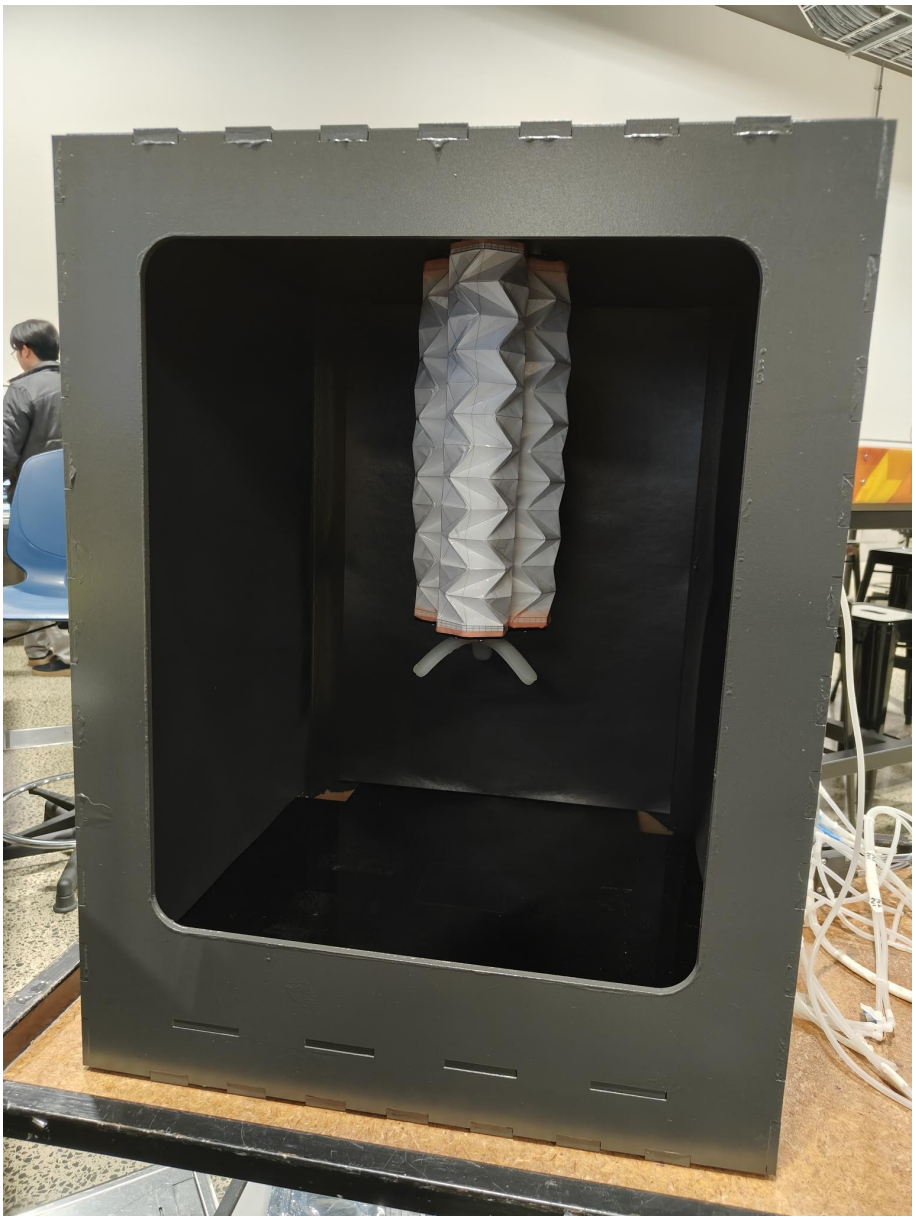

Figure 3.18: Assembled Soft Robotic Arm

Chapter 4

Results

Chapter 3 introduced the OSRA manufacturing method, material selection, assembly techniques, and the control system, providing a foundation for further investigation. Building on this foundation, this chapter evaluates the fabrication method, investigates material selection, and explores assembly techniques through a series of experiments. Finally, the effectiveness of the vision-based control system and the pneumatic system is assessed. These experiments validate the feasibility of the proposed OSRA fabrication and control methods and provide insights for further improvements.

4.1 Fabrication Method Selection

As Chapter 2 mentions, the current soft robot manufacturing methods and the selected materials affect each other. Combining the mentioned materials, EcoFlex is an easy-to-use manufacturing material, so the items related to EcoFlex are selected for reference in the initial selection of manufacturing methods.

4.1.1 Casting Mould

The casting method is the manufacturing method chosen for most projects using EcoFlex. It seems like a simple and feasible method to use a 3D printer to create a suitable mould and then pour EcoFlex into the mould.

Rotating Casting Mould

According to Li's manufacturing method [104], he used a 3D printer to print a shell using a Kresling Pattern. He poured a mixture of EcoFlex and DragonSkin (silicone-based materials of different hardnesses produced by the same company) into the shell. By continuously rotating the shell, the mixture is allowed to flow inside, thus evenly covering the inner surface of the shell.

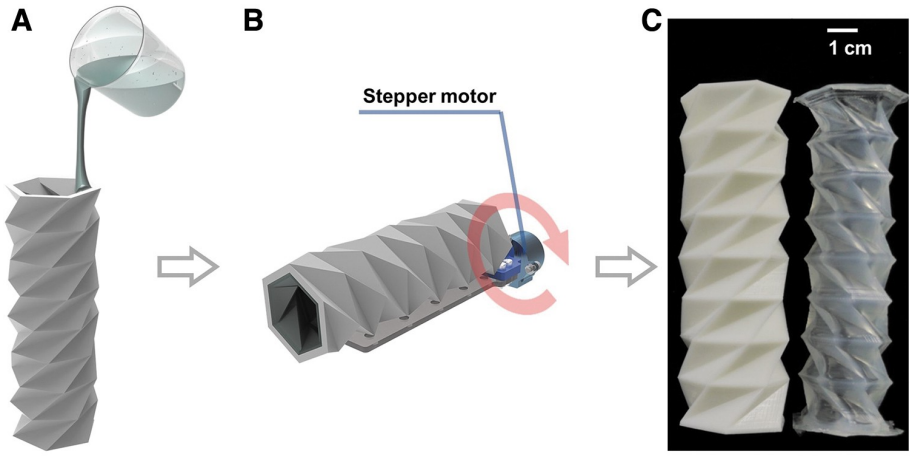

Figure 4.1: Li's Casting Fabrication Method [104]

However, there is a problem with his manufacturing method. As seen in Figure 4.1, the mould rotates eccentrically, which will cause uneven flow of EcoFlex. Also, he did not mention the material used for 3D printing, so the second problem is how to remove EcoFlex completely after it has cured.

The casting mould was redesigned to solve the above two problems. As shown in Figure 4.2. A central axis was used to ensure that EcoFlex could evenly applied to the inner wall. The overall shell was cut into five sections, with a Kresling Pattern design used for the middle three sections. Holes were added to the first and last sections to facilitate the use of a syringe to add EcoFlex into the inside, and a connecting shaft was added to connect the stepping motor to rotate the casting mould.

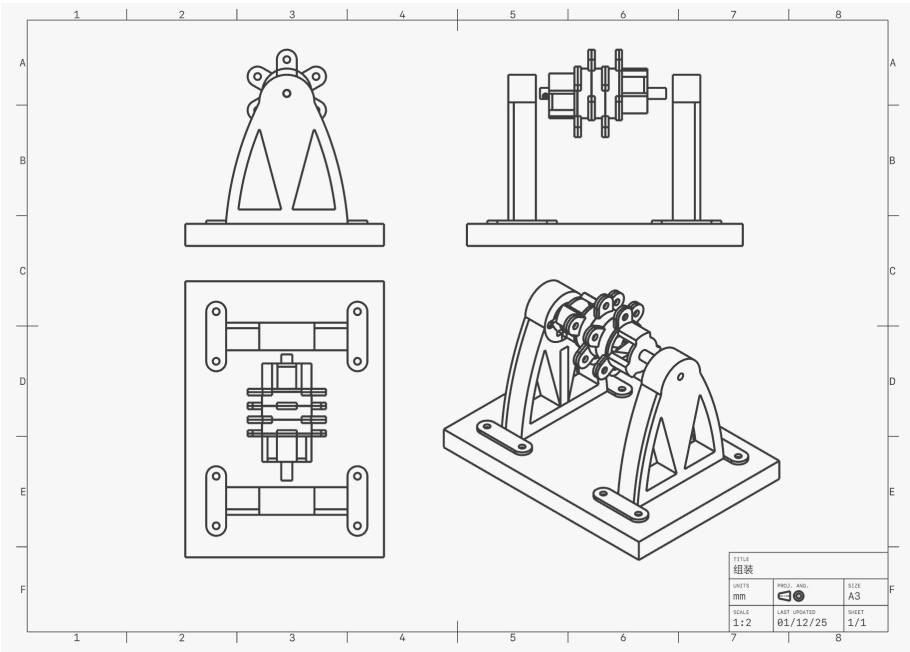

Figure 4.2: New Casting Mould Design

This method was abandoned after several attempts, as the high viscosity of EcoFlex made it challenging to achieve an even coating on the inner surface.

Manual Casting Mould

Although the results of the spin model did not meet expectations, some of the parts can still be used. Because EcoFlex is not evenly coated on the inner surface of the Kresling Pattern parts during spinning, try to manually brush EcoFlex onto the inner surface and allow the excess EcoFlex to flow out by gravity. After the painting is complete, place the mould on a support to ensure that no surface will block the flow of EcoFlex from the hollow part. After the EcoFlex cure, paint again and repeat 5 times.

Figure 4.3: Manual Casting Mould

As shown in Figure 4.3, after the manual painting process, the Kresling Pattern structure is clearly visible in the product. However, the valley part is thinner and more damaged than the mountain part. This is because the valley and mountain in the mould are the opposite of the valley and mountain in the product. As a result, the Ecoflex deposited on the valley of the mould caused the product's mountain to become thicker. Because each section of the mould is similar to a ring structure of a hexagon, when multiple moulds are stacked, it is not possible to add an internal core to limit the thickness of EcoFlex in different parts. If an internal core is added, it will make it more difficult to remove the product.

Therefore, it is challenging to use a casting mould to manufacture a resonator that conforms to the Kresling pattern, and other solutions need to be found.

Sheet Casting Mould

When using a casting mould, the biggest problem is that it is not possible to ensure that EcoFlex forms an even plane. Therefore, in order to ensure that the finished product has an even plane, try unfolding the Kresling Pattern as a flat pattern to perform casting.

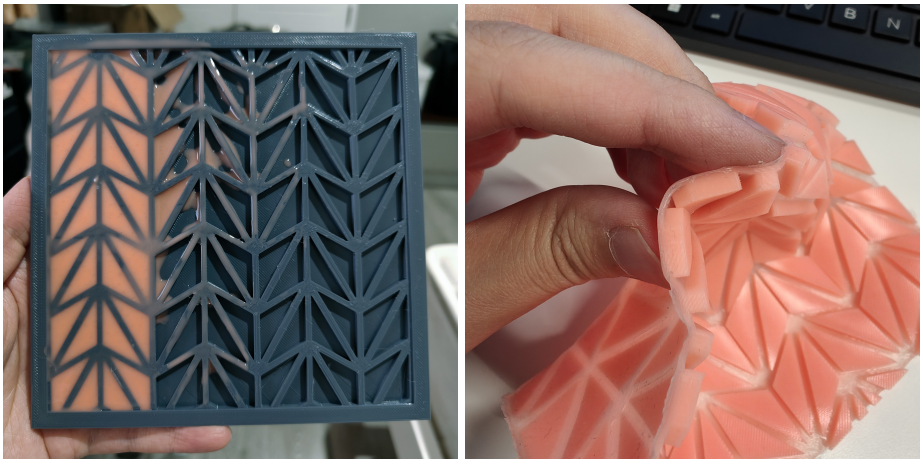

Figure 4.4: Sheet Casting

As seen in Figure 4.4. A casting mould was created using a 3D printer, and the structure of this mould conforms to the Kresling Pattern. Rebound25 (a product of the same company as EcoFlex, but with a different naming convention due to its different hardness and elasticity; Rebound25 is less elastic than EcoFlex and is suitable for creating surfaces that will not deform) was used to fill all the triangular openings. After all the triangular openings had been filled, EcoFlex was used to cover the surface and bond it to the Rebound25 to form a single sheet.

Although the sheet was successfully produced, its softness made it difficult to maintain the desired crease and orientation when folding it into an origami actuator, unlike paper. As a result, forming the sheet into the desired shape proved challenging. One potential solution is to use a core rod, such as a Kresling-pattern rod printed with a 3D printer, to assist in the folding process. However, this approach presents significant challenges, particularly in removing the actuator from the rod. Additionally, after removal, the mountain and valley structure inherent to the Kresling pattern may not be preserved due to the material's softness.

4.1.2 Paper Folding

The above experiment shows that it is extremely challenging to use EcoFlex to directly create origami actuators. Therefore, try using ordinary paper to create origami actuators.

Initially, an attempt was made to create an origami actuator using the Kresling pattern designed by Matthew [59]. The folded origami actuator is shown in Figure 4.5.

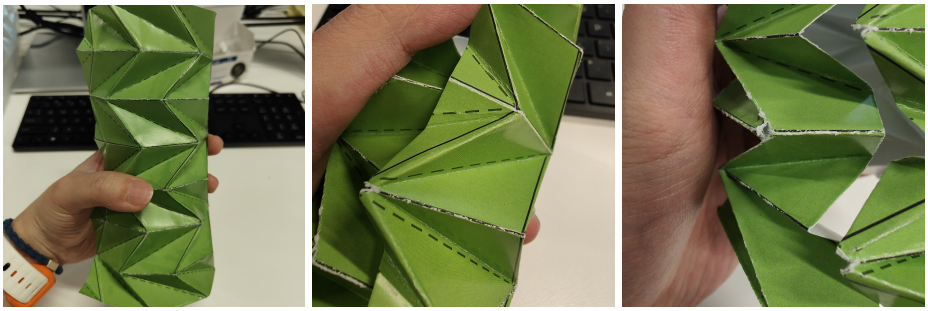

Figure 4.5: Paper Folding

However, when using only paper folds, tears tend to occur at the sharper edges. The use of additional materials in combination with paper is therefore required to enhance the strength of the origami folds.

Paper Enhancement and Sealing

EcoFlex offers good sealing properties and elasticity. When applied to folded paper, it can effectively cover the sharp edges that are prone to tearing. However, this approach introduced new challenges. While paper can be bonded using materials such as tape or glue, EcoFlex has minimal adhesion to other materials and can only bond effectively with itself. Therefore, sealing the seams of the origami actuator covered in EcoFlex becomes problematic. To maintain the shape of the Kresling pattern, a core rod that matches the pattern's design is required. However, removing the product from the core rod also presents significant challenges.

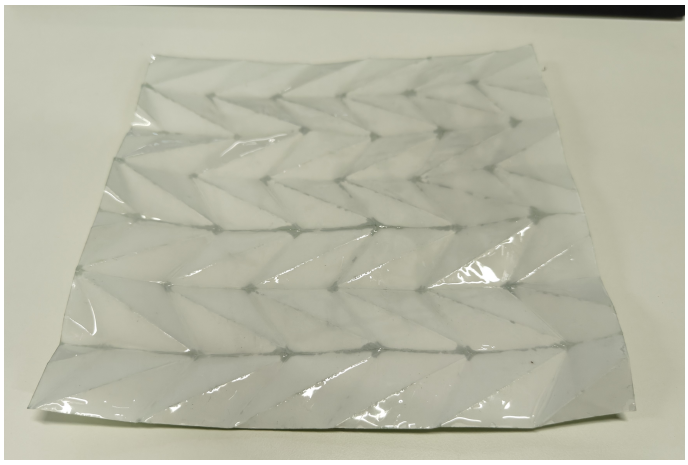

Figure 4.6: Paper Cover with EcoFlex

King [17] first folds the origami and seals the seams, then applies EcoFlex onto the origami actuator. Hongquan [71], on the other hand, first seals the origami and then immerses the actuator into a container of EcoFlex. The former sealing method does not ensure even coverage, and the resulting product experiences

air leakage after repeated bending. The latter method, however, wastes a significant amount of EcoFlex. Therefore, neither approach is ideal. Another material that sparked interest is contact paper, commonly used for book protection. It has some elasticity, with one side coated with adhesive, and its primary material is vinyl. This material provides an effective seal for the origami actuator. After completion, as shown in Figure 4.7.

Figure 4.7: Paper Cover with Contact Paper

The completed origami actuator demonstrates excellent airtightness and maintains the unique structure of the Kresling pattern during compression and extension. Therefore, using an adhesive to wrap and seal the outer surface of the paper folding is a viable approach. However, there are various types of paper and sealing agents available, and selecting the appropriate combination will be discussed in detail in Section 4.2.

4.1.3 Origami Actuator Binding

To achieve the bending motion of the ORSA, at least three origami actuators are required, and these actuators must be fixed on the same plane. Therefore, after completing the fabrication of the origami actuators, they need to be mounted on a surface, raising the new challenge of how to secure the actuators.

When securing the origami actuators, an initial attempt was made to directly bond the actuators to an acrylic sheet using EcoFlex. Due to the viscosity of EcoFlex, a brush was used to apply it at the seam between the actuator and the acrylic glass. After bonding, the result is shown in Figure 4.8. Initially, the bond between the actuator and the acrylic glass was strong. However, as gas was injected, separation occurred between the actuator and the acrylic glass. Although EcoFlex did not fracture, it formed a balloon-like structure, with gas entering the space between the actuator and the acrylic glass.

Figure 4.8: Binding with Acrylic Glass

Directly attaching the origami actuator to the acrylic glass proved infeasible. Therefore, an alternative approach was attempted by dividing the acrylic glass into three components. The first component is a hexagonal core placed at the center of the actuator's base. The second component is an outer hexagonal ring of acrylic glass, surrounding the actuator. This arrangement forms a sandwich-like structure comprising acrylic glass, paper, and acrylic glass layers. For sealing, Reboud25 was applied at the bottom (used solely for sealing purposes, as elasticity is not required for this material). Finally, another acrylic glass sheet was placed as the bottom layer, and the upper and lower acrylic glass layers were fastened together using screws and nuts. The gaps between the origami structure and the acrylic glass were filled using acrylic glue. Result displayed in Figure 4.9.

Figure 4.9: Binding with Acrylic Glass Ring

This sealing method effectively ensured the airtightness of the origami actuator, with no damage observed during the experiments. However, the large size of the acrylic glass ring added weight, which impacted the actuator's movement. In subsequent improvements, the origami structure was scaled up, and the acrylic glass components were reduced to match the diameter of the origami actuator. Additionally, thinner acrylic glass was used for fabrication to minimize weight. The final fabrication method of the origami actuator is shown in Figure 3.17.

4.2 Material Selection

When comparing different fabrication methods, various material choices were discussed. Below are some criteria for material selection:

a) The accuracy of the Kresling pattern printed with a printer is inevitably better than that drawn by hand, so the material must be printable.

b) Once the Kresling pattern has been printed, the blank area needs to be cut out, so the material must be able to be cut with a pair of scissors or a paper cutter.

c) The material must be soft enough to fold by hand but hard enough to maintain the geometry of the Kresling pattern.

Based on the above requirements, the following origami materials were selected and purchased from a local art supply store: 100mic drafting film, 110/115 tracing paper, INKJET printable plastic sheet, and 120gsm printing paper.

The first experiment is to see if the purchased paper could be folded into the Kresling Pattern. Use a printer to print the Kresling pattern shown in Figure 3.13 on different materials listed above, cut out the blank area and follow the steps in Section 3.5 to fold it. The results are shown in Figure 4.10.

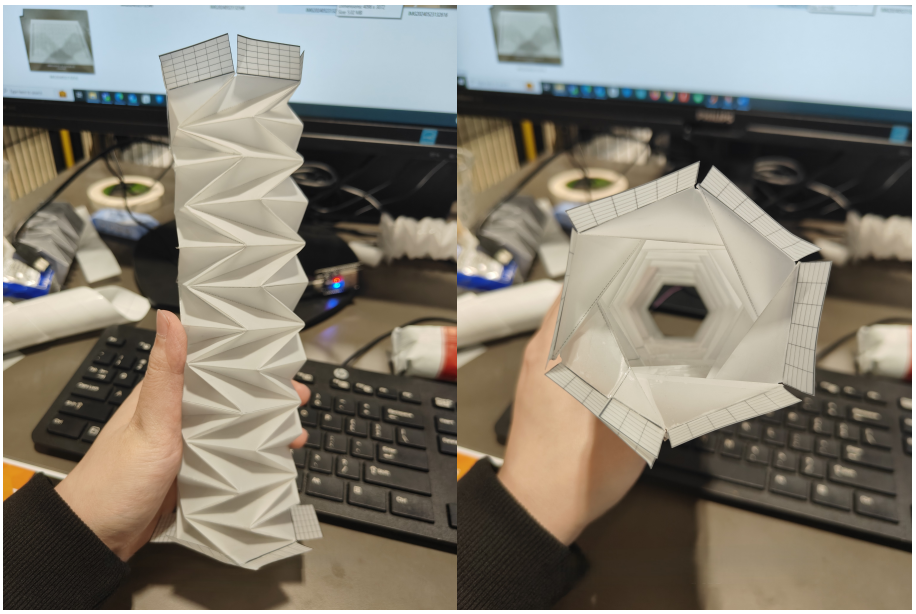

(a) 100mic Drafting Film (b) 100mic Drafting Film

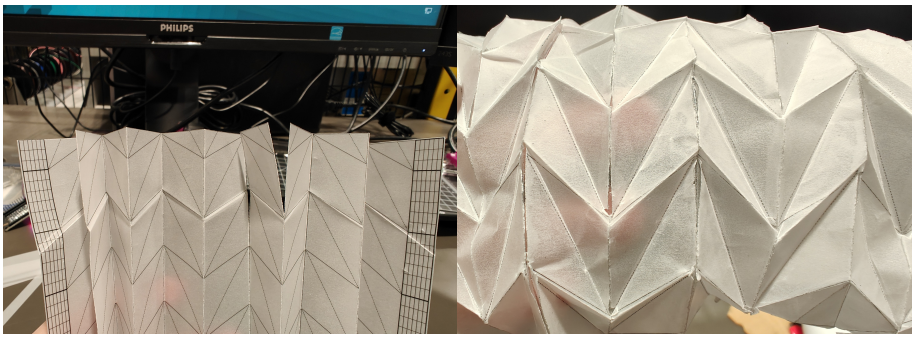

(c) 110/115 Tracing Paper (d) 110/115 Tracing Paper

(e) INKJET Printable Sheet (f) INKJET Printable Sheet

Figure 4.10: Origami with Different Materials

100-micron drafting film is a polyester film with moderate water resistance. After folding, the material fully retains the geometric structure of the Kresling pattern, including a distinct internal hexagonal structure. In contrast, 110/115gsm tracing paper, which has a frosted glass-like texture and a certain degree of stiff-

ness, develops noticeable cracks during the folding process. This indicates that such paper is brittle and unsuitable for repeated folding. INKJET-printable plastic sheets, made of PET material, exhibit good water resistance but are excessively stiff, preventing the formation of a complete Kresling pattern during folding. Finally, 120gsm paper, being thicker than standard 80gsm printing paper, provides better structural integrity and is more capable of maintaining the geometric features of the Kresling pattern.

After comparing the materials, 100 mic drafting film was the best choice. It can print patterns on its surface, is easy to fold, and can well maintain the combined structure of the Kreling Pattern. And compared to 120gsm paper, it has good air tightness. Therefore, 100 mic drafting film is the best choice.

Once the folding is complete, seams of origami need to be glued, so a suitable adhesive is required. It needs to provide sufficient air tightness to ensure the origami actuator functions properly. To choose the right adhesive, all kinds of adhesives were purchased from the same art supply store. Adhesive materials include acrylic glue, silicon rubber, sellotape, parcel tape, dot liner, contact paper. Cut the 100mic drafting film trimmed in the previous experiment into 3 cm x 5.4 cm strips. Divide the strips into groups of two, make a total of six groups. Use a different adhesive for each group to compare results.

As result shows in Figure 4.11, the acrylic glue can't glue two pieces of drafting film together. It takes 7 days for the silicone rubber to fully cure and bond the 100mic drafting film together. This is an excessively long time, which causes uncertainty in the production process. If the origami seam has a slight displacement within 7 days, it will cause bubbles in the silicone bonded part, which will affect the overall air tightness. Sellotape is a viable option, and it can adhere to 100 mic drafting film. Although parcel tape adheres well to 100 mic drafting film, it also increases the stiffness of the film by its thickness, and if not cut into shape properly, may have a bad effect on soft robot movement. The dot liner is too weak to bond 100mic drafting film together. Although the results of contact paper are not as good as those of Sellotape, a gap can be clearly observed between the two strips when the top strip is lifted. However, compared to other adhesives, contact paper can still be regarded as a usable adhesive that is inferior to Sellotape. This material selection experiment was conducted to identify suitable paper for the origami folding and an adhesive that can bond the origami seams. After comparing all the results, 100 mic drafting paper and 120gsm paper were found to be the most suitable materials for origami folding. Sellotape and contact paper were found to be suitable adhesives for bonding the origami seams. Subsequent experiments will identify the best combination of these four materials.

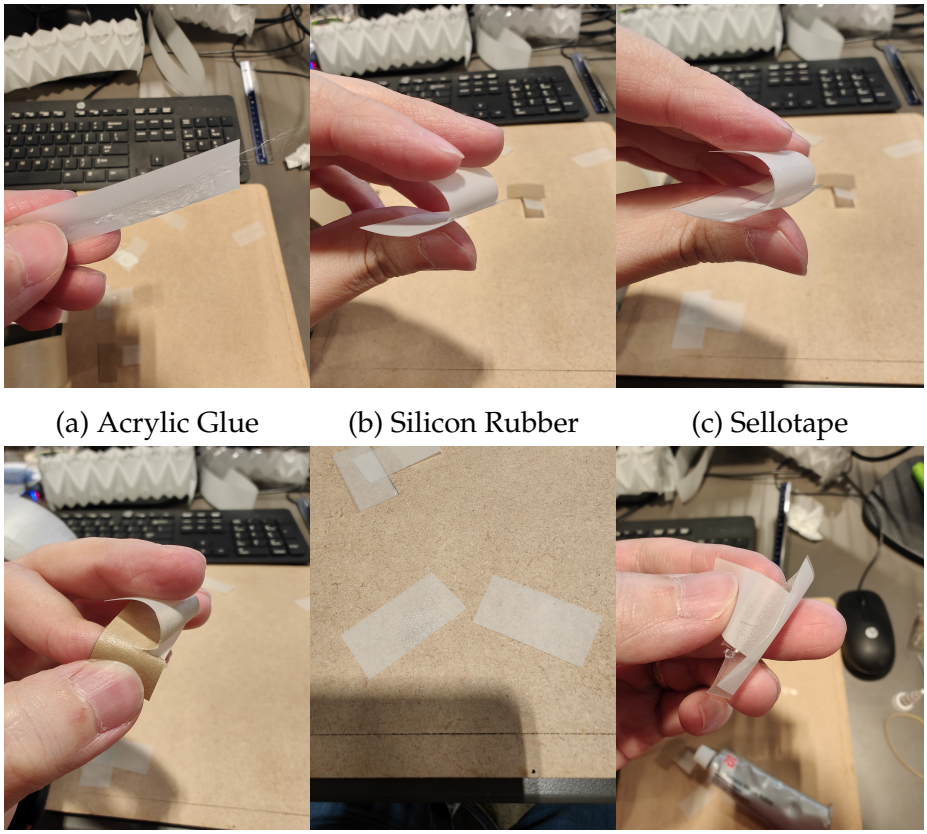

(a) Acrylic Glue (b) Silicon Rubber (c) Sellotape

(d) Parcel-tape (e) Dot-liner (f) Contact Paper

Figure 4.11: 100mic Drafting Film with Different Adhesives

4.3 Mechanical Experiment

The experiment in Section 4.2 showed that 100 mic drafting film and 120 gsm paper are the most suitable materials for origami, and Sellotape and contact paper can be used as adhesives for gluing and folding paper joints. This experiment will compare the adhesion strength of these four materials in pairs to select the best combination. The tensile testing machine used in the test is usually used to measure the tensile strength of materials that can withstand stronger tensile forces, such as metal materials such as iron or composite materials such as nylon fibres. In order to verify whether the tensile testing machine can obtain results when the tested material is paper, ordinary printing paper (80gsm paper) was first tested alone. To avoid the sheet being too thin to obtain a reading, the 80gsm paper was folded four times in a zigzag pattern, so that it went from one layer to five. The results of the experiment are shown in Figure 4.12, the 80gsm paper can withstand a tensile force of $100.333\,\mathrm{N}$.

Therefore, 80gsm paper was also added to the experimental group. Material combinations for this experiment are as follows:

To ensure the validity of the experimental results and control the variables, the paper strips used in this experiment were all cut to the same size and shape,

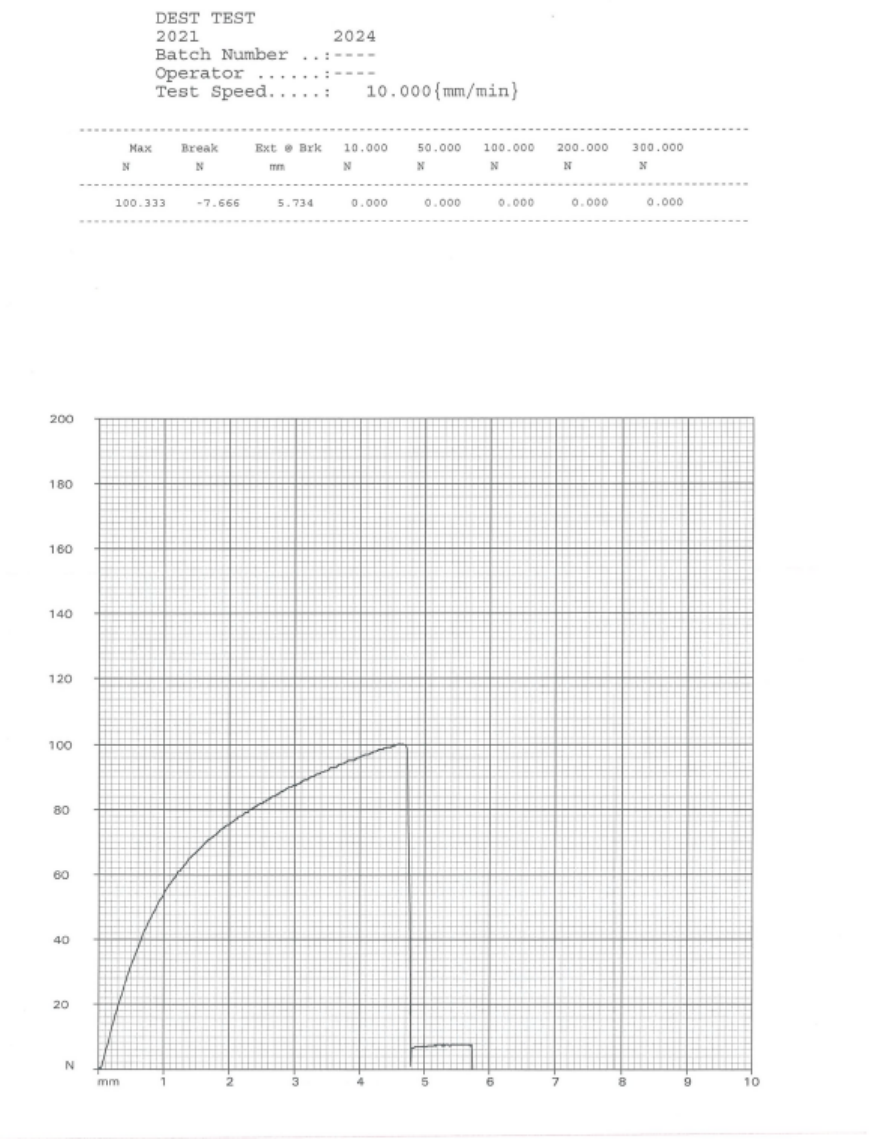

Figure 4.12: 80gsm Paper Tensile Experiment

Material Combinations List		
Number	Paper	Adhesive
1	80gsm paper	Contact paper
2	80gsm paper	Sellotape
3	100mic drafting film	Contact paper
4	100mic drafting film	Sellotape
5	120gsm paper	Contact paper
6	120gsm paper	Sellotape

Table 4.1: List of material combinations for testing.

and the adhesive area was kept the same size and shape. The only variable was the combination of different papers and adhesives. The paper used in the experi-

ment was cut into two equal strips, placed on the left and right respectively, with an overlap in the middle, and different adhesives were applied to the overlap. At the same time, to ensure that the tensile testing machine could obtain valid data, the paper strip was also folded four times in a zigzag pattern, increasing from one layer to five layers. Figure 4.13 shows the size and shape of the single layer of the paper strip being tested. Figure 4.14shows the results of the experiment for these

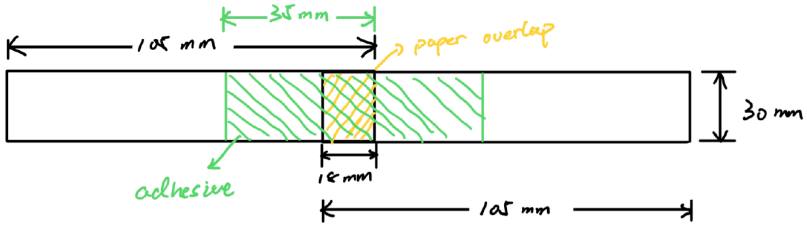

Figure 4.13: Paper Strips Specification

six material combinations. The results were generated using a tensile testing machine. The results for each group consist of two parts: the upper reading and the lower graph. The upper reading consists of three readings, which represent the maximum tensile force(N), the material breaking stress(N), and the distance stretched at the time of breaking(mm). This experiment only focuses on the maximum tensile force that different material combinations can withstand, so only the first reading is of interest. The graph below represents the tensile force applied to the material as the distance increases during the tensile test. The highest point of the curve is the same as the maximum tensile force in the reading above. This graph only shows the change in tensile force applied to the material. Therefore, only the first reading in the graph of the test results needs to be considered.

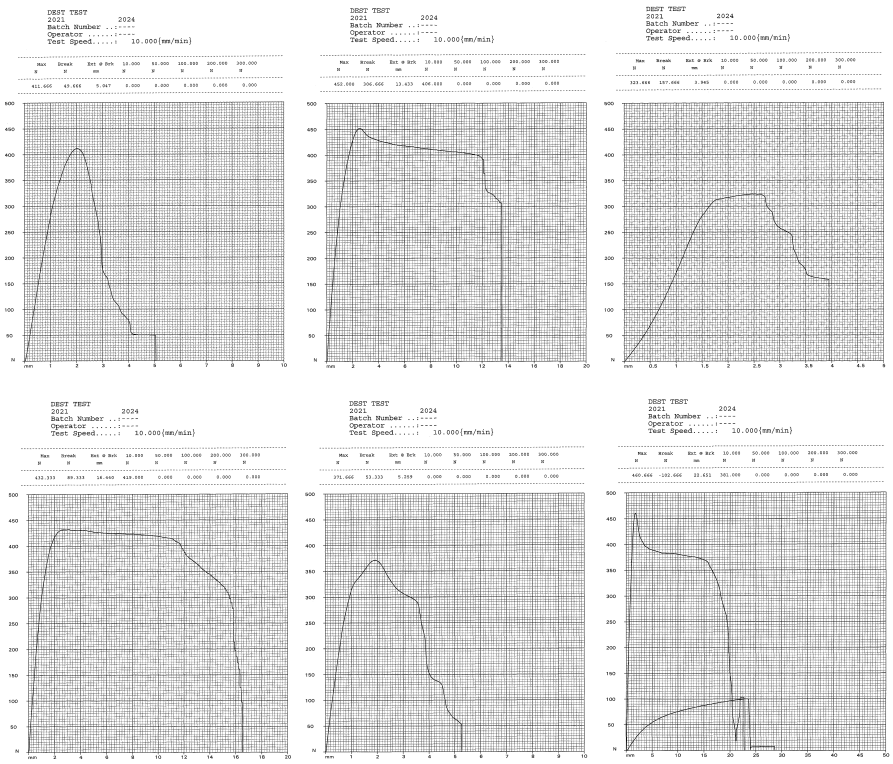

Figure 4.14: Tensile Experiments Results

By comparing the results of the six experiments in Figure 4.14, it can be concluded that the material combination of 120gsm paper and Sellotape can withstand the maximum tensile force, which is $460.666\,\mathrm{N}$. Therefore, these two materials will be selected for the fabrication of the origami actuators.

4.4 Soft Arm

After selecting the materials, three origami actuators were made using the selected materials according to the steps in Section 3.5, and a simple assembly was performed using zip-ties and masking tape to form a soft robotic arm, as shown in Figure 3.17.

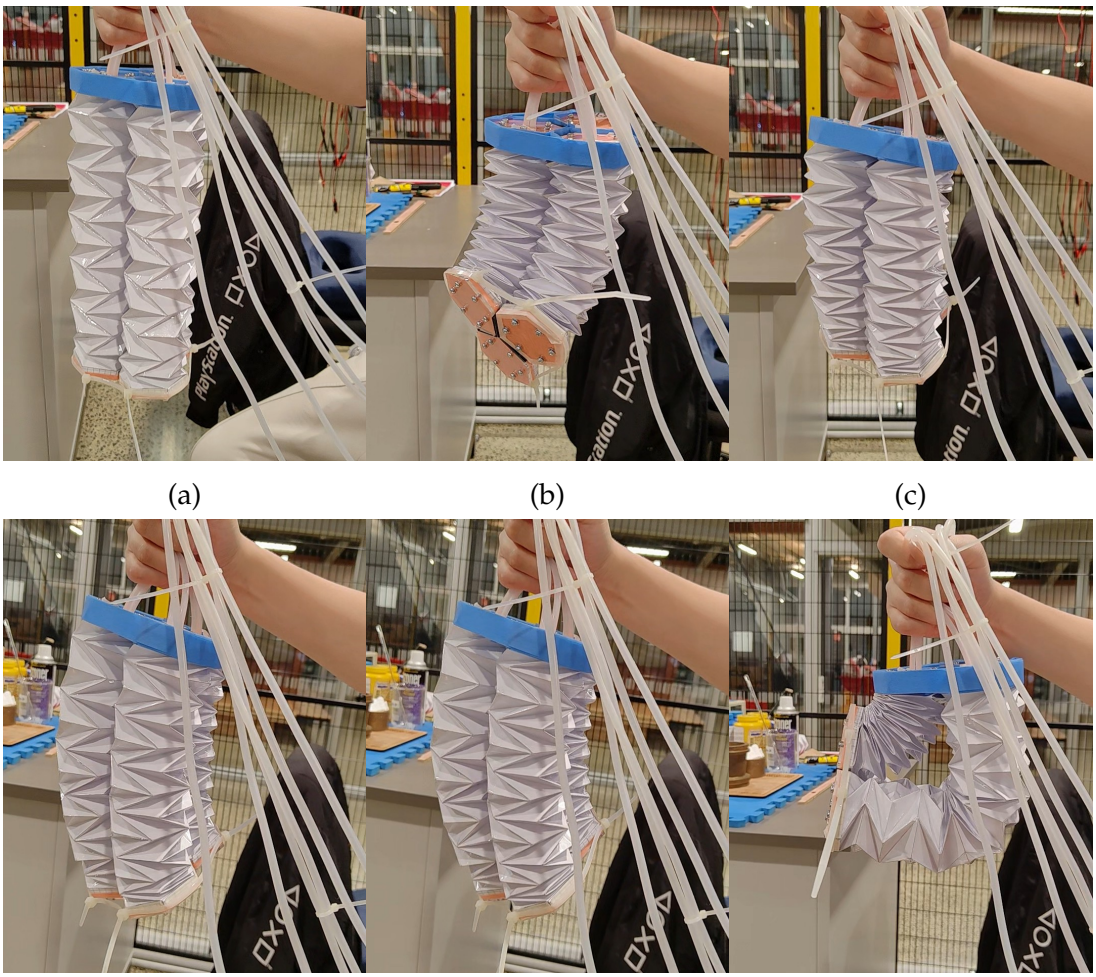

(a) (b) (c)

(d) (e) (f)

Figure 4.15: Temporary Assembled Soft Robotic Arm

The previous steps should be repeated three times to create three origami cylinders. The three completed actuators are shown in Figure 4.16. Once connected to the pneumatic drive system, the simply assembled soft robotic arm can cause the single or multiple origami actuators to compress or extend according to the design of control system in Section 3.2, and thus cause the soft robotic arm to bend, compress and extend by pressing different buttons. Figure 4.15 shows the different postures of the proposed assembled soft robotic arm.

For a single origami cylinder without sealing pads or connection pads, the natural length was measured as 18.0 cm, and it could be compressed to a minimum of 2.29 cm or extended to a maximum of 36.0 cm. A single origami actuator was able to bend up to 180°, while the assembled soft robotic arm consisting of three actuators achieved a maximum bending angle of 105°. During testing, the internal pressure measured in all origami actuators ranged from 56.97 kPa to 103.74 kPa, with a sensor accuracy of 0.25% FSS (BFSL), where FSS refers to the full scale span between the maximum and minimum calibrated pressure limits [106]. In terms of actuation dynamics, a single origami actuator required approximately

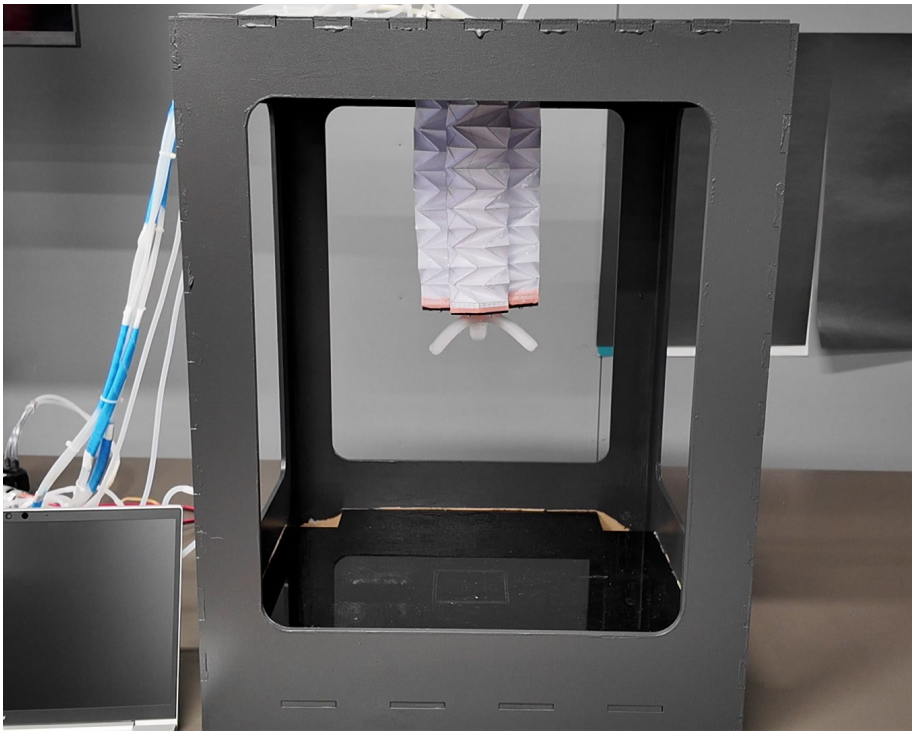

Figure 4.16: Assembled Soft Robotic Arm

4 seconds to complete the transition from the fully extended to the fully compressed state, whereas the assembled OSRA required 8 seconds to achieve full compression along the vertical axis. These results demonstrate that the OSRA is capable of substantial axial deformation and bending while maintaining structural integrity under stable pneumatic conditions.

Use the connecting pads in Section 3.1 to reassemble the soft robotic arm into a single unit, and then fix the soft robotic arm to the inside of the frame in Section 3.1 as shown in Figure 4.16.

After all the components have been assembled, the manipulator actuation system can be used to control the soft robotic arm to perform the desired actions. The stereo camera can detect the spatial position of the soft robotic arm and display its 3D shape in a point cloud, as discussed in Section 4.5.

Two issues were noted during the testing of the robotic arm. These issues do not affect the movement of the soft robotic arm, the response of the control system, or the accuracy of the stereo vision system for each soft robotic arm, but still need to be improved in future research. Therefore, the problems will be described and analyzed in this section.

The first problem is: After the gripper is made, the responses of its different branches are different. Section 3.1 mentioned that the grapple's design was based on an online open-source file. The original grapple design was relatively small, with only 6.5 cm from the center to the tips of each fork. To create the gripper, the overall size was scaled up by a factor of two. After fabrication, air was man-

ually injected into the gripper using a syringe. However, only one branch bent as intended, while the other two exhibited minimal response.

To investigate this issue, purple-coloured water was injected into the gripper using a syringe, as shown in Figure 4.17. The observations revealed two main problems. In one branch, the upper and lower layers were not tightly bonded, allowing the purple water to spread out beyond the grid-like air chamber. In another branch, the purple water did not fully occupy the air chamber, with some sections having more water than others. This inconsistency was caused by an excessive amount of silicone applied during bonding, which flowed into the air cavities and solidified, partially blocking the air chamber.

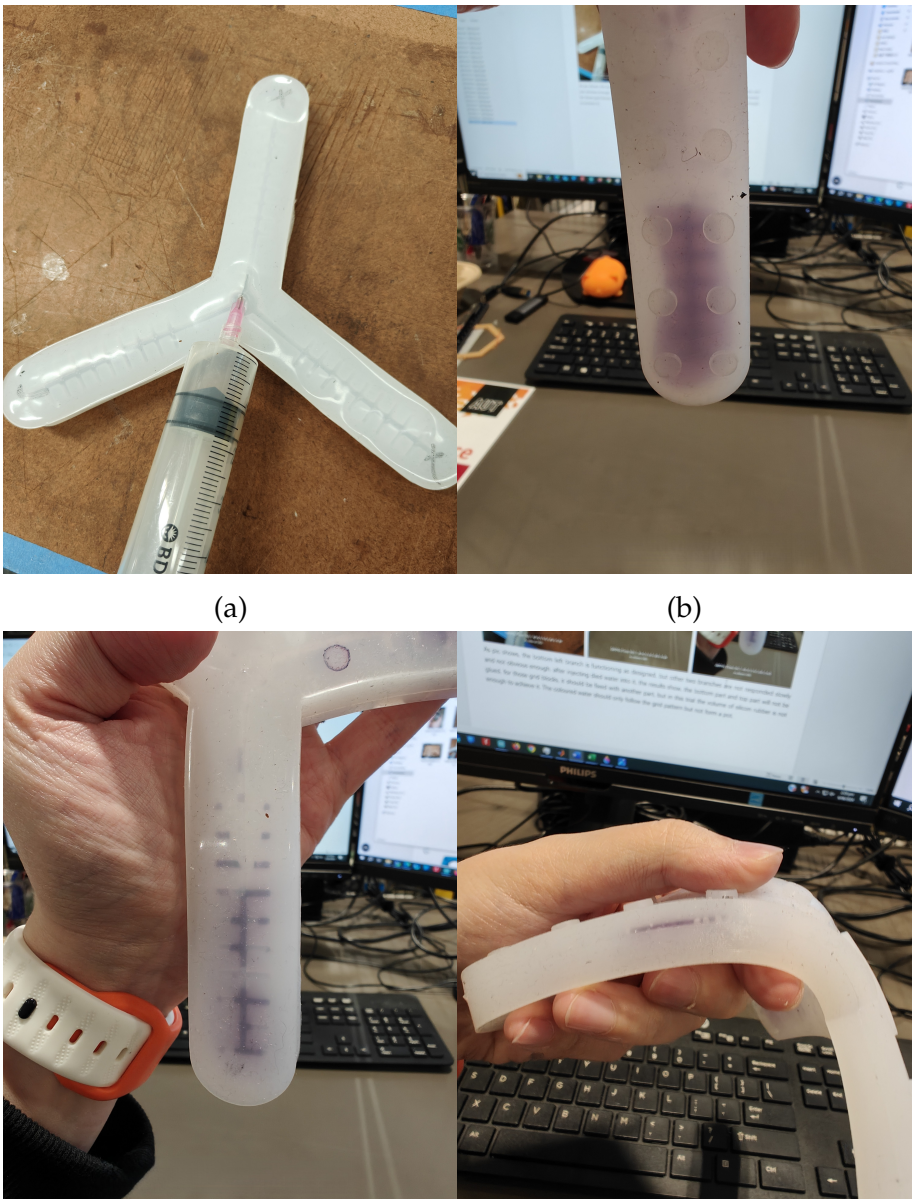

(a) (b)

(c) (d)

Figure 4.17: Soft Gripper Test

The problems with these two branches highlight the challenge of using EcoFlex to bond two pre-cured EcoFlex parts. To achieve an even adhesive layer, other tools must be employed to ensure the correct amount of EcoFlex is applied, preventing blockage of the air chamber. Further experimentation and research are needed to address this issue.

The second problem encountered was overheating of the air pump. To identify the cause, a thermal imager was used to locate hot spots. As shown in Figure 4.18, the thermal imager revealed that the hot spot was near the air outlet of the pump. Further disassembly of the pump (Figure 4.19) showed that it uses a simple piston structure. The cylinder lacks an effective lubrication system, causing the rubber seal and plastic cylinder to rub against each other as the piston moves back and forth, generating heat.

To resolve the overheating issue, the air pump was disassembled, and lubricant was applied to the piston seal, which reduced the temperature by 3.3815°C, as shown in Figure 4.20a.

A long-term test (Figure 4.20b) was conducted to evaluate the effectiveness of the lubricant. After extended use, the temperature continued to rise, and it was noted that the lubricant's shelf life is approximately one month. To mitigate overheating, the air pump is now operated in intervals: it runs for 5 minutes and is then turned off to cool down.

Currently, there is no more effective method to cool the air pump, but this is not a critical issue for the Soft Robotic Arm. In the future, air pumps with better internal lubrication designs can be considered.

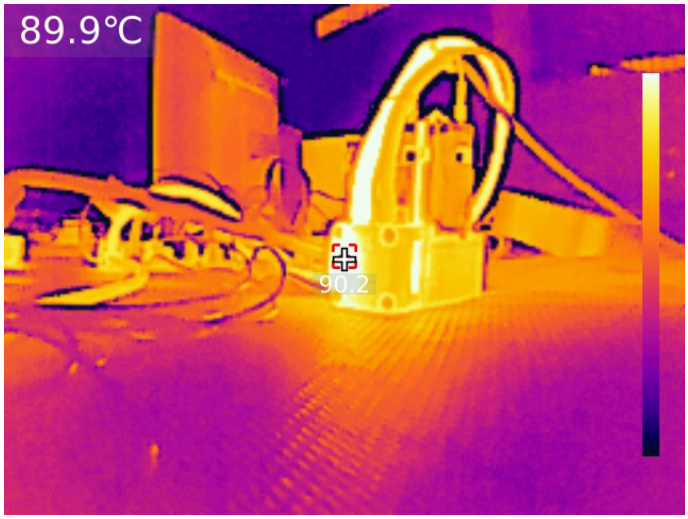

Figure 4.18: Air Pump Temperature Measurement

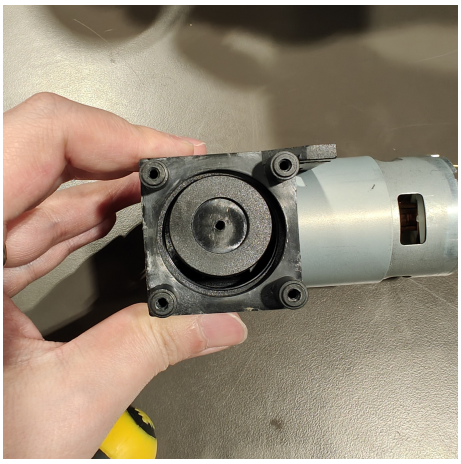

Figure 4.19: Disassembled Air Pump

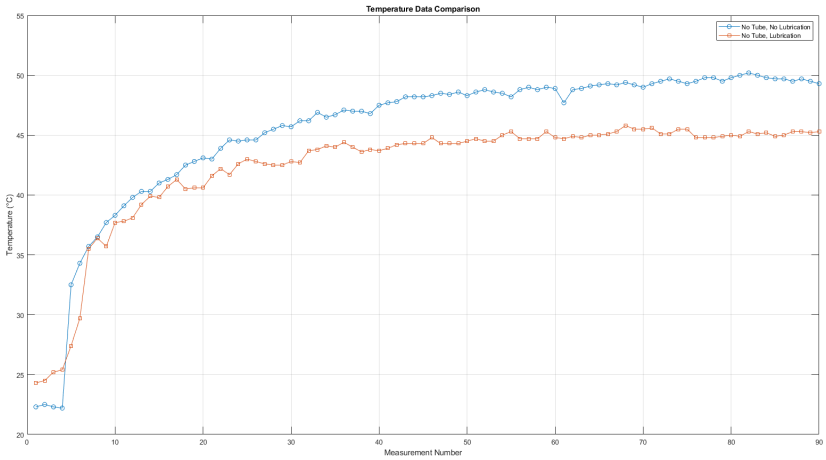

(a) Air Pump Temperature Compression between without lubrication and with lubrication

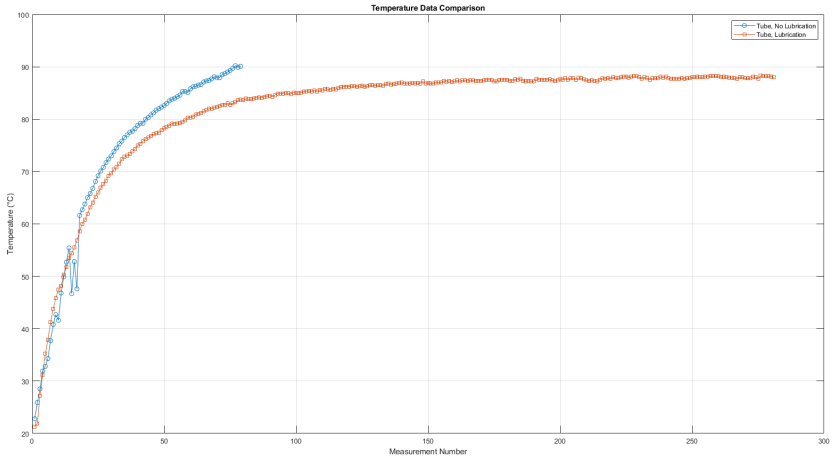

(b) Air Pump Temperature with lubrication

Figure 4.20: Air Pump Temperature Analysis

4.5 Control System

4.5.1 Pneumatic System

The current control system is based on the block diagram of the control system in figure 3.9 and the electrical system block diagram in figure 3.6. As a result, the system operates as intended: when the user presses a button, the corresponding origami actuator compresses or extends, causing the soft robotic arm to move. The pneumatic pressure sensor continuously measures the internal air pressure of the origami actuators, while the vision system monitors the length and spa-

tial position of the entire soft robotic arm. These two measurements are fed back to the pneumatic drive system, which halts the current action and interrupts the user's input before the origami actuator reaches its compression or extension limits, thereby protecting the soft robotic arm.

The schematic illustrates a pneumatic drive system with an ESP32 microcontroller at its core, controlling all components. During testing of the components and circuits, a limitation of the ESP32's I2C interface was identified. Specifically, all three air pressure sensors use the I2C communication protocol and share the same I2C address. This prevents all three sensors from connecting to the same I2C bus simultaneously, as the ESP32 only has two I2C buses. To resolve this issue, a TCA9458A I2C multiplexer was added to the circuit. This allows a single I2C bus to connect up to 8 components with the same I2C address, improving the scalability of the pneumatic drive system. The completed drive system is shown in Figure 4.21.

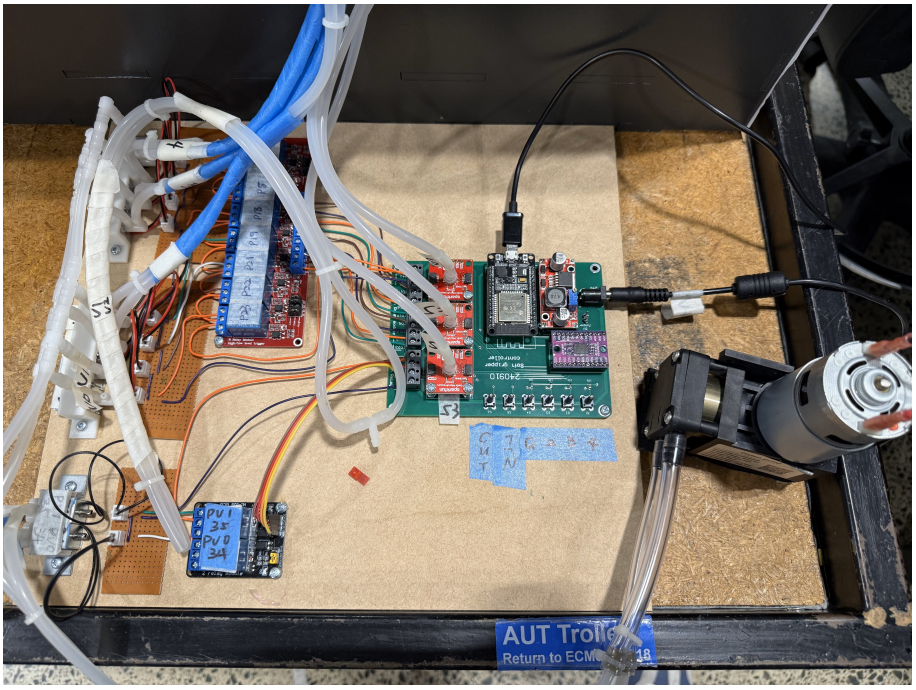

Figure 4.21: Pneumatic-Drive System

Since the stereo vision system operates on the computer, the overall control system also includes the computer end. Upon startup, the ESP32 connects to a WiFi network to obtain time information from an NTP server. Once this step is completed, data from each port—including the status of buttons and valves, and the readings from the air pressure sensors—are continuously sent to MATLAB. After receiving this data, MATLAB displays it in the command window in a formatted style and generates a comma-separated values (CSV) file locally to store the information received at each instance. Figure 4.22 shows an example of the recorded data.

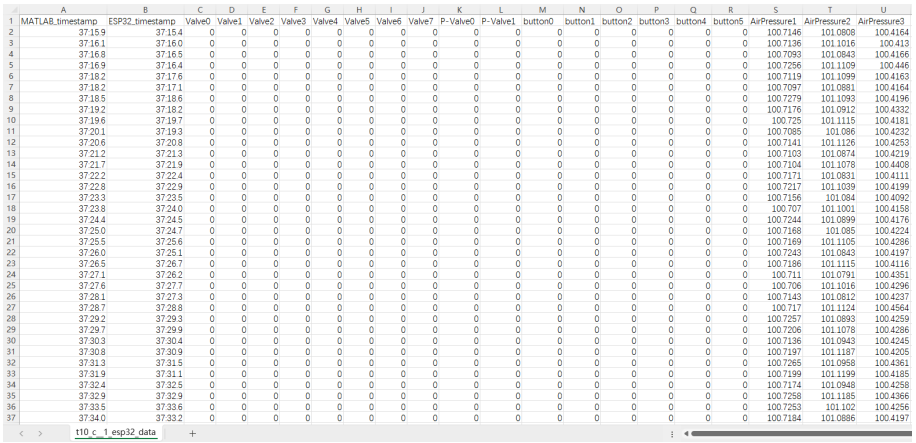

	A	B	C	D	E	F	G	H	I	J	K	L	M	N	O	P	Q	R	S	T	U
1	MATLAB_timestamp	ESP32_timestamp	Valve0	Valve1	Valve2	Valve3	Valve4	Valve5	Valve6	Valve7	P-Valve0	P-Valve1	button0	button1	button2	button3	button4	button5	AirPressure1	AirPressure2	AirPressure3
2	37:15.9	37:15.4	0	0	0	0	0	0	0	0	0	0	0	0	0	0	0	0	100.7146	101.0808	100.4164
3	37:16.1	37:16.0	0	0	0	0	0	0	0	0	0	0	0	0	0	0	0	0	100.7136	101.1016	100.413
4	37:16.8	37:16.5	0	0	0	0	0	0	0	0	0	0	0	0	0	0	0	0	100.7093	101.0843	100.4166
5	37:16.9	37:16.4	0	0	0	0	0	0	0	0	0	0	0	0	0	0	0	0	100.7256	101.1109	100.446
6	37:18.2	37:17.6	0	0	0	0	0	0	0	0	0	0	0	0	0	0	0	0	100.7119	101.1099	100.4163
7	37:18.2	37:17.1	0	0	0	0	0	0	0	0	0	0	0	0	0	0	0	0	100.7097	101.0881	100.4164
8	37:18.5	37:18.6	0	0	0	0	0	0	0	0	0	0	0	0	0	0	0	0	100.7279	101.1093	100.4196
9	37:19.2	37:18.2	0	0	0	0	0	0	0	0	0	0	0	0	0	0	0	0	100.7176	101.0912	100.4332
10	37:19.6	37:19.7	0	0	0	0	0	0	0	0	0	0	0	0	0	0	0	0	100.725	101.1115	100.4181
11	37:20.1	37:19.3	0	0	0	0	0	0	0	0	0	0	0	0	0	0	0	0	100.7085	101.086	100.4232
12	37:20.6	37:20.8	0	0	0	0	0	0	0	0	0	0	0	0	0	0	0	0	100.7141	101.1126	100.4253
13	37:21.2	37:21.3	0	0	0	0	0	0	0	0	0	0	0	0	0	0	0	0	100.7103	101.0874	100.4219
14	37:21.7	37:21.9	0	0	0	0	0	0	0	0	0	0	0	0	0	0	0	0	100.7104	101.1078	100.4408
15	37:22.2	37:22.4	0	0	0	0	0	0	0	0	0	0	0	0	0	0	0	0	100.7171	101.0831	100.4111
16	37:22.8	37:22.9	0	0	0	0	0	0	0	0	0	0	0	0	0	0	0	0	100.7217	101.1039	100.4199
17	37:23.3	37:23.5	0	0	0	0	0	0	0	0	0	0	0	0	0	0	0	0	100.7156	101.084	100.4092
18	37:23.8	37:24.0	0	0	0	0	0	0	0	0	0	0	0	0	0	0	0	0	100.707	101.1001	100.4158
19	37:24.4	37:24.5	0	0	0	0	0	0	0	0	0	0	0	0	0	0	0	0	100.7244	101.0899	100.4176
20	37:25.0	37:24.7	0	0	0	0	0	0	0	0	0	0	0	0	0	0	0	0	100.7168	101.085	100.4224
21	37:25.5	37:25.6	0	0	0	0	0	0	0	0	0	0	0	0	0	0	0	0	100.7169	101.1105	100.4286
22	37:26.0	37:25.1	0	0	0	0	0	0	0	0	0	0	0	0	0	0	0	0	100.7243	101.0843	100.4197
23	37:26.5	37:26.7	0	0	0	0	0	0	0	0	0	0	0	0	0	0	0	0	100.7186	101.1115	100.4116
24	37:27.1	37:26.2	0	0	0	0	0	0	0	0	0	0	0	0	0	0	0	0	100.711	101.0791	100.4351
25	37:27.6	37:27.7	0	0	0	0	0	0	0	0	0	0	0	0	0	0	0	0	100.706	101.1016	100.4296
26	37:28.1	37:27.3	0	0	0	0	0	0	0	0	0	0	0	0	0	0	0	0	100.7143	101.0812	100.4237
27	37:28.7	37:28.8	0	0	0	0	0	0	0	0	0	0	0	0	0	0	0	0	100.717	101.1124	100.4564
28	37:29.2	37:29.3	0	0	0	0	0	0	0	0	0	0	0	0	0	0	0	0	100.7257	101.0893	100.4259
29	37:29.7	37:29.9	0	0	0	0	0	0	0	0	0	0	0	0	0	0	0	0	100.7206	101.1078	100.4286
30	37:30.3	37:30.4	0	0	0	0	0	0	0	0	0	0	0	0	0	0	0	0	100.7136	101.0943	100.4245
31	37:30.8	37:30.9	0	0	0	0	0	0	0	0	0	0	0	0	0	0	0	0	100.7197	101.1187	100.4205
32	37:31.3	37:31.5	0	0	0	0	0	0	0	0	0	0	0	0	0	0	0	0	100.7265	101.0958	100.4361
33	37:31.9	37:31.1	0	0	0	0	0	0	0	0	0	0	0	0	0	0	0	0	100.7199	101.1199	100.4185
34	37:32.4	37:32.5	0	0	0	0	0	0	0	0	0	0	0	0	0	0	0	0	100.7174	101.0948	100.4258
35	37:32.9	37:32.9	0	0	0	0	0	0	0	0	0	0	0	0	0	0	0	0	100.7258	101.1185	100.4366
36	37:33.5	37:33.6	0	0	0	0	0	0	0	0	0	0	0	0	0	0	0	0	100.7253	101.102	100.4256
37	37:34.0	37:33.2	0	0	0	0	0	0	0	0	0	0	0	0	0	0	0	0	100.7184	101.0886	100.4197

t10_c_1_esp32_data

Figure 4.22: Local CSV Data Record

As shown in Figure 4.22, each record includes two timestamps. The first timestamp indicates the time when MATLAB received the information, while the second represents the time when ESP32 sent the information. A slight difference between these two timestamps is observed, and this issue will be addressed later. To the right of the timestamps are the statuses of the eight two-way valves and two three-way valves, where a value of 1 indicates the valve is open and 0 indicates the valve is closed. The statuses of the six buttons are displayed in the same way. The last three columns display the real-time readings from the air pressure sensors. Using MATLAB to display and save data in real-time makes it easier to identify and compare data, particularly when the system encounters an error.

While obtaining data from the ESP32, MATLAB also operates the stereo vision system. It uses the stereo camera to calculate the disparity map and point cloud map to identify the spatial position of OSRA, including its length and depth, which are then displayed on the user dashboard. After calculating OSRA's length and depth, MATLAB compares these values with predefined thresholds. If the values exceed the threshold, it indicates that OSRA may be overextending or compressing. MATLAB will then send a signal back to the ESP32 via the serial port, instructing it to stop the current action and halt any further response to the user's operation.

There are some minor issues with the control system. These issues do not affect its current functionality but do suggest areas for improvement.

Firstly, the ESP32 in the pneumatic drive system communicates with MATLAB via a serial port, requiring an additional cable to connect the ESP32 to the computer. While the ESP32 is connected to the computer, it is powered by a USB cable. If another power supply is connected simultaneously, it could potentially damage the circuit components (since the input voltage for the air pressure sensors must not exceed 3.6V) or even the ESP32 itself. Although there is a jumper connector in the board design to select the power supply, there is still a possibility of incorrect operation.

Secondly, due to the limited ROM on the ESP32 (only 4MB), it cannot simultaneously store both the Bluetooth and WiFi libraries, which prevents the use of the Bluetooth module for communication.

Thirdly, when using the WiFi module, the computer must be connected to the ESP32 network, which prevents the computer from accessing the internet.

Fourthly, although the ESP32 can be programmed using the Arduino platform, which offers many libraries, it lacks native multi-threading capabilities. The current system uses FreeRTOS, with the main program allocating clock cycles to different tasks to simulate multi-threading. However, this method does not meet OSRA's need for faster response times.

Finally, when using an NTP server to obtain time information, the accuracy of all microcontrollers is limited to the second range. Therefore, synchronizing time information in milliseconds between the ESP32 and MATLAB is not feasible. Although the ESP32 can record the millisecond counter after it is powered on, this counter is not accurate enough, leading to the time segment counting accuracy issue mentioned in Section 4.5.

4.5.2 Stereo Vision System

Early attempts to recognise the robotic arm used background subtraction in the stereo vision system. Initially, basic image subtraction was applied, where the first frame of the live video served as the background, and this content was subtracted from each subsequent frame to extract the foreground object. Figure 4.23a shows the background frame, while Figure 4.23b depicts the foreground frame. The subtraction of the two frames is shown in Figure 4.23c. However, this approach did not fully capture the foreground object (e.g., the human figure), with parts of the outline, such as the shoulders and top of the head, disappearing. To improve the results, we attempted to dynamically update the background by assigning different weights to the first frame and the latest frame. Additionally, morphological operations were employed, but the results remained suboptimal, as shown in Figure 4.24.

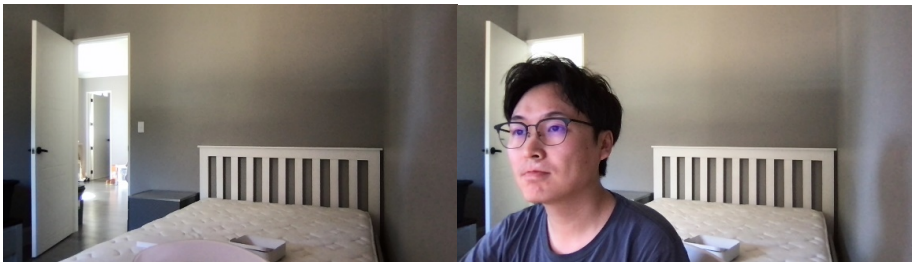

(a) Background Image (b) Foreground Image

(c) Result

Figure 4.23: Background Subtraction

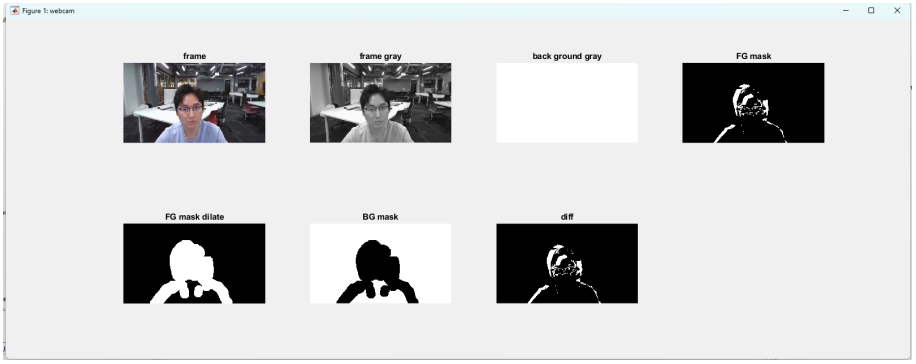

Figure 4.24: Image Subtraction with Morphological Operations

Figure 4.26 illustrates the processed point cloud map, wherein OSRA is delineated through the region of interest. Stereo camera calibration achieved a baseline of 107.43mm with an overall RMS reprojection error of 0.168px and a per-image RMS error of 0.193 ± 0.102px, confirming sub-pixel accuracy suitable for 3D reconstruction. For point cloud processing, a voxel downsampling step of 1 cm and a predefined region of interest were applied to suppress background clutter. OSRA was then extracted by selecting a central point at (0, 0, 135) cm and retrieving up to 2,500 neighboring points, constrained to a length range of 8–34.5 cm.

The raw reconstructed point cloud contained approximately 738,000 points, but due to the presence of invalid values (Inf/NaN), its bounding-box volume and density could not be reliably estimated. After ROI selection, the point cloud was reduced to 2,125 points, corresponding to a density of 0.283 points/cm³ within a bounding volume of 7,513 cm³. The same density was maintained after the nearest-neighbor step, as all ROI points were retained. Following denoising, the point count decreased slightly to 2,059, with a density of 0.282 points/cm³. These results demonstrate that the pipeline effectively reduced the data size while preserving a stable point density for representing the OSRA, thereby minimizing interference from background and surrounding objects.

In this project, this method successfully extracted OSRA from the real-time image. However, the two steps of delimiting the region and finding the neighboring points require considerable computation. This slows the control system's overall responsiveness, and delays can be observed in the real-time point cloud image. To quantify the temporal discrepancy between video duration and processing time, a reference video recorded by the same stereo camera was used. With disparityBM, the pipeline processed 900 frames in 127.3 seconds at a mean rate of 7.07 frames per second, whereas the reference video lasted 90 seconds. This corresponds to 0.71 times real-time speed, resulting in an additional latency of 37.3 seconds. On a per-frame basis, the processing time varied between 0.127 s and 0.585 s, with a mean of 0.141 s, indicating moderate fluctuations in computational load across frames, as Figure **??** shows.

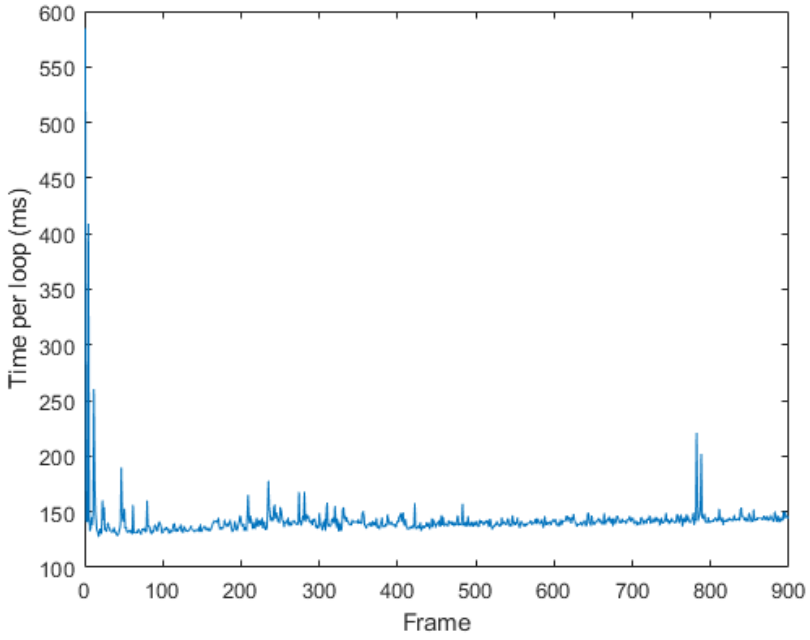

Figure 4.25: CPU Processing Time per Frame

Furthermore, it is evident that the representation of OSRA in the point cloud

image is incomplete, and the structure of the Kresling Pattern is not fully depicted. The issue of incomplete reality can be attributed to the camera's performance. Figure 4.26b illustrates the presence of noise and smearing in the image, which becomes more evident upon closer examination. In contrast, the photograph taken after positioning the phone in the exact location as the stereo camera in Figure 4.27b does not exhibit this smearing phenomenon.

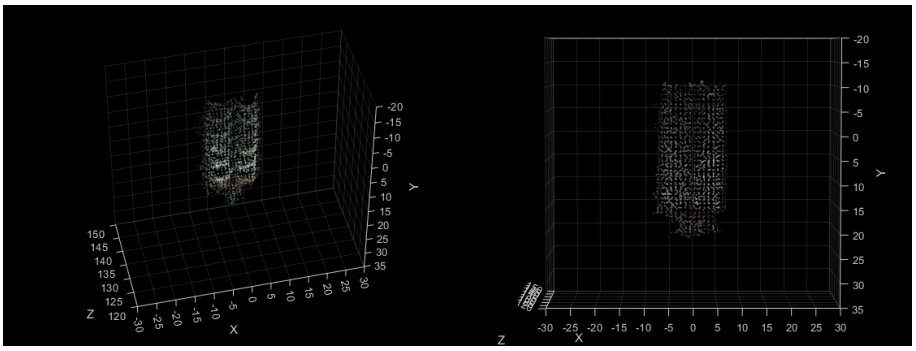

(a) (b)

Figure 4.26: Point Cloud of Soft Robotic Arm

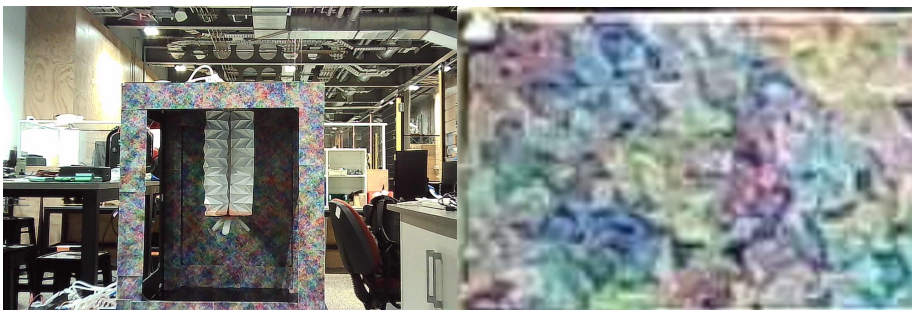

(a) Image Captured by Camera (b) Partial Magnification

(c) Image Captured by Phone (d) Partial Magnification

Figure 4.27: Comparison between Current Camera and Smart Phone Camera

Despite the flaws in the control system, it was still able to calculate the real-time position of OSRA based on the data in the point cloud map and calculate the arm length, which, combined with the real-time readings from the air pressure sensors, prevented damage to the arm structure.

Taken together, this project uses an optimal combination of common materials to fabricate the OSRA and establishes an efficient control system integrated with stereo vision and sensors for real-time management of the soft robotic arm. The primary objective of the control system is to accurately manage the arm's movements by utilizing spatial position data from the stereo vision and feedback from the pressure sensors. This ensures that the arm's motions are precisely controlled, preventing damage caused by excessive extension or compression. Furthermore, the system is designed to continuously monitor and adjust the arm's actions in real-time, ensuring its adaptability and stability in complex environments.

Chapter 5

Discussion

In this thesis, 120 gsm paper, Sellotape, EcoFlex, and Acrylic glass were used to create the OSRA. In contrast, many soft robotic systems reported in the literature are fabricated primarily from silicone or dielectric elastomers and other flexible polymers [2,3,6], highlighting that the present design leverages a hybrid approach combining paper-based origami with elastomeric and rigid materials to achieve low-cost and lightweight construction. This combination of materials and fabrication methods was experimentally compared, and the best combination was obtained from three different papers, two different adhesives, and the additional materials EcoFlex and Acrylic glass.

The control system, consisting of two main components—a pneumatic driving system and a stereo vision system—allows the user to control the movement of the OSRA and monitor its state and spatial position in real-time through a dashboard during operation. The stereo vision system and the air pressure sensor in the pneumatic driving system serve as feedback elements within the control system. The integration of feedback signals to the ESP32, which in turn manages the actuation of the pneumatic system, enables closed-loop control of the OSRA. This is an improvement over earlier soft robotic systems that typically employed open-loop control without sensor feedback [2,76].

Compared to other projects that use visual control or analysis systems [7–9, 77,83], this design does not require a significant amount of data for mathematical modelling or visual model training.

Furthermore, during the design and fabrication process, a more rapid and precise folding method for the Kresling pattern was identified. For comparison, the method proposed by Matthew [59] involves an A4-sized Kresling pattern requiring 10 min 50 seconds for cutting and folding, excluding the time for adhesive bonding and sealing. In contrast, the fabrication process developed in this project enables the completion of a Kresling pattern within 36 minutes 29 seconds for cutting and folding, plus 31 minutes 08 seconds for bonding and sealing. As a result, a complete unassembled OSRA can be produced in just 1 hour 6 minutes 37 seconds. Beyond efficiency, the proposed method also avoids the accuracy loss typically caused by the increased thickness of folded paper layers, ensuring structural precision and consistency.

During the experiment, some issues were identified, such as the discrepancy

between the ESP32 and MATLAB time stamps and the different responses of the gripper branches. However, these issues do not affect the overall functionality of the OSRA, as the control system can still effectively manage the arm to achieve the expected motion.

The objective of this project was to design a vision-based, markerless control system for an OSRA and to optimise its fabrication method. The control system successfully demonstrated its ability to subtract the OSRA from the background, extract its spatial position, and use this data to prevent structural damage caused by improper operation.

The overall result met expectations. The OSRA can bend, compress, and stretch in different directions, while the control system can effectively execute the user's operation and prevent structural damage to the arm due to excessive stretching and compression.

During the experiment, the main limitation observed was the latency introduced by the stereo vision processing, which affected the responsiveness of real-time control. Other phenomena, such as minor variations in the gripper response and occasional overheating of the air pump, were noted but were outside the primary scope of this study. Importantly, these factors did not compromise the overall operation of the OSRA, and the control system remained effective in achieving the intended actions. Possible improvements and directions for future work were also discussed based on these observations.

One notable challenge was the observable output delay in MATLAB after processing the point cloud data, even after downsampling, due to the large number of calculations involved. To address the response speed issue, it may be beneficial to train a machine learning model to enhance the system's ability to recognize patterns, rather than relying solely on mathematical operations. For instance, using marker recognition could allow the system to determine the real-time movement of the origami actuator with greater efficiency.

Chapter 6

Conclusion

This thesis proposed the design and implementation of an origami-inspired soft robotic arm (OSRA) and its vision-based control system. The system enables users to monitor the spatial position and operational status of the robotic arm through a dashboard while controlling its movements via pneumatic actuators. This project demonstrated that a relatively simple and efficient design, combining stereo vision and pneumatic control, can effectively manage the operation of the OSRA.

Experimentally, a single origami cylinder (without sealing or connection pads) had a natural length of 18.0 cm, compressible to 2.29 cm and extendable to 36.0 cm. A single actuator achieved 180° bending, and the assembled three-actuator arm reached 105°. The pneumatic operating range was 56.97–103.74 kPa. In actuation dynamics, a single actuator completed a full extension-to-compression transition in 4 seconds, whereas the assembled OSRA required 8 seconds along the vertical axis. Additionally, the origami-inspired actuator structure was fabricated using materials such as 120gsm paper, EcoFlex, and acrylic glass, which were tested and optimised for this project.

The system's control mechanism successfully prevents structural damage to the arm by continuously monitoring its position and air pressure. This ensures that the arm does not exceed its operational limits and maintains operational safety. In addition, the vision subsystem was calibrated with a stereo baseline of 107.43 mm and achieved an overall RMS reprojection error of 0.168 px (per-image 0.193 ± 0.102 px), confirming sub-pixel accuracy sufficient for reliable 3D reconstruction.

However, a key limitation identified during the experiments was the computational load of real-time recognition using stereo vision, which introduced delays in system response. On average, the processing time per frame was 0.141 seconds, indicating the need for further optimisation of the vision subsystem to improve processing speed and responsiveness.

Despite these challenges, the system was able to successfully execute the intended tasks of controlling the soft robotic arm's movement, and real-time feedback mechanisms helped prevent any potential damage due to over-extension or compression. In the future, additional improvements could focus on reducing delays in real-time point cloud processing, exploring alternative recognition techniques, and further enhancing the mechanisms for the OSRA.

Bibliography

[1] H. Jin, E. Dong, S. Mao, M. Xu, and J. Yang, "Locomotion modeling of an actinomorphic soft robot actuated by sma springs," in *2014 IEEE International Conference on Robotics and Biomimetics (ROBIO 2014)*, 2014, pp. 21–26.

[2] D. Rus and M. T. Tolley, "Design, fabrication and control of soft robots," *Nature*, vol. 521, no. 7553, pp. 467–475, 2015. [Online]. Available: https://doi.org/10.1038/nature14543

[3] S. Kim, C. Laschi, and B. Trimmer, "Soft robotics: a bioinspired evolution in robotics," *Trends in Biotechnology*, vol. 31, no. 5, pp. 287–294, 2013. [Online]. Available: https://www.sciencedirect.com/science/article/pii/S0167779913000632

[4] K. B. Justus, T. Hellebrekers, D. D. Lewis, A. Wood, C. Ingham, C. Majidi, P. R. LeDuc, and C. Tan, "A biosensing soft robot: Autonomous parsing of chemical signals through integrated organic and inorganic interfaces," *Science Robotics*, vol. 4, no. 31, p. eaax0765, 2019. [Online]. Available: https://www.science.org/doi/abs/10.1126/scirobotics.aax0765

[5] F. Xu and H. Wang, "Soft robotics: Morphology and morphology-inspired motion strategy," *IEEE/CAA Journal of Automatica Sinica*, vol. 8, no. 9, pp. 1500–1522, 2021.

[6] Y. Sun, D. Li, M. Wu, Y. Yang, J. Su, T. Wong, K. Xu, Y. Li, L. Li, X. Yu, and J. Yu, "Origami-inspired folding assembly of dielectric elastomers for programmable soft robots," *Microsystems Nanoengineering*, vol. 8, no. 1, p. 37, 2022. [Online]. Available: https://doi.org/10.1038/s41378-022-00363-5

[7] E. Almanzor, F. Ye, J. Shi, T. G. Thuruthel, H. A. Wurdemann, and F. Iida, "Static shape control of soft continuum robots using deep visual inverse kinematic models," *IEEE Transactions on Robotics*, vol. 39, no. 4, pp. 2973–2988, 2023. [Online]. Available: https://dx.doi.org/10.1109/TRO.2023.3275375

[8] C. Sorensen, P. Hyatt, M. Ricks, S. Nielsen, and M. D. Killpack, "Soft robot configuration estimation and control using simultaneous localization and mapping." IEEE, Conference Proceedings. [Online]. Available: https://dx.doi.org/10.1109/IROS51168.2021.9635896

[9] R. Ohnishi and Y. Hoshino, "Position estimation using stereo camera images and physics engine simulation for robot control." IEEE, Conference Proceedings. [Online]. Available: https://dx.doi.org/10.1109/SCIS-ISIS.2018.00125

[10] B. Trimmer, "A journal of soft robotics: Why now?" *Soft Robotics*, vol. 1, no. 1, pp. 1–4, 2014. [Online]. Available: https://dx.doi.org/10.1089/soro.2013.0003

[11] S. Kim, C. Laschi, and B. Trimmer, "Soft robotics: a bioinspired evolution in robotics," *Trends in Biotechnology*, vol. 31, no. 5, pp. 287–294, 2013. [Online]. Available: https://dx.doi.org/10.1016/j.tibtech.2013.03.002

[12] S. Jadhav, M. R. A. Majit, B. Shih, J. P. Schulze, and M. T. Tolley, "Variable stiffness devices using fiber jamming for application in soft robotics and wearable haptics," *Soft Robot*, vol. 9, no. 1, pp. 173–186, 2022, jadhav, Saurabh Majit, Mohamad Ramzi Abdul Shih, Benjamin Schulze, Jurgen P Tolley, Michael T eng Research Support, Non-U.S. Gov't 2021/02/12 Soft Robot. 2022 Feb;9(1):173-186. doi: 10.1089/soro.2019.0203. Epub 2021 Feb 10. [Online]. Available: https://www.ncbi.nlm.nih.gov/pubmed/33571060

[13] B. C. Mac Murray, C. C. Futran, J. Lee, K. W. O'Brien, A. A. Amiri Moghadam, B. Mosadegh, M. N. Silberstein, J. K. Min, and R. F. Shepherd, "Compliant buckled foam actuators and application in patient-specific direct cardiac compression," *Soft Robotics*, vol. 5, no. 1, pp. 99–108, 2018. [Online]. Available: https://dx.doi.org/10.1089/soro.2017.0018

[14] C. T. O'Neill, C. M. McCann, C. J. Hohimer, K. Bertoldi, and C. J. Walsh, "Unfolding textile-based pneumatic actuators for wearable applications," *Soft Robot*, vol. 9, no. 1, pp. 163–172, 2022, o'Neill, Ciaran T McCann, Connor M Hohimer, Cameron J Bertoldi, Katia Walsh, Conor J eng Research Support, Non-U.S. Gov't 2021/01/23 Soft Robot. 2022 Feb;9(1):163-172. doi: 10.1089/soro.2020.0064. Epub 2021 Jan 21. [Online]. Available: https://www.ncbi.nlm.nih.gov/pubmed/33481682

[15] Q. Guan, J. Sun, Y. Liu, N. M. Wereley, and J. Leng, "Novel bending and helical extensile/contractile pneumatic artificial muscles inspired by elephant trunk," *Soft Robot*, vol. 7, no. 5, pp. 597–614, 2020, guan, Qinghua Sun, Jian Liu, Yanju Wereley, Norman M Leng, Jinsong eng 2020/03/05 Soft Robot. 2020 Oct;7(5):597-614. doi: 10.1089/soro.2019.0079. Epub 2020 Mar 4. [Online]. Available: https://www.ncbi.nlm.nih.gov/pubmed/32130078

[16] C. Ching-Ping and B. Hannaford, "Measurement and modeling of mckibben pneumatic artificial muscles," *IEEE Transactions on Robotics and Automation*, vol. 12, no. 1, pp. 90–102, 1996. [Online]. Available: https://dx.doi.org/10.1109/70.481753

[17] J. King, "Development of soft robotic arm design," School of Engineering, Computer and Mathematical Science, Report, 2020.

[18] M. Wehner, M. T. Tolley, Y. Mengüç, Y.-L. Park, A. Mozeika, Y. Ding, C. Onal, R. F. Shepherd, G. M. Whitesides, and R. J. Wood, "Pneumatic energy sources for autonomous and wearable soft robotics," *Soft Robotics*, vol. 1, no. 4, pp. 263–274, 2014.

[19] J. T. B. O. J. C. W. B. M. K. B. G. M. W. Nicholas W. Bartlett, Michael T. Tolley and R. J. Wood, "A 3d-printed, functionally graded soft robot powered by combustion," *Science*, vol. 349, no. 6244, pp. 161 – 165, 2015.

[20] T. H. Weerakkody, M. Hammond, J. H. Neilan, V. Cichella, and C. Lamuta, "Modeling and control of twisted and coiled artificial muscles for soft robotics," *Meccanica*, vol. 58, no. 4, pp. 643–658, 2023.

[21] J. van der Weijde, H. Vallery, and R. Babuska, "Closed-loop control through self-sensing of a joule-heated twisted and coiled polymer muscle," *Soft Robot*, vol. 6, no. 5, pp. 621–630, 2019, van der Weijde, Joost Vallery, Heike Babuska, Robert eng 2019/05/31 Soft Robot. 2019 Oct;6(5):621-630. doi: 10.1089/soro.2018.0165. Epub 2019 May 30. [Online]. Available: https://www.ncbi.nlm.nih.gov/pubmed/31145024

[22] A. Nespoli, S. Besseghini, S. Pittaccio, E. Villa, and S. Viscuso, "The high potential of shape memory alloys in developing miniature mechanical devices: A review on shape memory alloy mini-actuators," *Sensors and Actuators A: Physical*, vol. 158, no. 1, pp. 149–160, 2010. [Online]. Available: https://www.sciencedirect.com/science/article/pii/S0924424709005469

[23] M. F. R. M. C. C. M. Z. M. T. A. A. D. A. M. P. L. M. Qingkun Liu, Wei Wang and I. Cohen, "Micrometer-sized electrically programmable shape-memory actuators for low-power microrobotics," *Science Robotics*, vol. 6, no. 52, 2021.

[24] M. Behl and A. Lendlein, "Shape-memory polymers," *Materials Today*, vol. 10, no. 4, pp. 20–28, 2007. [Online]. Available: https://www.sciencedirect.com/science/article/pii/S1369702107700470

[25] E. Sachyani Keneth, G. Scalet, M. Layani, G. Tibi, A. Degani, F. Auricchio, and S. Magdassi, "Pre-programmed tri-layer electro-thermal actuators composed of shape memory polymer and carbon nanotubes," *Soft Robot*, vol. 7, no. 2, pp. 123–129, 2020, sachyani Keneth, Ela Scalet, Giulia Layani, Michael Tibi, Gal Degani, Amir Auricchio, Ferdinando Magdassi, Shlomo eng 2019/10/04 Soft Robot. 2020 Apr;7(2):123-129. doi: 10.1089/soro.2018.0159. Epub 2019 Oct 29. [Online]. Available: https://www.ncbi.nlm.nih.gov/pubmed/31580782

[26] B. Q. Y. Chan, Z. W. K. Low, S. J. W. Heng, S. Y. Chan, C. Owh, and X. J. Loh, "Recent advances in shape memory soft materials for biomedical applications," *ACS Applied Materials and Interfaces*, vol. 8, no. 16, p. 10070 – 10087, 2016, cited by: 334. [Online]. Available: https://www.scopus.com/inward/record.uri?eid=2-s2.0-84966429181&doi=10.1021%2facsami.6b01295&partnerID=40&md5=7947930734ad14826eb41415ca2a7bc3

[27] J. M. Korde and B. Kandasubramanian, "Naturally biomimicked smart shape memory hydrogels for biomedical functions," *Chemical Engineering Journal*, vol. 379, p. 122430, 2020. [Online]. Available: https://www.sciencedirect.com/science/article/pii/S1385894719318339

[28] X. Li, X. Cai, Y. Gao, and M. J. Serpe, "Reversible bidirectional bending of hydrogel-based bilayer actuators," *Journal of Materials Chemistry B*, vol. 5, no. 15, pp. 2804–2812, 2017. [Online]. Available: https://dx.doi.org/10.1039/C7TB00426E

[29] Jan 2025. [Online]. Available: https://en.wikipedia.org/wiki/Silicone#cite_note-Ullmann-1

[30] H. Chen, M. A. Ali, Z. Wang, J. Chen, M. N. Ramadan, and M. Alkhedher, "Performance optimizing of pneumatic soft robotic hands using wave-shaped contour actuator," *Results in Engineering*, vol. 25, p. 103456, 2025. [Online]. Available: https://www.sciencedirect.com/science/article/pii/S2590123024017080

[31] M. Manns, J. Morales, and P. Frohn, "Additive manufacturing of silicon based pneunets as soft robotic actuators," *Procedia CIRP*, vol. 72, pp. 328–333, 2018, 51st CIRP Conference on Manufacturing Systems. [Online]. Available: https://www.sciencedirect.com/science/article/pii/S2212827118303457

[32] P. Testa, R. W. Style, J. Cui, C. Donnelly, E. Borisova, P. M. Derlet, E. R. Dufresne, and L. J. Heyderman, "Magnetically addressable shape-memory and stiffening in a composite elastomer," *Advanced Materials*, vol. 31, no. 29, p. 1900561, 2019. [Online]. Available: https://onlinelibrary.wiley.com/doi/abs/10.1002/adma.201900561

[33] X. Li, H. Duan, P. Lv, and X. Yi, "Soft actuators based on liquid–vapor phase change composites," *Soft Robotics*, vol. 8, no. 3, pp. 251–261, 2021, pMID: 32589522. [Online]. Available: https://doi.org/10.1089/soro.2020.0018

[34] R. Chellattoan and G. Lubineau, "A stretchable fiber with tunable stiffness for programmable shape change of soft robots," *Soft Robotics*, vol. 9, no. 6, pp. 1052–1061, 2022, pMID: 35049362. [Online]. Available: https://doi.org/10.1089/soro.2021.0032

[35] J. W. Ambrose, N. Z. R. Chiang, D. S. Y. Cheah, and C.-H. Yeow, "Compact multilayer extension actuators for reconfigurable soft robots," *Soft Robotics*, vol. 10, no. 2, pp. 301–313, 2023, pMID: 36037007. [Online]. Available: https://doi.org/10.1089/soro.2022.0042

[36] B. Oh, Y.-G. Park, H. Jung, S. Ji, W. H. Cheong, J. Cheon, W. Lee, and J.-U. Park, "Untethered soft robotics with fully integrated wireless sensing and actuating systems for somatosensory and respiratory functions," *Soft Robotics*, vol. 7, no. 5, pp. 564–573, 2020, pMID: 31977289. [Online]. Available: https://doi.org/10.1089/soro.2019.0066

[37] N. H. Nguyen and V. A. Ho, "Mechanics and morphological compensation strategy for trimmed soft whisker sensor," *Soft Robotics*, vol. 9, no. 1, pp. 135–153, 2022, pMID: 33464996. [Online]. Available: https://doi.org/10.1089/soro.2020.0056

[38] P. T. Phan, T. T. Hoang, M. T. Thai, H. Low, N. H. Lovell, and T. N. Do, "Twisting and braiding fluid-driven soft artificial muscle fibers for robotic applications," *Soft Robot*, vol. 9, no. 4, pp. 820–836, 2022, phan, Phuoc Thien Hoang, Trung Thien Thai,

Mai Thanh Low, Harrison Lovell, Nigel Hamilton Do, Thanh Nho eng 2021/10/07 Soft Robot. 2022 Aug;9(4):820-836. doi: 10.1089/soro.2021.0040. Epub 2021 Oct 5. [Online]. Available: https://www.ncbi.nlm.nih.gov/pubmed/34613831

[39] H. Lipson, "Challenges and opportunities for design, simulation, and fabrication of soft robots," *Soft Robotics*, vol. 1, no. 1, pp. 21–27, 2014. [Online]. Available: https://doi.org/10.1089/soro.2013.0007

[40] B. S. Limited, "Bs en iso/astm 52900:2021 - tc tracked changes. additive manufacturing. general principles. fundamentals and vocabulary," 2022.

[41] R. Mutlu, G. Alici, M. in het Panhuis, and G. M. Spinks, "3d printed flexure hinges for soft monolithic prosthetic fingers," *Soft Robotics*, vol. 3, no. 3, pp. 120–133, 2016. [Online]. Available: https://doi.org/10.1089/soro.2016.0026

[42] C. Tawk, M. in het Panhuis, G. M. Spinks, and G. Alici, "Bioinspired 3d printable soft vacuum actuators for locomotion robots, grippers and artificial muscles," *Soft Robotics*, vol. 5, no. 6, pp. 685–694, 2018, pMID: 30040042. [Online]. Available: https://doi.org/10.1089/soro.2018.0021

[43] M. Tyagi, G. M. Spinks, and E. W. Jager, "3d printing microactuators for soft microrobots," *Soft Robotics*, vol. 8, no. 1, pp. 19–27, 2021, pMID: 32326869. [Online]. Available: https://doi.org/10.1089/soro.2019.0129

[44] Jan 2025. [Online]. Available: https://en.wikipedia.org/wiki/Stereolithography

[45] E. B. Joyee and Y. Pan, "A fully three-dimensional printed inchworm-inspired soft robot with magnetic actuation," *Soft Robotics*, vol. 6, no. 3, pp. 333–345, 2019, pMID: 30720388. [Online]. Available: https://doi.org/10.1089/soro.2018.0082

[46] E. B. Joyee, A. Szmelter, D. Eddington, and Y. Pan, "3d printed biomimetic soft robot with multimodal locomotion and multifunctionality," *Soft Robotics*, vol. 9, no. 1, pp. 1–13, 2022, pMID: 33275498. [Online]. Available: https://doi.org/10.1089/soro.2020.0004

[47] F. Ahmadi, J. Song, and R. Zoughi, "Electromagnetic scattering properties of metal powder cloud for laser powder bed fusion (lpbf) additive manufacturing (am)," *IEEE Open Journal of Antennas and Propagation*, vol. 5, no. 6, pp. 1639–1648, 2024. [Online]. Available: https://dx.doi.org/10.1109/OJAP.2024.3431536

[48] Dec 2024. [Online]. Available: https://en.wikipedia.org/wiki/Photolithography#:~:text=Photolithography%20is%20the%20most%20common,of%20the%20objects%20it%20creates.

[49] W. Wu, R. M. Guijt, Y. E. Silina, M. Koch, and A. Manz, "Plant leaves as templates for soft lithography," *RSC Advances*, vol. 6, no. 27, pp. 22 469–22 475, 2016. [Online]. Available: https://dx.doi.org/10.1039/C5RA25890A

[50] A. A. Amiri Moghadam, S. Alaie, S. Deb Nath, M. Aghasizade Shaarbaf, J. K. Min, S. Dunham, and B. Mosadegh, "Laser cutting as a rapid method for fabricating thin

soft pneumatic actuators and robots," *Soft Robotics*, vol. 5, no. 4, pp. 443–451, 2018, pMID: 29924697. [Online]. Available: https://doi.org/10.1089/soro.2017.0069

[51] Y. Han, A. Varadarajan, T. Kim, G. Zheng, K. Kitani, A. Kelliher, T. Rikakis, and Y.-L. Park, "Smart skin: Vision-based soft pressure sensing system for in-home hand rehabilitation," *Soft Robotics*, vol. 9, no. 3, pp. 473–485, 2022, pMID: 34415805. [Online]. Available: https://doi.org/10.1089/soro.2020.0083

[52] M. Zhu, Y. Mori, T. Wakayama, A. Wada, and S. Kawamura, "A fully multi-material three-dimensional printed soft gripper with variable stiffness for robust grasping," *Soft Robotics*, vol. 6, no. 4, pp. 507–519, 2019, pMID: 30973316. [Online]. Available: https://doi.org/10.1089/soro.2018.0112

[53] Z. Xie, A. G. Domel, N. An, C. Green, Z. Gong, T. Wang, E. M. Knubben, J. C. Weaver, K. Bertoldi, and L. Wen, "Octopus arm-inspired tapered soft actuators with suckers for improved grasping," *Soft Robotics*, vol. 7, no. 5, pp. 639–648, 2020, pMID: 32096693. [Online]. Available: https://doi.org/10.1089/soro.2019.0082

[54] R. Hashem, S. Kazemi, M. Stommel, L. K. Cheng, and W. Xu, "A biologically inspired ring-shaped soft pneumatic actuator for large deformations," *Soft Robotics*, vol. 9, no. 4, pp. 807–819, 2022, pMID: 34704835. [Online]. Available: https://doi.org/10.1089/soro.2021.0013

[55] L. Wang, J. Lam, X. Chen, J. Li, R. Zhang, Y. Su, and Z. Wang, "Soft robot proprioception using unified soft body encoding and recurrent neural network," *Soft Robotics*, vol. 10, no. 4, pp. 825–837, 2023, pMID: 37001175. [Online]. Available: https://doi.org/10.1089/soro.2021.0056

[56] Z. Chen, S. Siu, S. Tin, Y. Liu, H. Cao, Y. Gao, J. Zhou, and Y. Liu, "A dexterous origami-inspired soft (dois) robot for objects reorientation and overturn," in *2021 IEEE International Conference on Real-time Computing and Robotics (RCAR)*, 2021, pp. 1379–1384.

[57] E. Zhang and E. Zhang, "Spiro: An ai based origami inspired soft robot with multidimensional locomotion and multimodal data analysis for infrastructure assessments." IEEE, Conference Proceedings. [Online]. Available: https://dx.doi.org/10.1109/CCDC62350.2024.10587655

[58] Y. Ge, R. Zong, X. Chen, and T. Nanayakkara, "An origami-inspired endoscopic capsule with tactile perception for early tissue anomaly detection," *IEEE Robotics and Automation Letters*, vol. 9, no. 11, pp. 10 018–10 025, 2024. [Online]. Available: https://dx.doi.org/10.1109/LRA.2024.3469821

[59] M. Gardiner, "Kresling." [Online]. Available: https://orilab.art/natural/kresling

[60] W. contributors, "Miura fold," accessed: 2025-02-13. [Online]. Available: https://en.wikipedia.org/wiki/Miura_fold

[61] C. G. Foster, "Some observations on the yoshimura buckle pattern for thin-walled cylinders," 1979.

[62] Y. Chen, H. Feng, J. Ma, R. Peng, and Z. You, "Symmetric waterbomb origami," *Proc Math Phys Eng Sci*, vol. 472, no. 2190, p. 20150846, 2016, chen, Yan Feng, Huijuan Ma, Jiayao Peng, Rui You, Zhong eng England 2016/07/21 Proc Math Phys Eng Sci. 2016 Jun;472(2190):20150846. doi: 10.1098/rspa.2015.0846. [Online]. Available: https://www.ncbi.nlm.nih.gov/pubmed/27436963

[63] ivan g, "Origami twisted tower," 2018 2018. [Online]. Available: https://steemit.com/origami/@ivan-g/origami-twisted-tower

[64] Y. Yu, X. Duan, X. Xu, S. Tian, W. Zhao, and Y. Luo, "Programmable instability of miura tube–based spatial structures," *Journal of Engineering Mechanics*, vol. 149, no. 9, p. 04023065, 2023. [Online]. Available: https://ascelibrary.org/doi/abs/10.1061/JENMDT.EMENG-6548

[65] G. Giménez-Ribes, A. Ghorbani, S. Y. Teng, E. Van Der Linden, and M. Habibi, "Shear and shear-induced normal responses of origami cylinders relate to their structural asymmetries," *Materials amp; Design*, vol. 240, p. 112874, 2024. [Online]. Available: https://dx.doi.org/10.1016/j.matdes.2024.112874

[66] M. Kshirsagar, S. D. Ambike, N. Jaya Prakash, B. Kandasubramanian, and P. Deshpande, "Origami engineering: Creating dynamic functional materials through folded structures," *Hybrid Advances*, vol. 4, p. 100092, 2023. [Online]. Available: https://www.sciencedirect.com/science/article/pii/S2773207X23000751

[67] B. Kresling, *Biruta Kresling (2008) "Natural twist buckling in shells: From the hawkmoth's bellows to the deployable Kresling-pattern and cylindrical Miura-ori" IASS-IACM 2008, pp. 18-21*, 2008.

[68] X. Wang, H. Qu, K. Zhao, X. Yang, and S. Guo, "Kresling origami derived structures and inspired mechanical metamaterial," *Smart Materials and Structures*, vol. 33, no. 7, p. 075030, 2024. [Online]. Available: https://dx.doi.org/10.1088/1361-665X/ad5a5a

[69] H. Feng, J. Ma, Y. Chen, and Z. You, "Twist of tubular mechanical metamaterials based on waterbomb origami," *Scientific Reports*, vol. 8, no. 1, p. 9522, 2018. [Online]. Available: https://doi.org/10.1038/s41598-018-27877-1

[70] Y. Wang and K. Lee, "3d-printed semi-soft mechanisms inspired by origami twisted tower," in *2017 NASA/ESA Conference on Adaptive Hardware and Systems (AHS)*, 2017, pp. 161–166.

[71] H.-Q. Nguyen, "Closed-loop control of a soft robotic xy-table to manipulate delicate objects," Thesis, 2019.

[72] T. V. Minh, T. Tjahjowidodo, H. Ramon, and H. Van Brussel, "Cascade position control of a single pneumatic artificial muscle–mass system with hysteresis compensation," *Mechatronics*, vol. 20, no. 3, pp. 402–414, 2010.

[73] M. Russo, S. M. H. Sadati, X. Dong, A. Mohammad, I. D. Walker, C. Bergeles, K. Xu, and D. A. Axinte, "Continuum robots: An overview," *Advanced Intelligent Systems*, vol. 5, no. 5, p. 2200367, 2023. [Online]. Available: https://dx.doi.org/10.1002/aisy.202200367

[74] R. J. Webster and B. A. Jones, "Design and kinematic modeling of constant curvature continuum robots: A review," *The International Journal of Robotics Research*, vol. 29, no. 13, pp. 1661–1683, 2010.

[75] Z. Yi, K. Ma, Y. Sen, and F. Xu, *Hysteresis Modeling and Compensation Control of Soft Gripper*. Springer International Publishing, 2021, pp. 241–252. [Online]. Available: https://dx.doi.org/10.1007/978-3-030-89095-7_24

[76] T. George Thuruthel, Y. Ansari, E. Falotico, and C. Laschi, "Control strategies for soft robotic manipulators: A survey," *Soft Robot*, vol. 5, no. 2, pp. 149–163, 2018, george Thuruthel, Thomas Ansari, Yasmin Falotico, Egidio Laschi, Cecilia eng Research Support, Non-U.S. Gov't 2018/01/04 Soft Robot. 2018 Apr;5(2):149-163. doi: 10.1089/soro.2017.0007. Epub 2018 Jan 3. [Online]. Available: https://www.ncbi.nlm.nih.gov/pubmed/29297756

[77] T. Behr, T. P. Pusch, M. Siegfarth, D. Hüsener, T. Mörschel, and L. Karstensen, "Deep reinforcement learning for the navigation of neurovascular catheters," *Current Directions in Biomedical Engineering*, vol. 5, no. 1, pp. 5–8, 2019. [Online]. Available: https://dx.doi.org/10.1515/cdbme-2019-0002

[78] F. Largilliere, E. Coevoet, M. Sanz-Lopez, L. Grisoni, and C. Duriez, "Stiffness rendering on soft tangible devices controlled through inverse fem simulation." IEEE, Conference Proceedings. [Online]. Available: https://dx.doi.org/10.1109/IROS.2016.7759768

[79] H. Thien, M. Stommel, F. Le Daheron, A. Le Page, Z. Deng, and W. L. Xu, "Embedded infrared imaging to measure the deformation of a soft robotic actuator," in *2016 International Conference on Image and Vision Computing New Zealand (IVCNZ)*, 2016, pp. 1–6.

[80] J. Tapia, E. Knoop, M. Mutny, M. A. Otaduy, and M. Bacher, "Makesense: Automated sensor design for proprioceptive soft robots," *Soft Robot*, vol. 7, no. 3, pp. 332–345, 2020, tapia, Javier Knoop, Espen Mutny, Mojmir Otaduy, Miguel A Bacher, Moritz eng 2020/01/01 Soft Robot. 2020 Jun;7(3):332-345. doi: 10.1089/soro.2018.0162. Epub 2019 Dec 9. [Online]. Available: https://www.ncbi.nlm.nih.gov/pubmed/31891526

[81] L. O. Tiziani and F. L. Hammond, "Optical sensor-embedded pneumatic artificial muscle for position and force estimation," *Soft Robot*, vol. 7, no. 4, pp. 462–477, 2020, tiziani, Lucas O Hammond, Frank L eng Research Support, Non-U.S. Gov't 2020/02/08 Soft Robot. 2020 Aug;7(4):462-477. doi: 10.1089/soro.2019.0019. Epub 2020 Feb 7. [Online]. Available: https://www.ncbi.nlm.nih.gov/pubmed/32031920

[82] S. Sankar, D. Balamurugan, A. Brown, K. Ding, X. Xu, J. H. Low, C. H. Yeow, and N. Thakor, "Texture discrimination with a soft biomimetic finger using a flexible neuromorphic tactile sensor array that provides sensory feedback," *Soft Robot*, vol. 8, no. 5, pp. 577–587, 2021, sankar, Sriramana Balamurugan, Darshini Brown, Alisa Ding, Keqin Xu, Xingyuan Low, Jin Huat Yeow, Chen Hua Thakor, Nitish eng Research Support, Non-U.S. Gov't 2020/09/26 Soft Robot. 2021 Oct;8(5):577-587. doi: 10.1089/soro.2020.0016. Epub 2020 Sep 23. [Online]. Available: https://www.ncbi.nlm.nih.gov/pubmed/32976080

[83] Z. Zhang, T. Yang, T. Zhang, F. Zhou, N. Cen, T. Li, and G. Xie, "Global vision-based formation control of soft robotic fish swarm," *Soft Robot*, vol. 8, no. 3, pp. 310–318, 2021, zhang, Zhen Yang, Tao Zhang, Tianhao Zhou, Fanghao Cen, Nuo Li, Tiefeng Xie, Guangming eng 2020/07/14 Soft Robot. 2021 Jun;8(3):310-318. doi: 10.1089/soro.2019.0174. Epub 2020 Jul 10. [Online]. Available: https://www.ncbi.nlm.nih.gov/pubmed/32654595

[84] "What are the main steps in a typical computer vision pipeline?" 2024 2024. [Online]. Available: https://www.geeksforgeeks.org/what-are-the-main-steps-in-a-typical-computer-vision-pipeline/

[85] N. INSTRUMENTS, "A practical guide to machine vision lighting." [Online]. Available: https://www.ni.com/en/shop/choosing-the-right-hardware-for-your-vision-applications/a-practical-guide-to-machine-vision-lighting.html

[86] R. Garg, S. Indu, and S. Chaudhury, "Camera and light source placement: A multi-objective approach," pp. 187–191, 2011.

[87] M. Elgendy, "The computer vision pipeline, part 3: image preprocessing." [Online]. Available: https://freecontent.manning.com/the-computer-vision-pipeline-part-3-image-preprocessing/

[88] T. M. Inc., "imsubtract," 2024. [Online]. Available: https://www.mathworks.com/help/images/ref/imsubtract.html

[89] ——, "vision.foregrounddetector," 2024. [Online]. Available: https://www.mathworks.com/help/vision/ref/vision.foregrounddetector-system-object.html

[90] A. W. R. Fisher, S. Perkins and E. Wolfart., "Skeletonization/medial axis transform," 2003. [Online]. Available: https://homepages.inf.ed.ac.uk/rbf/HIPR2/skeleton.htm

[91] P.-T. B. A. M. Valerio Pascucci, Giorgio Scorzelli, "Robust on-line computation of reeb graphs: simplicity and speed," *ACM Transactions on Graphics*, vol. 26, no. 3, 2007.

[92] T. R. Institute, "Seeing clearly: Advancing robotic stereo vision," 2021. [Online]. Available: https://medium.com/toyotaresearch/seeing-clearly-advances-in-robotic-vision-through-learning-stereo-depth-52e3c9440646

[93] M. Jolaei, A. Hooshiar, J. Dargahi, and M. Packirisamy, "Toward task autonomy in robotic cardiac ablation: Learning-based kinematic control of soft tendon-driven catheters," *Soft Robotics*, vol. 8, no. 3, pp. 340–351, 2021. [Online]. Available: https://dx.doi.org/10.1089/soro.2020.0006

[94] M. S. Sofla, S. Vayakkattil, and M. Calisti, "Haptic localization with a soft whisker from moment readings at the base," *Soft Robotics*, vol. 11, no. 4, pp. 539–549, 2024. [Online]. Available: https://dx.doi.org/10.1089/soro.2023.0098

[95] S. Li, L. Ye, H. Yu, X. Yin, C. Xia, W. Ding, X. Wang, and B. Liang, "Jamtac: A tactile jamming gripper for searching and grasping in low-visibility environments," *Soft Robotics*, vol. 10, no. 5, pp. 988–1000, 2023. [Online]. Available: https://dx.doi.org/10.1089/soro.2022.0134

[96] B. Ward-Cherrier, N. Pestell, L. Cramphorn, B. Winstone, M. E. Giannaccini, J. Rossiter, and N. F. Lepora, "The tactip family: Soft optical tactile sensors with 3d-printed biomimetic morphologies," *Soft Robotics*, vol. 5, no. 2, pp. 216–227, 2018. [Online]. Available: https://dx.doi.org/10.1089/soro.2017.0052

[97] OpenCV, "Depth map from stereo images," 2024. [Online]. Available: https://docs.opencv.org/4.x/dd/d53/tutorial_py_depthmap.html

[98] T. M. Inc., "Using the stereo camera calibrator app," 2024. [Online]. Available: https://www.mathworks.com/help/vision/ug/using-the-stereo-camera-calibrator-app.html

[99] S. Mittal, "A survey on optimized implementation of deep learning models on the nvidia jetson platform," *Journal of Systems Architecture*, vol. 97, pp. 428–442, 2019. [Online]. Available: https://dx.doi.org/10.1016/j.sysarc.2019.01.011

[100] T. Moons, "3d reconstruction from multiple images part 1: Principles," *Foundations and Trends® in Computer Graphics and Vision*, vol. 4, no. 4, pp. 287–404, 2008. [Online]. Available: https://dx.doi.org/10.1561/0600000007

[101] T. M. Inc., "Point cloud processing," 2024. [Online]. Available: https://www.mathworks.com/help/vision/point-cloud-processing.html

[102] J. Zhao, T. Yu, Y. Zhang, H. Sun, and M. Xu, "Electrostatically driven kresling origami soft pump," *IEEE Robotics and Automation Letters*, vol. 9, no. 8, pp. 7166–7173, 2024. [Online]. Available: https://dx.doi.org/10.1109/LRA.2024.3419640

[103] M. Moshtaghzadeh and P. Mardanpour, "Design, mechanical characteristics evaluation, and energy absorption of multi-story kresling origami-inspired structures," *Mechanics Research Communications*, vol. 130, p. 104125, 2023. [Online]. Available: https://dx.doi.org/10.1016/j.mechrescom.2023.104125

[104] D. Li, D. Fan, R. Zhu, Q. Lei, Y. Liao, X. Yang, Y. Pan, Z. Wang, Y. Wu, S. Liu, and H. Wang, "Origami-inspired soft twisting actuator," *Soft Robotics*, vol. 10, no. 2, pp. 395–409, 2023. [Online]. Available: https://dx.doi.org/10.1089/soro.2021.0185

[105] JB86, "Mold for soft actuator/gripper - parametric - openscad," 2020. [Online]. Available: https://www.thingiverse.com/thing:4396187

[106] S. Electronics, "Sparkfun qwiic micropressure sensor," 2019, accessed: 2025-02-13. [Online]. Available: https://www.sparkfun.com/products/16476